Lithium- and oxygen-driven structural evolution in Co-free Li-Mn-rich oxides as cathodes for lithium ion batteries

Zur Erlangung des akademischen Grades eines

DOKTORS DER NATURWISSENSCHAFTEN

(Dr. rer. nat.)

der KIT-Fakultät für Chemie und Biowissenschaften

des Karlsruher Instituts für Technologie (KIT)

genehmigte

DISSERTATION

von

Master – Chemical technique

Weibo Hua

aus Xinxiang, China

KIT-Dekan: Prof. Dr. Reinhard Fischer

Referent: Prof. Dr. Helmut Ehrenberg

Korreferent: Prof. Dr. Stefano Passerini

Tag der mündlichen Prüfung: 04.02.2019

Contents

Abbreviations, Constants, Symbols

ΔG	Non-standard Gibbs free energy
ΔG^0	Standard Gibbs free energy
n	Number of electrons transferred in a electrode reaction
F	Faraday constant (96485.3 C/mol or 26.801 Ah/mol)
E	Cell voltage under non-standard conditions
E^0	Standard battery potential (at 25 ^{o}C temperature and 1 bar pressure)
R	Universal gas constant (8.314 J mol^{-1} K^{-1})
T	Absolute temperature
a	Ratio of chemical activities of products and reactants
E_{eq}	Equilibrium potential of the electrode
$\{A\}$	Chemical activities of relevant species in a reaction
j	Electrode current density
i	Current
A	Surface area of the electrode
j_0	Exchange current density
α_a	Cathodic charge transfer coefficient
α_c	Anodic charge transfer coefficient
E_{S}	Specific energy density
t	Time
$v(t)$	Voltage as a function of time
$i(t)$	Current as a function of time
τ	Total time
m	Device mass
C_T	Theoretical specific capacity
Q	Charge amount
C_T	Theoretical specific capacity
Δx	Number of moles of lithium ions participated in a reaction

M_w	Molar mass of the electrode material
C_P	Practical specific capacity
P_S	Specific power density
D_{Li}	Lithium ion diffusivity
ΔG_d	Activation energy for the movement of lithium ions
k_B	Boltzmann's constant
D_0	Kinetic prefactor
L	Ionic diffusion length
C-rate	Current density
γ	Grain boundary surface tension
V	Molar volume
r	Radius of particles
x	Diffusion distance
D^*	Self-diffusion coefficient
$\frac{\Delta V}{V_0}$	Volume change
$\frac{\Delta L}{L_0}$	Length variation
P_a	Absorbed power
σ	Conductivity
E_e	Electric field strength
f	Frequency of microwave radiation
ε_0	Permittivity of free space
ε''	Relative dielectric loss factor of the sample
d	Penetration depth
λ	Wavelength
$\tan\delta$	Energy loss tangent
BET	Brunauer, Emmett and Teller
TG	Thermogravimetric
DSC	Differential scanning calorimetric
XRD	X-ray diffraction

SRD	Synchrotron radiation diffraction
NPD	Neutron powder diffraction
BVS	Bond valence sum
SEM	Scanning electron microscopy
TEM	Transmission electron microscopy
SAED	Selected area electron diffraction
STEM	Scanning transmission electron microscopy
ABF	Annular bright-field
HAADF	High angle annular dark-field
ED	Electron diffraction
DFT	Density functional theory
ICP-OES	Inductively coupled plasma optical emission spectroscopy
XPS	X-ray photoelectron spectroscopy
XAS	X-ray absorption spectroscopy
XANES	X-ray absorption near edge structure
EXAFS	Extended X-Ray absorption fine structure
MAS NMR	Magic-angle spinning nuclear magnetic resonance
PVdF	Polyvinylidene fluoride
EC	Ethylene carbonate
DMC	Dimethyl carbonate

List of Figures

List of Tables

Zusammenfassung

Die lithiumreichen 3*d*-Übergangsmetalloxide (LLOs) (TM = Übergangsmetall) sind aktuell aussichtreiche Kandidaten als Kathodenmaterialien für Lithium-Ionen-Batterien der nächsten Generation (LIBs), da sie eine viel höhere Entladekapazität, nämlich fast 300 mAh g^{-1} bei 0,1 C, als die derzeit üblicherweise verwendeten Materialien, nämlich bis 180 mAh g^{-1} bei 0,1 C, besitzen. Der Syntheseprozess von LLOs ist noch nicht vollständig verstanden. Eine der interessantesten und immer noch offenen Fragen ist, wie Lithium- und Sauerstoffatome während der Synthese der LLO-Endprodukte in die Kristallstruktur der Vorstufe eingebaut werden. In dieser Doktorarbeit wurde eine systematische Untersuchung zur Beantwortung dieser Frage durchgeführt.

Um die gewünschten LLOs mit guten Eigenschaften zu erhalten, ist es erforderlich, eine geeignete Morphologie für den Präkursor zu entwerfen, da diese eine sehr wichtige Rolle in der Hochtemperaturreaktion der Lithiierung spielt. Zur Synthese des dreidimensionalen (3D) ‚nano flower'-strukturierten Präkursor für LLOs wurde ein leistungsfähiges Hydroxid-Kopräzipations-Verfahren eingesetzt.

Zur Untersuchung der thermisch induzierten strukturellen Entwicklung wurde eine Kombination von Methoden wie Thermogravimetrie (TG), dynamische Differenz-Kalorimetrie (DSC) und *in situ* Hochtemperatur Synchrotronstrahlung Diffraktion (SRD) eingesetzt. Die Ergebnisse lassen sich kurz zusammengefasst so beschreiben: während der thermischen Behandlung der Präkursoren allein, bestehend aus geschichtetem TMOOH (Raumgruppensymmetrie *C*2/*m*) und tetragonalem TM_3O_4 ($I4_1/amd$), kommt es zu einer Umwandlung in eine einzige kubische TM_3O_4-Spinellphase ($Fd\,\bar{3}\,m$) einhergehend mit Sauerstoffabgabe. Wird stattdessen während der Synthese dem Präkursor eine Lithiumquelle angeboten, kommt es während der Synthese der LLOs zur Aufnahme von Sauerstoff und dessen Einbau in das kristalline Sauerstoffgitter.

Eine vielversprechende und praktische Methode ist eine Kopräzipationsmethode gefolgt von einer thermischen Behandlung mittels Mikrowellen. Damit lässt sich die Synthese der geschichteten monoklinen $Li[Li_{0.2}Ni_{0.2}Mn_{0.6}]O_2$-Kathodenmaterialien mit einer hohen Ratenfähigkeit kontrollieren: es können spezifische Entladekapazitäten von bis 171 mAh g^{-1} bei 10 C erzielt werden. Während des Lithium-Insertionsprozesses bei hoher Temperatur zeigt die

höhere Oxidationsstufe der Übergangsmetallkationen an, dass Sauerstoffionen kontinuierlich in die Wirtsstruktur eingefügt werden. Dadurch bleibt die Ladungsneutralität erhalten und es werden offene Koordinationsstellen für eingebaute Lithiumionen und bewegte TM-Ionen während der Herstellung von LLOs bereitgestellt. Während der Lithiierung-Reaktionen bei hohen Temperaturen können Phasenübergange, Atomumlagerungen und Oberflächenrekonstruktionen beobachtet werden.

Trotz der Tatsache, dass das synthetisierte monokline $Li[Li_{0.2}Ni_{0.2}Mn_{0.6}]O_2$-Kathodenmaterial eine gute Ratenfähigkeit liefert, leidet sie aber unter einem starken Spannungsabfall während des elektrochemischen Zyklierens. Um den zugrundeliegenden Degradationsmechanismus aufzuklären, muss man mittels hochaufgelöster *in situ* SRD die strukturellen Entwicklungen der Li-Überschussschichtelektrode während des elektrochemischen Zyklierens untersuchen und bestimmen, welche strukturellen Faktoren für die Degradation der LLOs verantwortlich sind. Die *in situ* SRD-Ergebnisse legen nahe, dass die Bildung einer Nanodomänestruktur bestehend aus einer Schichtstruktur-Phase und einer spinellartigen Phase nach dem Laden auf hohe Spannungen (über 4,5 V) der Hauptfaktor für die strukturelle Instabilität ist. Die Degradationssrisse im Elektrodenmaterial können nach längerer Zyklierzeit direkt durch hochauflösende Transmissionselektronenmikroskopie (HRTEM) beobachtet werden. Sie werden durch die während des Delithiierungs- / Lithiierungsprozesses auftretenden anisotropen Gitterdehnungen und Volumenänderungen induziert.

Um die Beziehung zwischen Syntheseprozess und Degradation von LLOs besser zu verstehen, wurde eine Reihe von $Li_xNi_{0.2}Mn_{0.6}O_y$-Oxiden mit einer großen Vielfalt von Lithiumgehalten ($0{,}00 \leq x \leq 1{,}52$) durch einen Hochtemperatur-Syntheseprozess hergestellt. Die konsistenten Ergebnisse zeigen, dass die strukturellen Eigenschaften von $Li_xNi_{0.2}Mn_{0.6}O_y$ -Oxiden stark von der chemischen Zusammensetzung bezüglich Lithium und Sauerstoff abhängen. Das Li-überschüssige schichtartige $Li[Li_{0.2}Ni_{0.2}Mn_{0.6}]O_2$-Oxid ist nur stabil, wenn während der Synthese eine beträchtliche Menge an Lithium und Sauerstoff verfügbar ist. Im Vergleich dazu ist die Spinell-/Steinsalz-Struktur-Phase bei einer niedrigeren Konzentration von verfügbarem Lithium thermisch stabil. Diese Ergebnisse bieten auch neue Einblicke in die Art der Ermüdungsprozesse in LLOs.

Die Tatsache, dass eine Konkurrenz besteht zwischen thermisch induziertem Sauerstoffverlust und Lithium-Insertion induzierter Sauerstoffaufnahme, gestaltet die Hochtemperaturreaktion des Präkursors mit der Lithiumquelle sehr kompliziert. Schließlich wurde eine *in situ* Hochtemperatur-

SRD-Technik verwendet, um die chemisch (d.h. Li & O) induzierte strukturelle Entwicklung für das reine Spinelloxid ($Fd\ \bar{3}\ m$) zu erforschen, um so einen zuverlässigen Lithiierungsreaktionsmechanismus mit Sauerstoffaufnahme zu untersuchen. Der Mechanismus zur Bildung von Li-haltigen Oxiden deutet darauf hin, dass die Li-Überschuss-Schichtoxide als Ergebnis der Lithium- und Sauerstoffinsertion während der Synthese in Luftatmosphärein einen Spinell ($Fd\bar{3}m$) und/oder in eine Li-haltige Steinsalzphase ($Fm\bar{3}m$) gebildet werden können. Wenn eine kleine Menge Lithium bereitgestellt wird, neigen die Lithiumionen dazu, sich in den Zwischenräumen von Sauerstofftetraedern zu lokalisieren und bilden die Li enthaltenden Spinelloxide. Da nach und nach mehr Lithiumionen in die Spinellmatrix eingebaut werden, neigen die Lithiumionen dazu, bevorzugt die oktaedrischen Stellen zu besetzen, die eine Li-enthaltende Steinsalz-Struktur-Phase und / oder eine Li-reiche Schichtphase bilden. Da die kubisch dicht gepackten Sauerstoffanionen an der Phasenumwandlung beteiligt sind, werden Sauerstoffatome nur in das Sauerstoffoberflächengitter eingefügt, was mit Kristallwachstum und / oder Rekristallisation begleitet ist.

Diese Erkenntnisse tragen nicht nur zu einem umfassenden Verständnis der Zusammenhänge zwischen Präparation, Struktur und Leistung von LIBs der nächsten Generation bei, sondern bieten auch neue Einblicke in die Wechselwirkung von Sauerstoff mit Lithium in Li-haltigen Oxiden während der Synthese und des elektrochemischen Zyklierens.

Abstract

Nowadays, the lithium-rich layered 3*d*-transition-metal (TM) oxides (LLOs) are regarded as one of the most attractive cathode materials for next-generation lithium-ion batteries (LIBs), because they can exhibit a discharge capacity (approaching 300 mAh g^{-1} at 0.1 C) much higher than that of the currently used materials (~ 180 mAh g^{-1} at 0.1 C). However, the formation mechanism of LLOs has not been fully understood on a fundamental level yet. One of the most interesting and still open questions is about lithium and oxygen atoms are incorporated into the precursor's crystal structure during the synthesis of final LLO products. A systematic exploration of this subject was conducted in this PhD work.

In order to obtain the desired LLOs with high performance, it is necessary to design a proper morphology for the precursor which acts as an important source for the high-temperature lithiation reaction. A powerful hydroxide coprecipitation process was employed to synthesize the three dimensional (3D) nanoflower-structured precursor for LLOs.

A combination of thermogravimetric (TG), differential scanning calorimetric (DSC) and *in situ* high-temperature synchrotron radiation diffraction (SRD) experiments was utilized to investigate the thermally induced structural evolution. The results show that the precursor composed of layered TMOOH (*C*2/*m*) and tetragonal TM_3O_4 ($I4_1/amd$) transforms into a single cubic spinel TM_3O_4 phase ($Fd\bar{3}m$) with successive oxygen loss during thermal treatment. On the contrary, oxygen would be inserted into the host structure during synthesis of LLOs starting from a mixture of the precursor and lithium source (Li_2CO_3).

It is the original formation mechanism of LLOs that inspires to develop a promising and practical method, a coprecipitation route followed by a microwave heating process, for controllable synthesis of the layered monoclinic $Li[Li_{0.2}Ni_{0.2}Mn_{0.6}]O_2$ cathode materials with high rate performance (i.e. a specific discharge capacity of 171 mAh g^{-1} at 10 C). An increased oxidation of transition metal cations during high-temperature lithium insertion process reveals that oxygen atoms are continuously inserted into the host structure to keep charge neutrality and provide the open coordination sites for incorporated lithium ions and relocated TM ions during preparation of LLOs. The high-temperature lithiation reaction is accompanied by phase transition, atomic rearrangement, and surface reconstruction.

Despite the fact that the synthesized monoclinic $Li[Li_{0.2}Ni_{0.2}Mn_{0.6}]O_2$ cathode could deliver a good rate performance, it suffers from a serious voltage decay during electrochemical cycling. Therefore, *in situ* high-resolution SRD was carried out in order to understand the structural evolution of the Li-excess layered electrode during electrochemical cycling and to figure out what are the important factors responsible for the degradation of LLOs. The *in situ* SRD results suggest that the nanodomain formation of a layered phase and a spinel-like phase after charging to high voltages (above 4.5 V) is the main contributing factor for the structural instability. The fatigue crack in the electrode material after prolonged cycling is directly observed by high-resolution transmission electron microscopy (HRTEM), which is ascribed to the volume variation induced by anisotropic lattice strain during the delithiation/lithiation process.

To better understand the relationship between the formation mechanism and degradation mechanism of LLOs, a series of $Li_xNi_{0.2}Mn_{0.6}O_y$ oxides with a large variety of provided lithium contents ($0.00 \leq x \leq 1.52$) was prepared via a thermal treatment. The consistent results demonstrate that the structural properties of $Li_xNi_{0.2}Mn_{0.6}O_y$ oxides are strongly dependent on the chemical composition with respect to lithium and oxygen. The Li-excess layered $Li[Li_{0.2}Ni_{0.2}Mn_{0.6}]O_2$ oxide is only stable when a considerable amount of lithium and oxygen is available during synthesis, while at a lower concentration of them, the spinel/rock-salt-type phase is thermally stable. These findings offer new insights into the nature of fatigue processes in LLOs.

Due to fact that the competition between thermally-induced oxygen loss and lithium-insertion-induced oxygen uptake occurs, the high-temperature reaction of the precursor and lithium source gets much more complicated. Lastly, *in situ* high-temperature SRD technique was utilized to explore the chemically (i.e. Li & O) induced structural evolution for the pure spinel oxide ($Fd\bar{3}m$), so as to provide a guarantee of reliable lithiation reaction mechanism with oxygen uptake. The original formation mechanism of Li-containing oxides indicates that the Li-excess layered oxides can be formed as a result of lithium and oxygen insertion into the spinel ($Fd\bar{3}m$) and/or Li-containing rock-salt-type phase ($Fm\bar{3}m$) during synthesis at air atmosphere. If a small amount of lithium is provided, lithium atoms have a tendency to be located on tetrahedral positions, forming the Li-containing spinel oxides. As more lithium ions are gradually incorporated into the spinel matrix, lithium atoms tend to preferentially occupy the octahedral sites forming Li-containing rock-salt-type phase and/or Li-rich layered phase. Because the oxygen anion cubic close-packed

lattice is involved during phase transformation, oxygen atoms are supposed to be inserted only into the oxygen lattice at the surface, associated with crystal growth and/or recrystallization.

These discoveries not only contribute to a comprehensive understanding of the correlation between preparation, structure and performance for next-generation LIBs, but also provide new insights into the interaction of oxygen with lithium in Li-containing oxides during synthesis and electrochemical cycling.

1 Motivation & Outline

Nowadays, the ever-increasing energy crisis and global climate change make it significant to build a cleaner and better world for human beings. Lithium ion batteries (LIBs) have been considered to be of great importance as environmentally friendly energy sources for electrical energy storage such as portable devices and large scale battery applications in modern civilization.[1–3] However, as technology creates more functional portable devices, electric vehicles (EV), and power tools, there is a large-scale demand for next-generation LIBs with high power density, high energy density, long cycle life, and low cost.

Advanced cathode materials that can deliver high electrochemical performance are the core components in the next-generation LIBs because the energy density, the lifetime and the price of LIBs are mainly determined by cathode materials.[4,5] Instead of $LiCoO_2$ and $LiNi_xCo_yMn_{1-x-y}O_2$ (NCM) cathode materials, used widely in commercial LIBs, lithium-rich layered oxides (LLOs; $Li[Li_xTM_y]O_2$, TM = 3*d*-tansition metals) have been explored as one of the most promising cathode candidates for high-energy LIBs in recent years.[6,7] Generally, the capacity of conventional cathode materials (e.g., NCM) is limited by the oxidation-reduction reactions of TM cations. Interestingly, the cationic and anionic redox processes in LLOs (space group $C2/m$ and/or $R\bar{3}m$) could allow storage/release of a larger amount of electrons and lithium ions, and hence result in a huge improvement in energy storage capacity (delivering 50 % excess capacity beyond traditionally used cathodes).[8–10]

Exploring the origin of oxygen redox mechanisms has become essential for next-generation LIBs. For example, Tarascon et al. reported that the formation of peroxo-like O_2^{n-} ($1 \leq n \leq 3$) dimers is mainly responsible for the excess capacity in Ru-based Li-rich intercalation oxides.[11,12] However, in contrast to that, Bruce and co-workers suggested that the lithium-driven generation of localized electron-hole on oxygen atoms contributes to the high capacity for 3*d*-TM-oxide insertion compounds.[13] Although the origin of oxygen redox reaction is not completely elucidated, it is found that the oxygen would be released during long-term cycling, concomitant with irreversible lithium loss.[14,15] As the release of oxygen and/or lithium proceeds, the composition-induced phase transition from layered LLOs to spinel phase ($Fd\bar{3}m$) and/or rock-salt-type phase ($Fm\bar{3}m$) is accelerated during prolonged cycling.[16,17]

Up to now, the oxygen redox and oxygen loss in LLOs have been intensively discussed in battery research. Unfortunately, the investigation of oxygen incorporation during synthesis of LLOs has not been addressed sufficiently so far. For instance, Cao et al. suggested that the release of oxygen from spinel structure could promote the formation of Li-rich layered crystals.[18] However, such oxygen loss can only be rationally understood as the generation of oxygen vacancy (i.e. a tiny amount of oxygen release) during transition from spinel to layered phase. It is evident that both lithium and oxygen are incorporated into spinel architecture to produce Li-containing layered oxides (e.g., $1/3\ Co_3O_4 + 1/2\ Li_2O + 1/12\ O_2 \xrightarrow{\Delta} LiCoO_2$ [19]). Since the difference between spinel and layered structure is determined by the arrangement of Li and TM ions in each metal layer, the question which should be raised is: how is oxygen inserted into the crystal structure during synthesis from precursors to final LLOs. Uncovering the origin of oxygen incorporation during high-temperature lithiation reaction, therefore, is necessary to fully use the LLOs for practical purposes.

Therefore, the objective of this PhD thesis is to understand the nature of lithium- and oxygen-driven structural evolution in $Li_xNi_{0.2}Mn_{0.6}O_y$ ($0.00 \leq x \leq 1.52$) oxides for next-generation LIBs. The research work can be divided into six parts:

(1) The first part is to study the physicochemical properties of the precursors obtained by hydroxide coprecipitation method.

(2) The second part is to explore the original formation mechanism of LLOs starting from the precursors.

(3) The third part is to controllably prepare high-energy LLOs with excellent performance using a one-step and practical synthetic technology, i.e. a fast hydroxide co-precipitation method coupled with microwave annealing process.

(4) In the next part, the degradation mechanism of prepared LLOs after long-term cycling will be investigated.

(5) The fifth section is to study the thermally stable phase of $Li_xNi_{0.2}Mn_{0.6}O_y$ oxides.

(6) The last part is to reveal the mechanism of lithium/oxygen incorporation into the pure spinel matrix.

This PhD thesis consists of six chapters. **Chapter 2** gives a brief description of lithium ion batteries and cathode materials. **Chapter 3** generally describes the basic concepts and principles of the synthetic method used in this research. **Chapter 4** introduces the materials synthesis,

materials characterization and electrochemical measurement. In **chapter 5**, the details on the results, discussions and conclusions of this research will be presented. **Chapter 6** summarizes the work and recommends the strategy for further studies.

2 Fundamentals of lithium ion secondary batteries

Rechargeable lithium ion batteries (LIBs) are constructed in order to convert chemical energy into electrical energy and vice versa. These batteries usually consist of a cathode and an anode separated by a separator and an electrolyte. During cycling, lithium ions are inserted/extracted into/from an electrode host, whereas electrons pass through an external circuit. In this chapter, a general description of the fundamental components of LIBs is provided.

2.1 Basic concepts of lithium ion batteries

In a LIB, lithium ions are shuttled back and forth between cathode and anode through an electrochemical redox process within the electrode materials, involving a charge compensation mechanism, see Figure 2.1. The battery mainly consists of a cathode (positive electrode), an anode (negative electrode) and an electrolyte. Graphite or metallic lithium are usually used as anode, while various oxides and phosphates of transition metals typically serve as cathode. During discharge process, lithium ions are released from the anode and travel to the cathode through an electrolyte. Meanwhile the anode is oxidized and supplied electrons to external circuit with a reduction of the chemical potential of Li^+ at the individual electrodes. When the battery is charged, lithium ions are intercalated back into the anode by an externally imposed potential. The capacity of the electrode is then limited by the number of electrons and lithium ions that can participate in the intercalation reaction. Both, cathode and anode, must be ionically and electronically conducting. The electrolyte, which is commonly a lithium salt dissolved in an organic solvent, must possess high ionic conductivity but be an electronic insulator.

Until now, $LiCoO_2$ and graphite are the most widely used cathode and anode materials in a LIB, the redox reaction during electrochemical process is shown below.

$$\text{Anode: } 6C + x\text{Li}^+ + xe^- \rightleftharpoons \text{Li}_x C_6 \tag{2.1}$$

$$\text{Cathode: } \text{Li}_{1-x}\text{CoO}_2 + x\text{Li}^+ + xe^- \rightleftharpoons \text{LiCoO}_2 \tag{2.2}$$

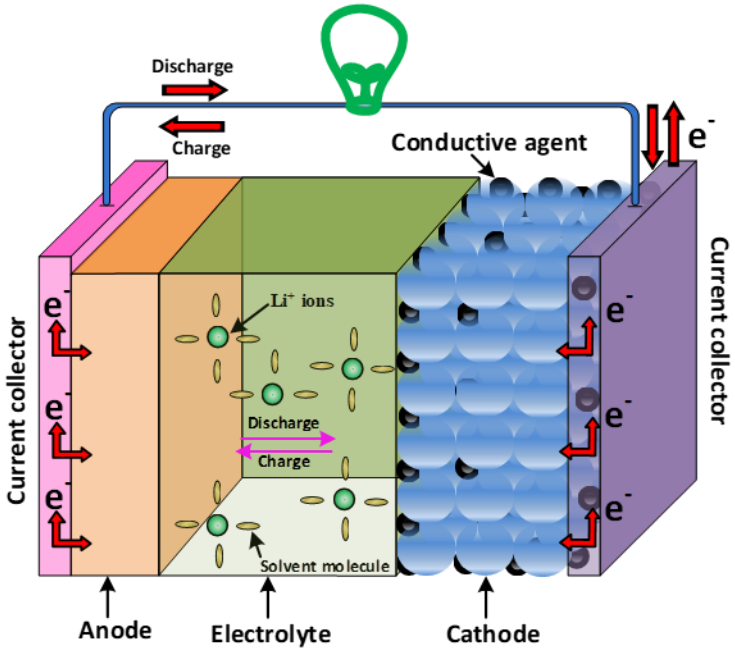

Figure 2.1 Schematic of a secondary lithium ion battery.

The driving force for the oxidation-reduction reaction is determined by the difference in Gibbs free energy between positive electrode and negative electrode [20]:

$$\Delta G = -nFE \quad \text{or} \quad \Delta G^0 = -nFE^0 \tag{2.3}$$

where ΔG^0 is the standard Gibbs free energy, n is the number of electrons, F is Faraday constant (96485.3 C/mol or 26.801 Ah/mol), E is the cell voltage under non-standard conditions, and E^0 is standard battery potential (at 25 ^{o}C temperature and 1 bar pressure). The non-standard Gibbs free energy, ΔG, can be expressed by van't Hoff isotherm as:

$$\Delta G = \Delta G^0 + RT\ln a \tag{2.4}$$

where R is universal gas constant (8.314 J mol^{-1} K^{-1}), T is absolute temperature and a is the ratio of chemical activities of products and reactants. If no external potential is applied, the equilibrium potential of the electrode (E_{eq}) is derived from the Nernst equation assuming a general redox reaction $a\text{A} + b\text{B} \rightleftharpoons c\text{C} + d\text{D}$:

$$E_{\text{eq}} = E^0 - \frac{RT}{nF}\ln a = E^0 - \frac{RT}{nF}\ln\left(\frac{\{C\}^c\{D\}^d}{\{A\}^a\{B\}^b}\right) \tag{2.5}$$

where $\{A\}$, $\{B\}$, $\{C\}$, $\{D\}$, and a, b, c, d are the chemical activities and the numbers of moles in a system, respectively. When the current flows inside a circuit, the electrochemical reactions are also affected by various kinetic impedances such as the activation energy of the redox reaction (reaction overpotential), the depletion of charge-carriers at electrode surface (concentration overpotential)

and resistance of all cell components (resistance overpotential). The voltage difference between the observed experimental potential (E) and the redox reaction equilibrium potential (E_{eq}) is defined as polarization and quantified in terms of an overpotential, $\eta_s = E - E_{\mathrm{eq}}$. This overpotential is dependent on the electrical current through a Butler–Volmer equation:

$$j = j_0[\exp\left(\frac{nF\alpha_a\eta_s}{RT}\right) - \exp\left(\frac{-nF\alpha_c\eta_s}{RT}\right)] \quad (2.6)$$

where j is electrode current density (defined as $j = i/A$, i is current and A is the surface area of the electrode), j_0 is the exchange current density, R is gas constant, T is temperature, n is the number of electrons transferred in the electrode reaction, F is Faraday constant, α_a and α_c are the cathodic and anodic charge transfer coefficient, respectively. In order to normalize to the active material capacity, discharge current is often described as C-rate (mA g^{-1}), which is an indicator of current density at which a cell is fully discharged in relation to its maximum capacity. In other words, a battery is discharged in x hours at a rate of x^{-1} C.

The choice of the electrode materials is very important in the electrochemical property of a battery, since the lithium deintercalation/intercalation reaction is intimately tied to the intrinsic properties of electrode materials. Improvements to the following key parameters are needed to develop advanced electrode materials for next-generation LIBs:

- High gravimetric/volumetric energy density
- High rate capability (power density)
- Long cycleability (stability)
- Low cost
- High safety
- Low toxicity (environmentally friendly)

2.2 Important characteristics for lithium ion batteries

2.2.1 Energy density and specific energy density

The volumetric energy density, sometimes referred to as the energy density, is defined as the nominal battery energy per unit volume (Wh L^{-1}). Gravimetric energy density (i.e. specific energy) is another characteristic of the battery chemistry and packing. It can be calculated using the following equation [21,22]:

$$E_S = \frac{1}{m}\int_0^\tau v(t)\, i(t)\mathrm{d}t \qquad [\mathrm{Wh\ kg^{-1}}] \qquad (2.7)$$

where E_S is the specific energy density, $v(t)$ and $i(t)$ are respectively the voltage and current as a function of time (t), τ is the total time, m is the mass of the devices.

With respect to electrode, the theoretical specific capacity (C_T) is the amount of charge ($Q = \int i(t)\mathrm{d}t$) involved in the electrochemical reaction process per unit weight. It is expressed by Faraday's law:

$$C_T = \frac{\Delta x \cdot F}{M_w} \times \frac{1000}{3600} \qquad [\mathrm{Ah\ kg^{-1}\ or\ mAh\ g^{-1}}] \qquad (2.8)$$

where Δx is the number of moles of lithium ions that could participate in the reaction, m is the mass of the active material used in the electrode, M_w is the molar mass of the electode material and F is Faraday constant. Δx depends on the physicochemical properties of electrode compounds. For instance, theoretical specific capacity of $LiCoO_2$ is 274 mAh g^{-1} ($\Delta x = 1$). Only around 50 % of lithium ions can be reversibly intercalated and deintercalated into the structure of $LiCoO_2$ without significant structural instability, resulting in a low practical specific capacity (~ 140 mAh g^{-1}). The practical specific capacity (C_P) can be calculated by the electrochemical test:

$$C_P = \frac{\int_{\tau_1}^{\tau_2} i(t)\mathrm{d}t}{m} \qquad [\mathrm{mAh\ g^{-1}}] \qquad (2.9)$$

where τ_1 and τ_2 are the reaction time to reach the cut-off potential.

If the current is constant during discharging, E_S of the electrode can be deduced as follows:

$$E_S = \int_{V_1}^{V_2} C(v)\,\mathrm{d}v \qquad [\mathrm{Wh\ kg^{-1}}] \qquad (2.10)$$

Therefore, the specific energy is equal to a product of the battery potential and the specific capacity.

2.2.2 Power density and specific power density

The power density of a cell is the maximum available power per unit volume, W L^{-1}. The specific power density (P_S) is the amount of power that a battery can deliver per unit weight:

$$P_S = \frac{1}{m}\int_0^\tau i(v)\mathrm{d}v \qquad [\mathrm{W\ kg^{-1}}] \qquad (2.11)$$

It can be simply obtained by the specific energy density divided by the discharging time (τ):

$$P_S = \frac{E_S}{\tau} \qquad [\mathrm{W\ kg^{-1}}] \qquad (2.12)$$

The specific power density of a battery is determined by the dynamic factors including the conductivity of lithium ions and electrons in the electrode, lithium motion at the interface between

electrode and electrolyte, intrinsic ohmic resistance from battery geometry, lithium ion diffusion in the electrolyte and so on. Among them, lithium ion diffusion in the solid electrode materials and charge transfer at the interface are considered to be crucial in the rate capability of the batteries. Generally, lithium ion diffusivity (D_{Li}) in solids is temperature dependent and can be expressed by the Arrhenius equation:

$$D_{\mathrm{Li}} = D_0 \exp\left(\frac{-\Delta G_{\mathrm{d}}}{k_{\mathrm{B}} T}\right) \tag{2.13}$$

wherein ΔG_{d} is the activation energy for the movement of lithium ions, k_{B} is the Boltzmann's constant, D_0 is the kinetic prefactor and T is the absolute temperature. The diffusion time (τ) of lithium ions in electrode materials is related to the D_{Li} and the ionic diffusion length (L):

$$\tau \propto \frac{L^2}{D_{\mathrm{Li}}} \tag{2.14}$$

Thus, in order to enhance the rate capability of electrode materials, it is essential to reduce the energy barrier for lithium ion diffusion and shorten the electronic/ionic transport length.

2.2.3 Long cycleability

Cycle life is the number of charge and discharge cycles that a cell is able to support before the battery cannot meet specific performance criteria. The cycleability of a cell is generally affected by current density, formation of stable solid electrolyte interphase (SEI) layer, depth of discharge (DOD), stability of electrode and electrolyte, and by other operating conditions such as temperature and humidity. Most of all, the structural stability of electrode material has a pronounced influence upon the cycle life of a battery.

2.2.4 Safety, cost and toxicity

Since LIBs were commercialized by Sony in 1991, along with them are the potential safety risks. If the batteries are not carefully designed or fabricated, they will have the potential to be dangerous. That may include fire, explosion and emission of toxic fumes. The scientists and engineers achieve a high safety battery by limiting the amount of active material, introducing various safety mechanisms and adding the electronic protection circuit within the battery pack. In the quest for high-power and high-energy batteries, highly reactive chemicals have been utilized to provide the high energy densities but they tend to increase the risk of danger in case of physical damages.

The cost of LIBs is a significant performance metric for fabricating and management analysis. A rapid drop in the battery prices could create a condition for further adoption of LIBs in industries and society itself. New research suggests that prices for LIBs will fall in coming years,[23] see Figure 2.2. In general, a process-based model is employed to calculate costs for batteries (e.g., dollars per kWh). The cost of a battery is dominated by materials cost presenting approximately 74 % of the total cell cost, in which cathode materials comprise ~ 30 % of the overall materials cost.[5,24]

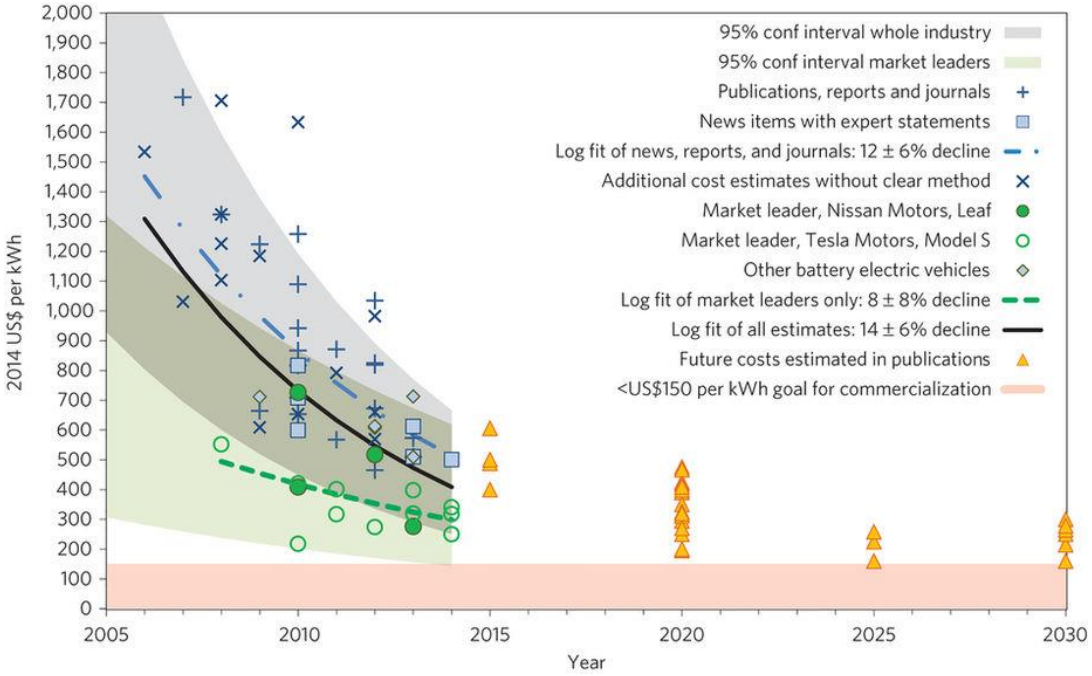

Figure 2.2 Cost of LIB packs in electric vehicles (EV).[23]

In case of accidents, LIBs were found to leak dozens of poisonous gases that are profoundly detrimental to human health and environment. The state of charge (SOC), DOD, and chemicals contained in the cells can affect the concentrations and species of toxic gases released. For example, a fully charged battery will produce more dangerous gases than a battery at a half charged state.

2.3 Cathode materials for lithium ion batteries

As a positive electrode material in a LIB, the compound should be able to accommodate mobile species such as lithium ions. Olivine $LiFePO_4$, layered $LiCoO_2$, and spinel $LiMn_2O_4$ are the current commercialized cathode materials which have open one dimensional (1D), 2D and 3D channels

for lithium ion migration, respectively. Figure 2.3 shows the crystal structures of these typical positive electrode materials. Olivine $LiFePO_4$ has an olivine structure (*Pnma* space group), in which the hexagonal close-packed (hcp) arrayed oxygen forms octahedral (LiO_6 and FeO_6) and tetrahedral (PO_4) positions. The $LiFePO_4$ cathode material belongs to the olivine framework family that can deliver a good structural stability but its rate capability is limited by the 1D lithium ion pathway and poor electronic conductivity.[25,26] Oxygen in the structure of $LiCoO_2$ ($R\bar{3}m$) forms face-centered cubic (fcc) lattice, which is also called cubic-close-packed (ccp) oxygen array, with Co and Li occupying the octahedral positions. The oxygen planes are stacked alternatingly in a sequential way of ABCABC, which is called layered O3-structure. Lithium ions move within the lithium layer through a 2D diffusion pathway.[27,28] With respect to the structure of $LiMn_2O_4$ ($Fd\bar{3}m$), oxygen also forms a ccp lattice with MnO_6 octahedra and LiO_4 tetrahedra. The structure provides 3D lithium ion diffusion channels, guaranteeing a rapid intercalation-deintercalation reaction.[29,30] Therefore, the electrochemical reaction of the electrode material is mainly dependent on the mobility of lithium ions and the electrical conductivity in the host crystal structure.

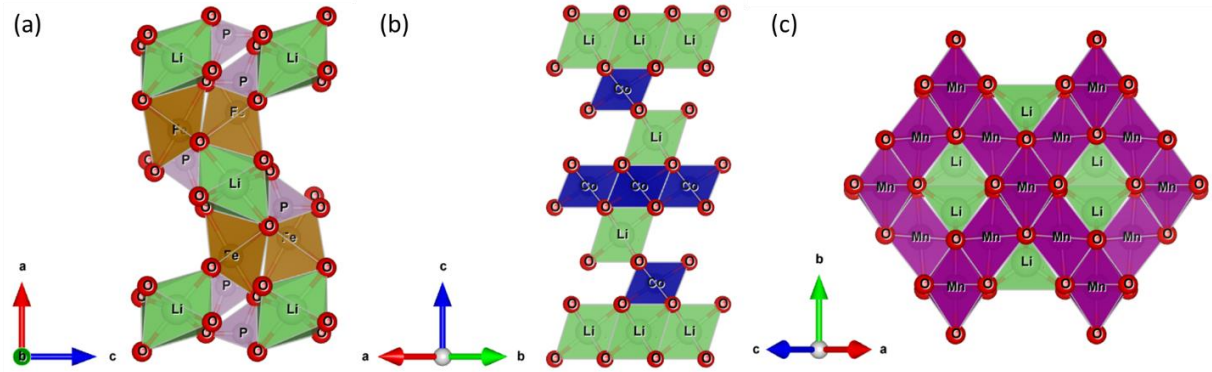

Figure 2.3 Crystal structure of (a) $LiFePO_4$, (b) $LiCoO_2$ and (c) $LiMn_2O_4$.

Among the conventional cathode materials, $LiCoO_2$ with a rhombohedral structure ($R\bar{3}m$ space group) was the first to be employed as a cathode material for LIB, and has been widely used over the past two decades because of its easy preparation and fast lithium ion intercalation. However, only half of lithium can be extracted from $LiCoO_2$ for practical operation due to many factors such as structural instability and safety. Instead of $LiCoO_2$, layered $LiNi_xCo_yMn_{1-x-y}O_2$ and layered Li-rich $Li[Li_{1/3-2x/3}M_xMn_{2/3-x/3}]O_2$ (M = Ni or/and Co) compounds have been developed recently for next-generation LIBs.

2.3.1 Layered Li-stoichiometric transition metal oxides

$LiNi_xCo_yMn_{1-x-y}O_2$ ($0 \leq x \leq 1$, $0 \leq y \leq 1$, NCM) are isostructural with $LiCoO_2$, they have a α-$NaFeO_2$-type layered rhombohedral structure with the space group of $R\bar{3}m$. The lithium atoms are located at 3*a* (0, 0, 0) position in the lithium layer, transitional metal (TM) atoms are placed at 3*b* (0, 0, 0.5) position in the TM slab, and the oxygen atoms are located at 6*c* (0, 0, *z*), $z < 0.25$, position forming the edge-sharing TMO_6 and LiO_6 octahedra, as shown in Figure 2.4. The lithium ions are positioned at lattice sites surrounded by the dense layers of edge-sharing octahedra TMO_6, resulting in a 2D pathway for lithium ions within the *ab* plane. Li^+/Ni^{2+} mixing between the transitional metal slab and the lithium slab widely exists in the series of NCM compounds since the similar ionic size of Li^+ and Ni^{2+}, which will seriously affect the activation energy barriers for lithium ion migration and thus the electrochemical performance.[3,31]

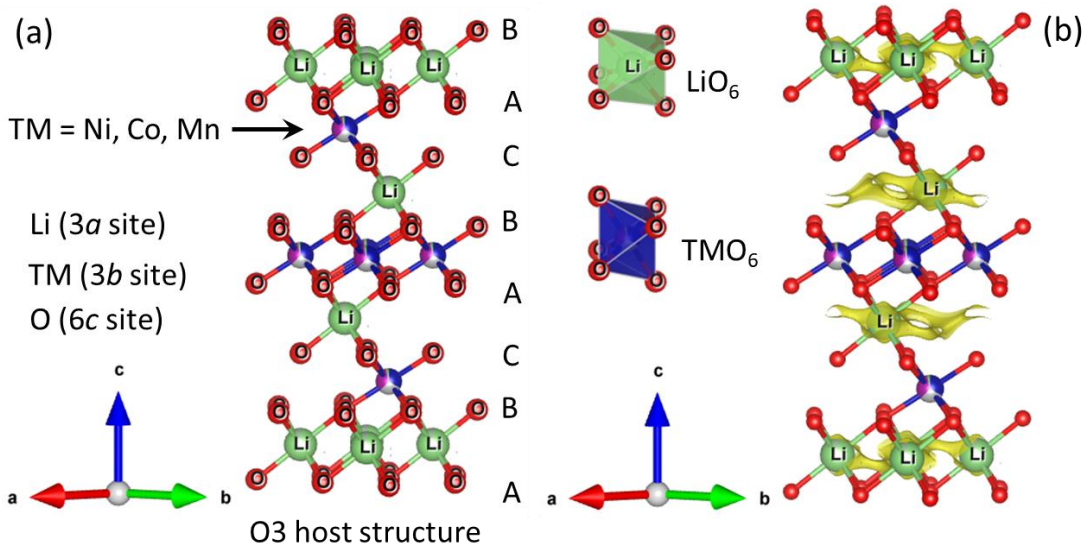

Figure 2.4 Schematics of (a) crystal structure of $LiNi_{1/3}Co_{1/3}Mn_{1/3}O_2$ and (b) a possible lithium ion pathway in $LiNi_{1/3}Co_{1/3}Mn_{1/3}O_2$.

The electrochemical properties of NCM materials are correlated with the composition of Ni, Co and Mn in the structure. Generally, high Ni content contributes to the improvement of specific capacity, high Co concentration enhances the rate capability and high Mn improves the structural stability. For example, the oxidation state of Ni, Co and Mn in $LiNi_{1/3}Co_{1/3}Mn_{1/3}O_2$ is +2, +3 and +4, respectively. Only divalent Ni ($t_{2g}^6e_g^2$) and trivalent Co ($t_{2g}^6e_g^0$) are electrochemically active through the Ni^{2+} ($t_{2g}^6e_g^2$) / Ni^{4+} ($t_{2g}^6e_g^0$) and Co^{3+} ($t_{2g}^6e_g^0$) / Co^{4+} ($t_{2g}^5e_g^0$) redox reactions, while Mn^{4+} ($t_{2g}^3e_g^0$) is very stable in the octaheral coordination because of its half filled t_{2g} and empty e_g orbitals,[32] see Figure 2.5 and Figure 2.6.

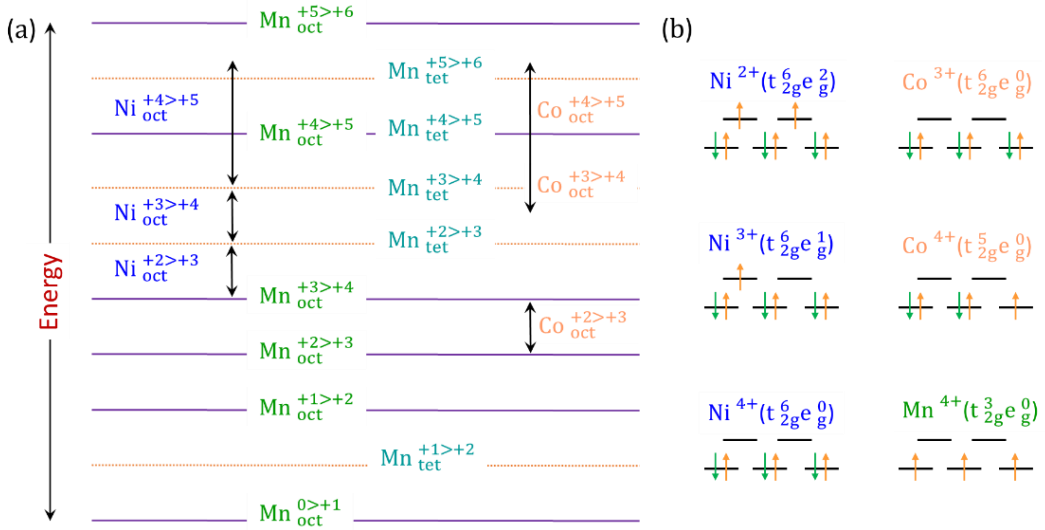

Figure 2.5 (a) The ionization energies of Ni, Co and Mn elements at various valence states in an oxide framework and (b) electronic configurations of various ions.[33] *Oct and tet represent the octahedral and tetrahedral coordination, respectively, Ni^{2+} and Mn^{4+} in the structure have high-spin configurations.*

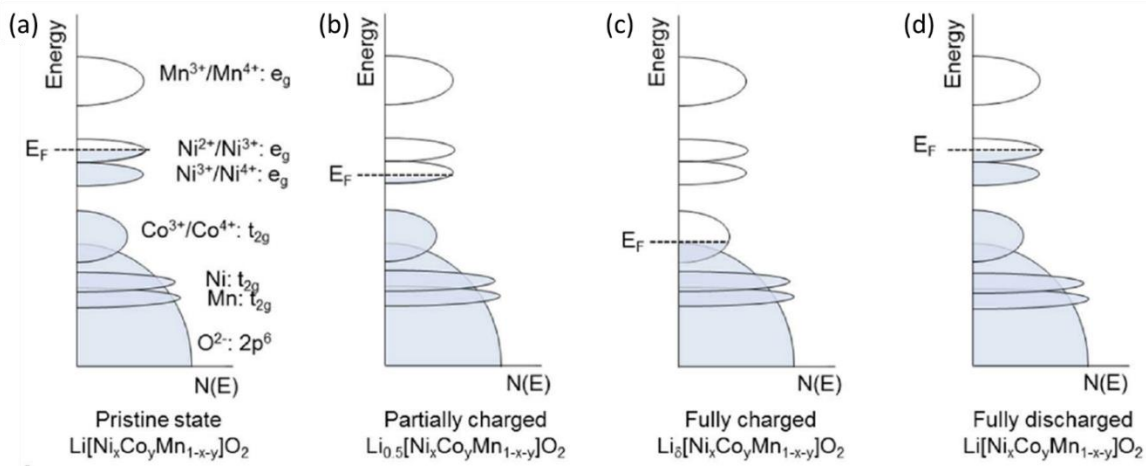

Figure 2.6 Schematic electronic density of states (DOS) of NCM cathode material at different SOC.[34]

The electrochemical activity of NCM materials is also determined by the energy level and density of their available electronic states. In layered NCM cathode materials, electrons localized in the *d* bands of transitional metal cations and/or the *p* electrons of oxygen anions participate in the oxidation-reduction reaction, and lithium ions are synchronously intercalated/deintercalated into/from the open host structure. When the $LiNi_{1/3}Co_{1/3}Mn_{1/3}O_2$ material is fully charged, the TM *d* electrons with higher energy states are sufficient to compensate for the loss of electrons.[34] Thus, the Fermi level (E_F) changes within the energy level of transitional metal *d* bands during the redox reaction (Figure 2.6).

2.3.2 Layered Li-rich transition metal oxides

Lithium-rich layered oxides (LLOs) are a class of layered cathode materials, the competitive advantages of LLOs are that they exhibit a high reversible capacity (> 250 mAh g^{-1}) and a low cost.[35–37] LLOs are generally notated as $xLi_2MnO_3 \cdot (1\text{-}x)LiTMO_2$ or standard layered formula of $Li_{1+x}TM_{1-x}O_2$. The crystallographic (real-)structure of LLOs can correspondingly be expressed as the following two models: (1) nanoscale coexistence of lithium-rich monoclinic Li_2MnO_3 phase ($C2/m$) and rhombohedral phase ($R\bar{3}m$ space group) with a ratio of $x/(1\text{-}x)$; and (2) a single monoclinic $\cdot Li[Li_{1/3-2x/3}M_xMn_{2/3-x/3}]O_2$ phase with excess Li ions incorporated in the TM layer (Figure 2.7).[38,39] There has been a long debate concerning whether the structure of pristine materials is a nanocomposite of two phases or a solid solution. Both structural models possess an O3-type structure and resemble each other crystallographically. Most of the reflections in typical X-ray diffraction patterns of LLO materials can be indexed by rhombohedral phase ($R\bar{3}m$) and only a few weak reflections are attributed to the superstructures according to monoclinic symmetry.[6,40] These superlattices originate from the in-plane Li/TM ordering induced by the excess lithium ions located in the TM layer, where one lithium is surround by six transition metals forming a honeycomb structure.[34]

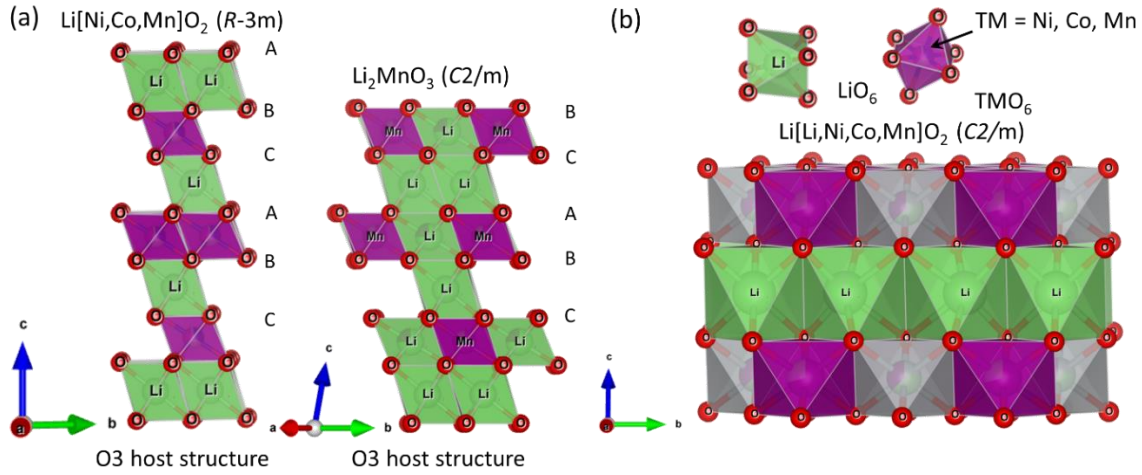

Figure 2.7 Schematic illustration of crystallographic structure: (a) a composition of trigonal phase ($R\bar{3}m$) and monoclinic Li_2MnO_3 phase ($C2/m$), and (b) a single monoclinic $Li[Li_{1/3-2x/3}TM_xMn_{2/3-x/3}]O_2$ phase.

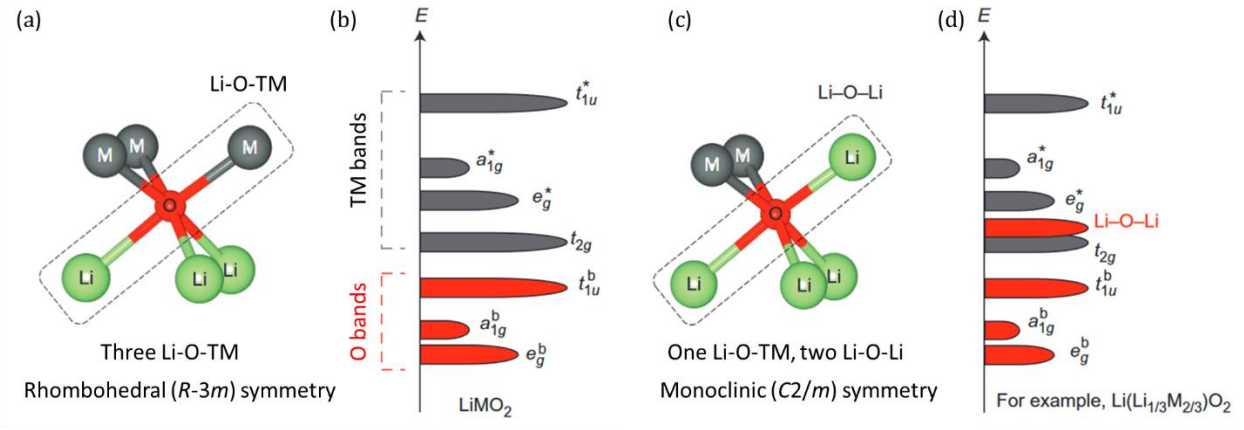

Figure 2.8. Local atomic coordination around oxygen in (a) rhombohedral NCM ($R\bar{3}m$) and (c) monoclinic Li_2MnO_3, and schematic of band structure for (b) layered NCM and (d) Li-rich materials.[10]

Up to now, the commercially used cathode materials in LIBs have a high theoretical specific capacity (C_T), i.e., $LiFePO_4$ (C_T = 170 mAh g^{-1}), $LiCoO_2$ (C_T = 274 mAh g^{-1}), $LiNi_{1/3}Co_{1/3}Mn_{1/3}O_2$ (C_T = 278 mAh g^{-1}), $LiNi_{0.8}Co_{0.15}Mn_{0.05}O_2$ (C_T = 279 mAh g^{-1}), and $LiMn_2O_4$ (C_T = 148 mAh g^{-1}), but their practical specific capacity (C_P) remains at 100-180 mAh g^{-1}. Interestingly, the reported LLOs could deliver a high reversible specific capacity exceeding 250 mAh g^{-1}, which far surpasses the C_T values obtained on the basis of the redox capabilities of TM ions. For instance, Ni^{2+} ($t_{2g}^6e_g^2$) / Ni^{4+} ($t_{2g}^6e_g^0$) redox can only compensate for 0.4 Li ion extraction in $Li_{1.2}Ni_{0.2}Mn_{0.6}O_2$. Intensive studies have been conducted to understand the unique electrochemical property of LLOs. Redox mechanism [41,42] and structural transformation mechanism [43–45] were proposed to unravel the high capacity and the voltage decay of LLOs during electrochemical operation. The TM *d* bands overlap with the O *p* bands in the electronic DOS of LLOs, when E_F shifts to the top of O *p* bands, oxygen electrons can participate in the delithiation process.[41,46] As an example of LLOs, Li_2MnO_3 is composed of a lithium plane and a transition metal plane comprising additional lithium ions. The TM slab contains lithium and manganese ions in an atomic ratio of 1:2, where one lithium atom is coordinated to six manganese atoms. As a result, the local coordination around oxygen consists of one Li-O-Li and two Li-O-Mn configurations in Li_2MnO_3 and the energy of un-hybridized Li-O-Li state is higher than hybridized O 2*p* states leading to an easy release of electrons.[42]

2.3.3 Spinel-based transition metal oxides

Spinel based cathode materials are another promising active material for LIBs due to the high operating voltage and the 3D framework for fast lithium ion diffusion.[37,47,48] A general formula of spinel structure ($Fd\bar{3}m$) is AB_2O_4, the A ions (i.e. Li) occupy the tetrahedral 8*a* sites, B ions are placed in octahedral 16*d* sites, and oxygen atoms are occupying 32*e* positions forming a fcc packing. The octahedral 16*c* position is unoccupied and provides a zigzag pathway (8*a*-16*c*-8*a*-16*c*) for lithium ion migration, see Figure 2.9. The typical intercalation compounds of this class are $LiMn_2O_4$ and $LiNi_{0.5}Mn_{1.5}O_4$.

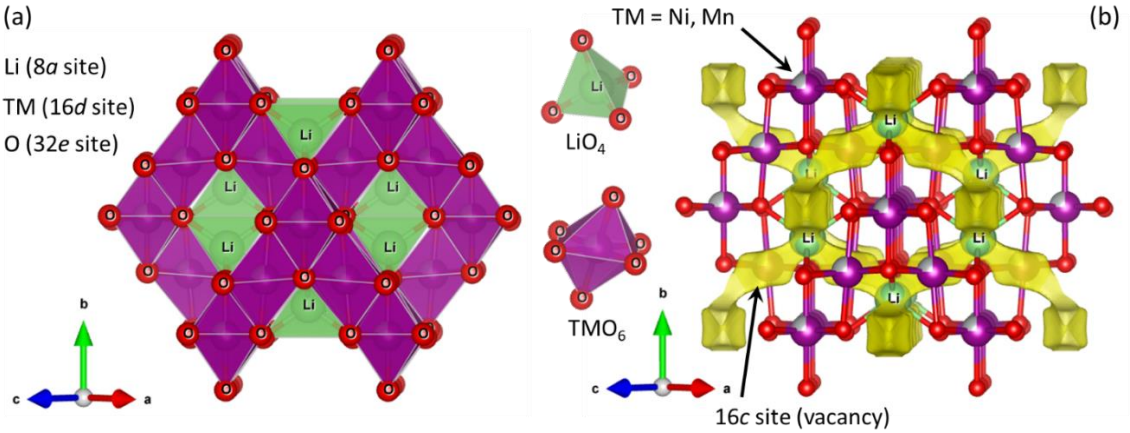

Figure 2.9 Schematics of (a) crystal structure of $LiNi_{0.5}Mn_{1.5}O_4$, and (b) possible lithium ion pathway with the isosurface of ΔBVS (bond valence sum, value = 0.2) along 8a-16c-8a-16c path in the structure of bulk $LiNi_{0.5}Mn_{1.5}O_4$.

The Mn^{3+} ion usually has a d^4 ($t_{2g}^3 e_g^1$) high spin electronic structure, the single electron with doubly degenerate e_g orbitals results in a local Jahn-Teller distortion in $LiMn_2O_4$ (Figure2.10). The Jahn-Teller distortion has a direct effect on the orbital energies and Mn-O bond lengths.[49] In essence, the Jahn-teller distortion reduces the e_g orbital energy and increases the energy level of t_{2g} band which lead to a total lowering of energy. When the e_g electron is occupying the d_{z^2} orbital, the Mn-O bond lengths on *z* axis of MnO_6 octahedra are increased while the Mn-O bond lengths on *x* and *y* axes are decreased (i.e. an elongated Jahn-Teller distortion). On the contrary, a compressed Jahn-Teller distortion is formed if the single e_g electron occupies the $d_{x^2-y^2}$ orbital, as a consequence of an enlargement of Mn-O bond lengths on *x* and *y* axes, and a shortening of Mn-O bond lengths on the *z* axis.[50]

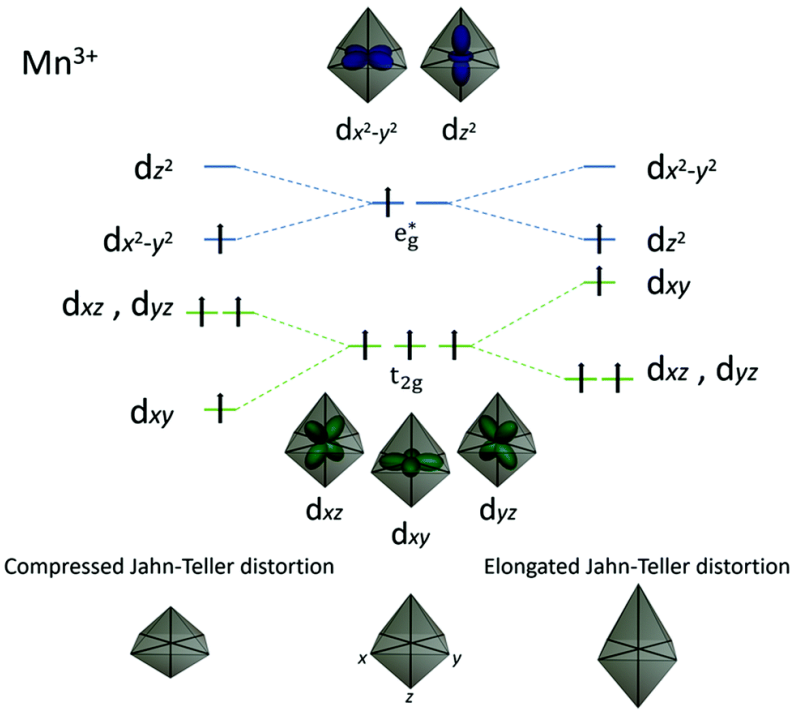

Figure 2.10 The typical Jahn-Teller distortion of a octahedral Mn^{3+} complex.[51]

In order to circumvent Jahn-Teller effect, considerable efforts have been performed to increase the concentration of Mn^{4+} in the spinel structure of $Li[M_xMn_{2-x}]O_4$ (M = Ni, Cr, Co, Fe, etc. $0 < x < 1$).[52–54] Spinel $LiNi_{0.5}Mn_{1.5}O_4$ is one of the most promising cathode materials because of its high voltage (4.7 V vs. Li/Li^+) and high power density. In the stoichiometric $LiNi_{0.5}Mn_{1.5}O_4$, Ni and Mn elements exist in the form of Ni^{2+} ($t_{2g}^6e_g^2$) and Mn^{4+} ($t_{2g}^3e_g^0$), respectively. Two different structures (i.e. cation ordered/disordered spinel phase) for $LiNi_{0.5}Mn_{1.5}O_4$ can be prepared by various synthesis routes. Both of them have a cubic spinel structure, the Ni and Mn ions are regularly distributed at 4*b* and 12*d* sites in the ordered $LiNi_{0.5}Mn_{1.5}O_4$ ($P4_332$ space group), but Ni and Mn ions are randomly located at 16*d* sites in the disordered $LiNi_{0.5}Mn_{1.5}O_4$ ($Fd\bar{3}m$ space group). According to the literature,[54–56] the disordered spinel phase delivers a superior electrochemical performance compared to the ordered one. Lithium ions can be extracted/inserted from/into the disordered spinel structure at about 4.7 V according to the redox reaction:

$$\begin{aligned} Li^{1+}Ni_{0.5}^{2+}Mn_{1.5}^{4+}O_4^{2-}(Fd\bar{3}m) &\rightleftharpoons Li_{0.5}^{1+}Ni_{0.5}^{3+}Mn_{1.5}^{4+}O_4^{2-}(Fd\bar{3}m) + 0.5Li^+ + 0.5e^- \\ &\rightleftharpoons Ni_{0.5}^{4+}Mn_{1.5}^{4+}O_4^{2-}(Fd\bar{3}m) + Li^+ + e^- \end{aligned} \quad (2.15)$$

Another electrochemical reaction process takes place at around 2.7 V and is related to a gradual intercalation of more lithium ions into the unoccupied 16*c* octahedral sites in the cubic spinel

structure. In this 'over-intercalated' tetrahedral phase ($I4_1/amd$), all lithium ions (2 per formula unit) occupy face-sharing LiO_6 octahedra (16*c* site) in contrast to cubic spinel with all lithium ions (1 per formula unit) occupying the LiO_4 tetrahedra (8*a* site):

$$\mathrm{Li}_1^{1+}\mathrm{Ni}_{0.5}^{2+}\mathrm{Mn}_{1.5}^{4+}\mathrm{O}_4^{2-}(Fd\bar{3}m) + \mathrm{Li}^+ + e^- \rightleftharpoons \mathrm{Li}_2^{1+}\mathrm{Ni}_{0.5}^{2+}\mathrm{Mn}_1^{3+}\mathrm{Mn}_{0.5}^{4+}\mathrm{O}_4^{2-}(I4_1/amd) \quad (2.16)$$

This phase transformation is caused by the Jahn-Teller distortion due to the increased concentration of Mn^{3+}, and it also decreases the crystallographic symmetry from cubic structure (c/a = 1) to tetragonal structure (c/a = ~ 1.16).[57,58] In addition, the structural instability can also be attributed to the slow manganese dissolution from the cathode materials through a disproportionation reaction in organic electrolyte [30,59]:

$$2\mathrm{Mn}_{solid}^{3+} \rightleftharpoons \mathrm{Mn}_{solid}^{4+} + \mathrm{Mn}_{solution}^{2+} \quad (2.17)$$

3 Synthetic chemistry for electrode materials

3.1 Solid-State reaction

Solid-state reaction, which is also called dry media reaction between raw materials, has been widely used in many industries because of its simplicity, low cost and ease of scale-up. The properties of the final products are affected by the characteristics of the raw materials and intermediates. Traditional calcination relies on the process of thermal conduction and thermal convection from heat sources to materials, which requires a long annealing time for a complete reaction and a slow crystallization process. Moreover, ball-milling is needed to synthesize the desired particle morphology and the crystal size.[60,61] Therefore, the simplicity is a pronounced advantage of solid state process, but the long reaction time, the difficulty of controlling particle shape, crystal size and elemental homogeneity pose substantial and significant challenges for the fabrication of high quality and reproducible products.

3.1.1 Models in sintering process

The calcination process has several stages which are involved in the particle consolidation, the pore disappearance and the growth (or shrinkage) of grains. The diversifications in the process of sintering are related to the changes in (1) particle size and morphology and (2) pore type and size distribution. Before heating, the powders are composed of individual grains and contain a lot of porosity. During annealing, these grains are linked together to eliminate the amount of porosity, and the mass transfer from one part of the structure to another also occurs. As calcination progresses, the particles move together according to the following mechanism: surface diffusion (SD), volume diffusion (VD) from surface and/or grain boundary, evaporation-condensation (E-C), plastic flow (PF) from dislocations, etc.[62,63]

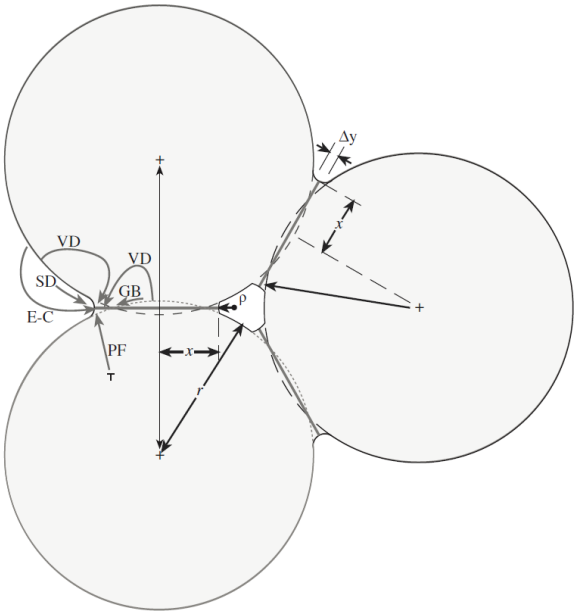

Figure 3.1 A model for sintering three spheres, showing the diffusion paths from the grain boundary to the neck surface and the development of a pore.[62]

3.1.2 Grain growth during calcination

The surface tensions should be balanced at every junction between grain boundaries when the grain is in thermodynamic equilibrium. Actually, there are always many grain boundaries with a net curvature in a polycrystalline agglomerate, resulting in a grain boundary migration and atomic reconstruction at high temperatures. The unbalanced forces makes the curved grain boundaries move toward to their center of curvature. The rate of boundary mobility is determined by the difference in free energy (ΔG) on its two sides and it can be expressed as follows [64]:

$$\Delta G = \frac{2\gamma V}{r} \tag{3.1}$$

where γ is the grain boundary surface tension, V is the molar volume and r is the radius of particles. It can be seen that the driving force is proportional to the grain boundary curvature and the rate at which the atoms can move through the boundary. What is more important, crystals with a large size normally possess a low grain boundary energy.

3.1.3 Lattice diffusion

The substances' movement from the grain boundary to the junction is determined by the lattice diffusion. The growth rate of the neck area between crystals can be derived by the following equation [62]:

$$\frac{x}{r} = (\frac{40\gamma a^3 r D^*}{kT})^{1/5} r^{-3/5} t^{1/5} \quad (3.2)$$

where x is the diffusion distance, r is the radius of particles, γ is the grain boundary curvature, a is the volume of the diffusing vacancy, D^* is the self-diffusion coefficient, k is Boltzmann's constant, T is the absolute temperature, t is the calcination time. Because of the lattice diffusion, the contact area is increased between particles. In addition, the crystal centers move toward each other. The rate of this approach is described as:

$$\frac{\Delta V}{V_0} = \frac{3\Delta L}{L_0} = 3(\frac{20\gamma a^3 r D^*}{\sqrt{2}kT})^{2/5} r^{-6/5} t^{2/5} \quad (3.3)$$

here, $\frac{\Delta V}{V_0}$ and $\frac{\Delta L}{L_0}$ are the volume change and length variation, respectively. It can be found that the crystal-growth rate increases exponentially with temperature, while it slowly increases with time. Compared to a long period of sintering time, a high temperature is more effective to obtain large and dense particles.

3.2 Microwave heating synthesis

3.2.1 Introduction to microwave sintering

Alternative synthetic routes have been developed to overcome the drawbacks of the conventional thermal treatment described above. Microwave heating is one of the most powerful methods for rapidly manufacturing the compounds,[65] as shown in Figure 3.2. Microwave annealing, which is known as dielectric heating, has the potential to heat the dielectric material instantly because of the volumetric heat generation at frequencies above 100 MHz. Typical commercial microwave ovens are operated at 2.45 GHz. During the microwave calcination, materials containing polar molecules try to align their electric dipole moment along the electromagnetic field. As the microwave is a form of electromagnetic wave with a quickly oscillating electric field component, the molecules rotate continuously by aligning to the field. Thus, thermal energy is produced inside the material by agitating their molecules or atoms in this process.[66]

3.2.2 Principles of microwave heating

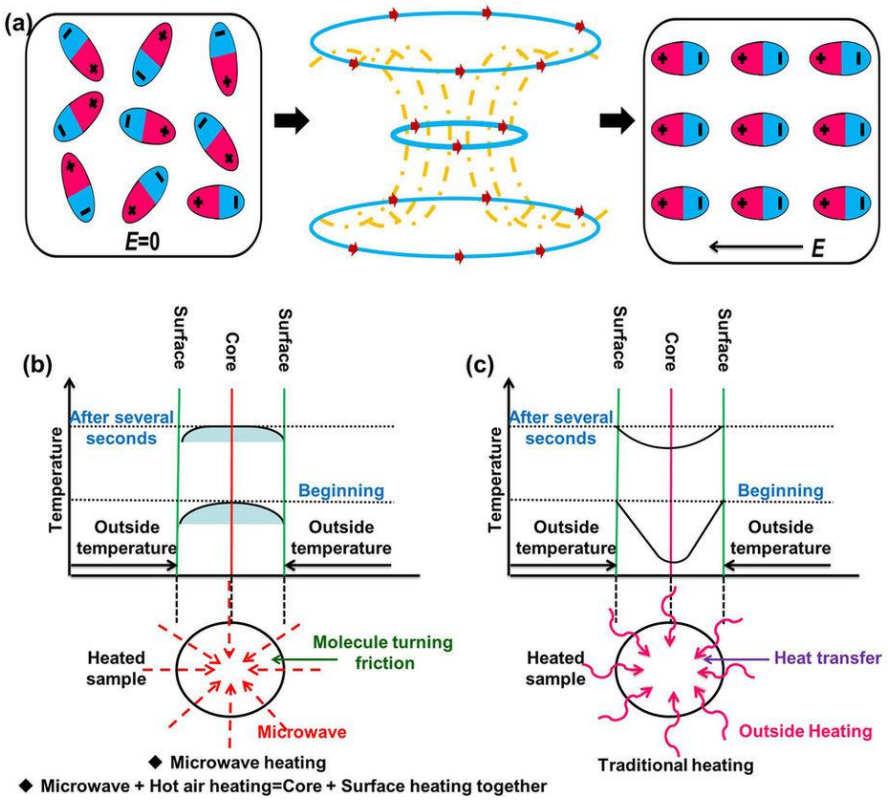

Figure 3.2 Comparison of the mechanism of (a-b)microwave heating and (c) traditional heating.[65]

The heat generation during microwave annealing has been modelled on the basis of Maxwell's equations [67]. The relationship between the power absorbed by substances and the electromagnetic field distribution is given by the following equation:

$$P_a = \sigma E_e^2 \tag{3.4}$$

where P_a is the absorbed power (W m^{-3}), σ is the conductivity and E_e is the electric field strength (V m^{-1}). The conductivity can be obtained according to the following expression:

$$\sigma = 2\pi\varepsilon_0 \, \varepsilon'' f \tag{3.5}$$

where f is the frequency of microwave radiation, ε_0 is the permittivity of free space and ε'' is the relative dielectric loss factor of the sample.

The penetration depth (d) is defined as a distance from surface to a point of the product where the intensity decays to e^{-1} (~ 37 %) of the original value. The uniformity of heating can be expressed as

$$d = \frac{\lambda}{2\pi\sqrt{\varepsilon'} \tan\delta} \tag{3.6}$$

where λ is wavelength, ε' is the relative dielectric constant and $\tan\delta$ is the energy loss tangent which is a ratio of ε'' and ε'.

Because of the specific interaction between molecules under exposure to microwave irradiation, temperature gradients in the substances are effectively alleviated so that temperature can be increased rapidly throughout the reaction medium. Furthermore, microwave furnace is simple to operate, and requires less maintenance and thermal budget.

3.3 Coprecipitation method

Chemical coprecipitation method is a simultaneous precipitation process of different soluble components with a precipitation agent by the formation of mixed crystals through adsorption, occlusion or mechanical entrapment. As shown in Figure 3.3, the first step is to obtain co-precipitates from the cation solution and anion solution in a homogeneous solution. The pH value, reaction temperature, feeding rate, agitation velocity and concentration are controlled strictly during the process of reaction and crystallization. The resulting powders are collected, washed and dried to remove impurities and water content. Thereafter, the lithium source is mixed with precursor to form the final cathode material at high temperature for several hours.

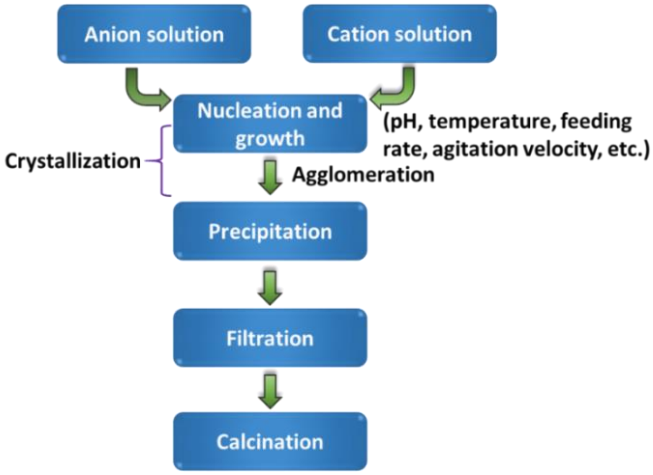

Figure 3.3 A schematic of a typical coprecipitation process for material synthesis.

Coprecipitation reaction can be realized by the kinetics of crystal growth and nucleation in a reactor. The commonly used anionic substances in coprecipitation reaction are hydroxides, carbonates and oxalates.[68–70] Hydroxide coprecipitation is the most popular route to synthesize the transition metal hydroxide precursors. A main advantage of this approach is that it results in

uniform and homogeneous precursors with good fluidity and high tap density. Furthermore, the hydroxide coprecipitation process using a continuous stirred-tank reactor (CSTR) is found to be a powerful, economic and scalable method for the production of layered hydroxides on a large scale (Figure 3.4). Owing to the fact that the hydroxide precipitation is one of the fastest chemical reactions, chelating agent like ammonia is usually employed for controlling the size, the morphology and the particle size distribution of the final products. So understanding of supersaturation, nucleation, crystal growth and post-growth (Ostwald ripening) is crucial to prepare the precursor for cathode materials.

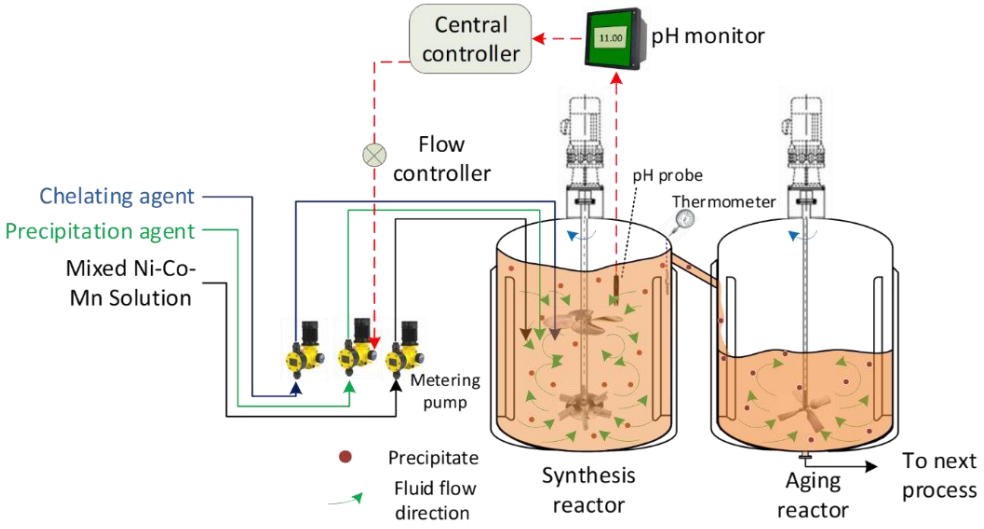

Figure 3.4 Schematic diagram of the co-precipitated particles synthesis via a continuous stirred-tank reactor (CSTR).[5]

Recently, Amine et al. prepared a nanostructured lithium-rich cathode material via a coprecipitation method and reported an improvement in the cycling performance and rate capability.[71] Very recently, our group also demonstrated the merits of the coprecipitation process, as shown in Figure 3.5.[72,73] We have utilized a fast hydroxide coprecipitation method to synthesize $LiNi_{1/3}Co_{1/3}Mn_{1/3}O_2$ cathode material and found the formation of a nanoflower structure in each step (Figure 3.5 (a-e)). Cathode materials made from the prepared $LiNi_{1/3}Co_{1/3}Mn_{1/3}O_2$ nanoflowers exhibits excellent electrochemical properties, demonstrating a specific discharge capacity of 126 mAh g^{-1} at a rate of 20 C between 2.7 and 4.3 V. A modified carbonate coprecipitation method combined with a vacuum distillation-crystallization process was also developed to prepare the $LiNi_{1/3}Co_{1/3}Mn_{1/3}O_2$ cathode material. We found that, compared to the conventional carbonate coprecipitation route, the modified method resulted in a better layered

structure with smaller particle size (Figure 3.5(f-g)). At different rates of 5, 10, and 20 C, the $LiNi_{1/3}Co_{1/3}Mn_{1/3}O_2$ material prepared by the modified route delivers a discharge capacity of 134, 123, and 112 mAh g^{-1} (labelled as LNCM-1 in Figure 3.5(i)), which is higher than that of the material obtained by a traditional carbonate co-precipitation method (labelled as LNCM-2 in Figure 3.5(i)). The cathode active material synthesized by the modified method also showed a good capacity retention of about 94 % after 100 cycles (Figure 3.5(h). Therefore, the chemical co-precipitation is a scalable, straightforward and low-cost approach to synthesize cathode materials, yet it is difficult to controllably prepare the desired architecture using coprecipitation methods.

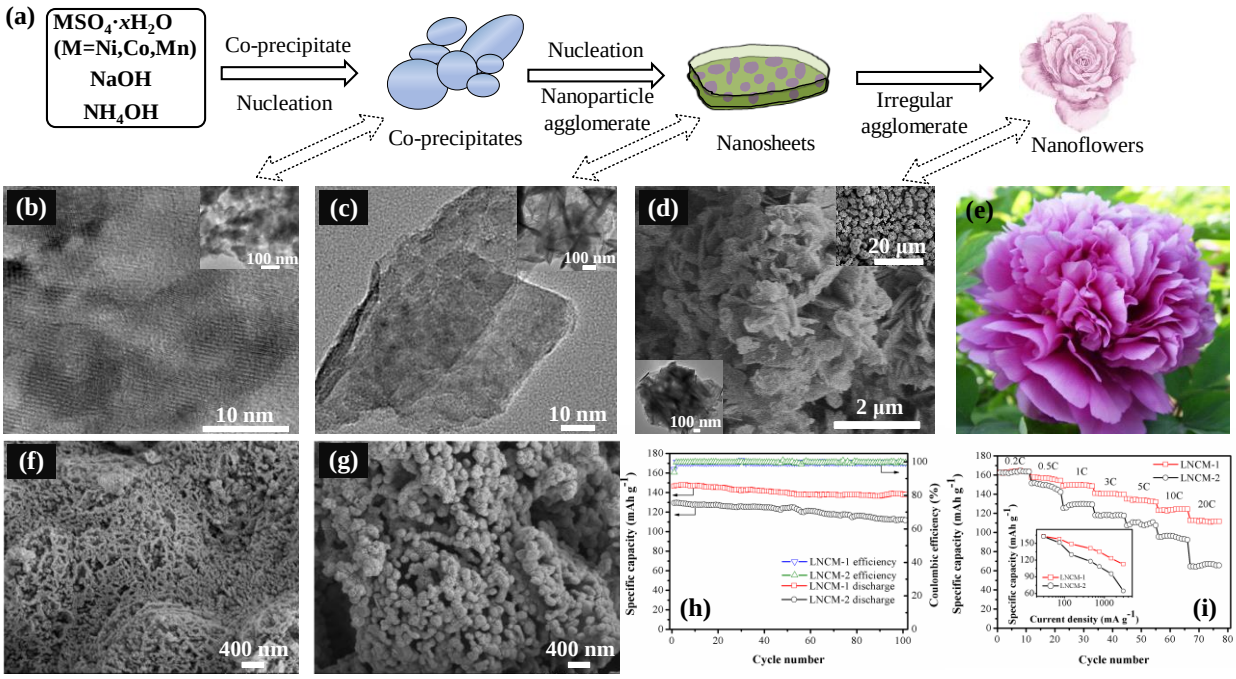

Figure 3.5 (a) Schematic illustration for the formation of the precursors at different stages during hydroxide co-precipitation reaction: (b) 0.5 h, (c) 1.5 h, and (d) 3 h;[72] *(e) photograph of a rose flower; SEM images of (f) precursor and (g) cathode material synthesized by a modified carbonate coprecipitation process; (h) cycling performance and (i) rate capability of the cathode materials made by the modified and traditional carbonate coprecipitation method.*[73]

4 Experimental

4.1 Materials Synthesis

4.1.1 Preparation of precursor

The precursor was synthesized by a hydroxide coprecipitation method. Firstly, a 2 M aqueous solution of stoichiometrically mixed $NiSO_4 \cdot 6H_2O$ and $MnSO_4 \cdot H_2O$ (molar ratio of Ni and Mn is 1:3) was added into a continuous stirred tank reactor (CSTR, see Figure 4.1) at the feeding rate of 2 ml min^{-1}. At the same time, 4 M precipitant solution (NaOH) and a desired amount of $NH_3 \cdot H_2O$ solution (complexing agent) were added into the reactor. The pH value (11.3 ± 0.3), temperature (52 ± 2 ^oC), and stirring speed (500 rpm) were carefully controlled, and the whole process was carried out under N_2 atmosphere. The co-precipitated particles were filtered, washed with distilled water for several times to remove the Na^+ and SO_4^{2-} ions and dried at 100 °C overnight.

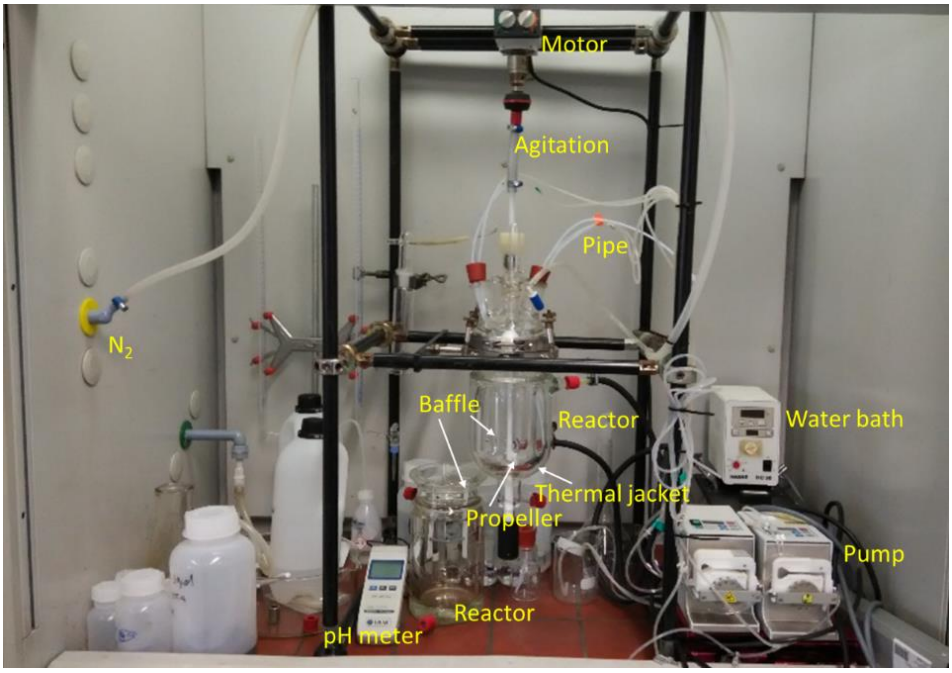

Figure 4.1 Experimental setup for the preparation of lithium transition-metal oxide cathode materials.

In addition, to investigate the structure of the Mn-rich precursor, the precursor for Ni-rich $LiNi_{0.6}Co_{0.2}Mn_{0.2}O_2$ was also prepared as a reference by the same procedure described above in

which the transitional metal solution was changed to a solution of stoichiometrically mixed $NiSO_4 \cdot 6H_2O$, $CoSO_4 \cdot 7H_2O$ and $MnSO_4 \cdot H_2O$.

4.1.2 Synthesis of lithium insertion compounds with different lithium contents

The obtained precursor powder for Mn-rich oxides was thoroughly mixed with different amounts of Li_2CO_3 (Li:TM=0.00, 0.08, 0.24, …, 1.52, TM = 0.2 Ni + 0.6 Mn) by a mechanical milling machine. Finally, the mixture was heated at 850 °C for 12 hours through a conventional furnace with air atmosphere to obtain the materials with various lithium concentrations, which are correspondingly labelled as L0.00, L0.08, L0.24, …, L1.52, respectively, as shown in Figure 4.2.

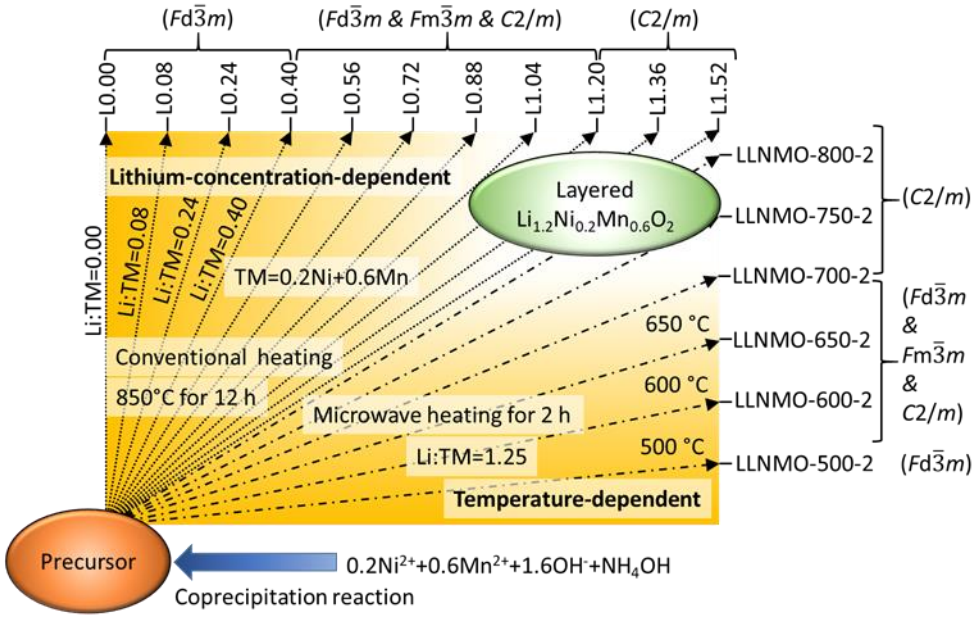

Figure 4.2 A schematic illustration for systematic synthesis of cobalt-free lithium insertion materials.

4.1.3 Synthesis of Li-excess layered oxides during microwave annealing

The prepared precursor for $Li_{1.2}Ni_{0.2}Mn_{0.6}O_2$ materials was thoroughly mixed with 7 % excess of Li_2CO_3. The obtained mixture was heated at different temperatures (500, 600, 650, 700, 750 and 800 °C) for 2 hours through a microwave chamber with air atmosphere to obtain the final materials, which are marked as LLNMO-500-2, LLNMO-600-2, LLNMO-650-2, LLNMO-700-2, LLNMO-750-2 and LLNMO-800-2, respectively.

For comparison, the layered $Li_{1.2}Ni_{0.2}Mn_{0.6}O_2$ (LLNMO-850-12-LT) cathode materials were prepared by annealing a mixture of obtained precursor and Li_2CO_3 at 850 °C for 12 hours in air via a traditional furnace.

4.2 Particle physical and thermal techniques

BET. The specific surface area of the samples was measured via Nitrogen physical adsorption isotherms (Gemini VII 2390, Micromeritics GmbH). The calculation of surface area was performed according to the Brunauer, Emmett and Teller (BET) theory.

TG/DSC. Thermogravimetric (TG) and differential scanning calorimetric (DSC) experiments were performed using a STA 449C thermal analyser (Netzsch) with a ramping rate of 10 K/min up to 1000 °C in air. Precursor and Li_2CO_3 were also measured separately to provide a reference.

4.3 Powder diffraction

***Ex situ* Powder diffraction.** The phase composition and crystal structure of the materials were measured by powder X-ray diffractometer (XRD, λ = 1.54056 Å) using a STOE diffractometer with Cu K$\boldsymbol{\alpha_1}$ radiation (40 kV, 40 mA) in the range 10-70°. *Ex situ* synchrotron radiation diffraction patterns were collected at the high-resolution Materials Science and Powder Diffraction (MSPD) beamline at ALBA, Spain, and/or at beamline P02.1, storage ring PETRA-III at DESY (Deutsches Elektronensynchrotron) at Hamburg, Germany.

***Ex situ* neutron powder diffraction.** The neutron powder diffraction (NPD) measurements were performed at the high-resolution powder diffractometer SPODI beamline, research neutron reactor MLZ/FRM II in Munich, Germany, at ambient temperature. The monochromatic neutrons were obtained at a 155° take-off angle using the 551 and 331 reflections of a vertically focusing Ge monochromator. The vertical position-sensitive multidetector consisting of 80 3He tubes with an effective height of 300 mm covering an angular two-theta range from 0° to 160° was used for data selection. All experiments were carried out in the Debye–Scherrer geometry with an incident neutron beam with a rectangular cross section at the sample position of 40 × 30 mm^2. The powder was filled into a cylindrically thin-wall vanadium container with diameter of 10 mm. The wavelength of the neutrons is approximately 1.54825 Å.

***In situ* synchrotron radiation diffraction.** *In situ* synchrotron radiation diffraction experiments were performed at the high-resolution MSPD at ALBA, using synchrotron radiation with an energy of 30 keV (λ = 0.41287 Å) and an exposure time of 60 s per pattern. The diffraction patterns at the MSPD beamline were collected using a MYTHEN 1D position sensitive detector.

Cells for *in situ* diffraction measurements were fabricated based on 2025 coin cell model and modified to allow penetration of the synchrotron light through a glass window, see Figure 4.3.

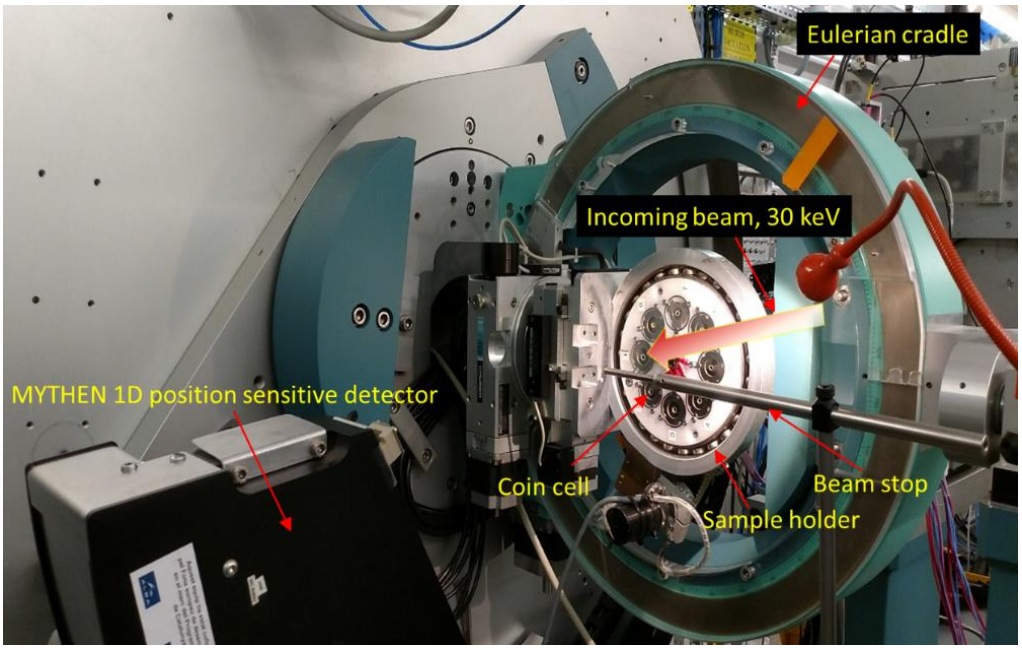

Figure 4.3 Custom-made sample holder for in situ SRD diffraction studies on lithium-ion batteries, during operation, at MSPD beamline.

***In situ* high-temperature synchrotron radiation diffraction.** The obtained precursor or spinel oxides were firstly mixed with a desired amount of Li_2CO_3. The mixture was sealed in a quartz capillary in air for time-resolved high temperature synchrotron radiation diffraction patterns at beamline P02.1, storage ring PETRA-III at DESY, using synchrotron radiation with an energy of 60 keV. The diffraction patterns at P02.1 beamline were acquired using a two-dimensional (2D) flat panel detector (Perkin-Elmer amorphous-Silicon detector) with a sample-to-detector distance of ~ 1600 mm. The resulting 2D images were then integrated to one dimensional diffraction patterns by using the X-ray image processing program Fit2D.

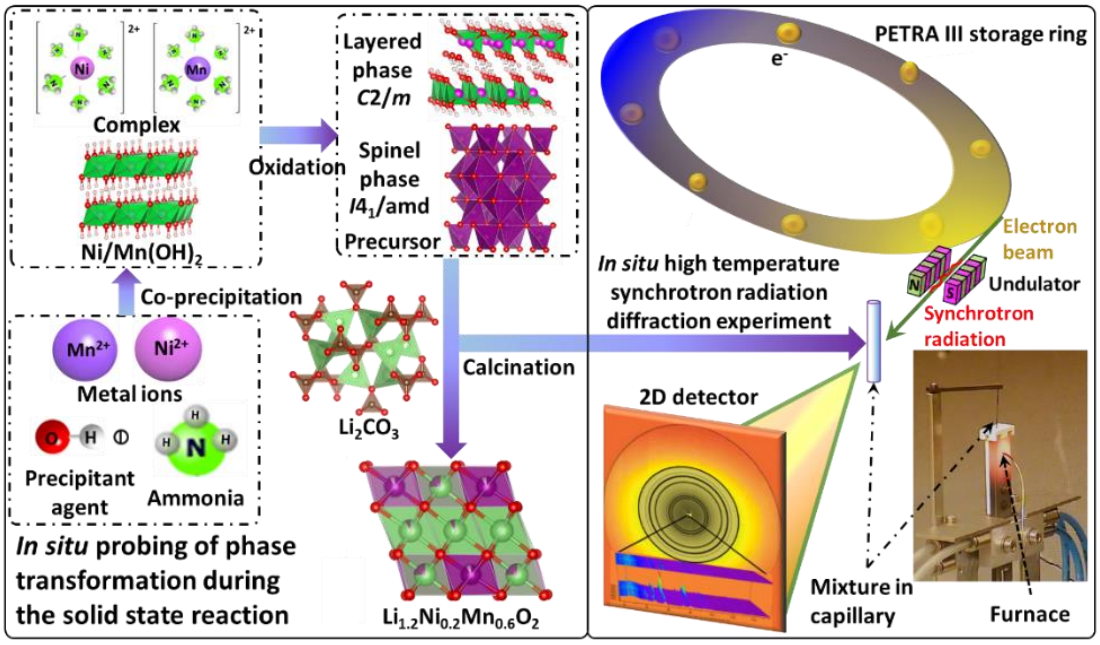

Figure 4.4 Schematic illustration for the experimental setup diagram of in situ high-temperature SRD measurements at beamline P02.1 at the storage ring PETRA-III at DESY.

Analysis of diffraction patterns. The lattice parameters and phase fractions were refined by the Rietveld method using the FULLPROF program. The bond valence sum (BVS) map was calculated by using the Bond_STR Program package incorporated in the FULLPROF program.[74]

Structure model. All the structural and electron density distribution models were obtained from refinement results and visualized using VESTA software.[75]

4.4 Microscopic observation

SEM-EDX. The morphology of the samples was observed by a scanning electron microscope (SEM, Zeiss Merlin) with an acceleration voltage of 10 keV. The coupled energy-dispersive X-ray (EDX) analysis was conducted at a Quantax 400 system from Bruker.

TEM-STEM-EDX. Transmission electron microscopy (TEM) and selected area electron diffraction (SAED) measurements were conducted on a JEM-2010. An aberration-corrected scanning transmission electron microscope (STEM, JEM-2010-ARM 200F) equipped with double probe aberration-correctors was employed to investigate the structure at the atomic scale. All of the microscopes were operated at 200 kV. The convergence semi-angle for STEM imaging was approximately 25 mrad, while the collection semi-angle was 12–24 mrad for annular bright-field

(ABF) imaging and 70–250 mrad for *Z*-contrast high angle annular dark-scanning transmission electron microscopy (HAADF) imaging. The STEM-EDX mapping results were obtained using a NSS software.

ED simulation. Electron diffraction (ED) pattern was simulated with a JEMS software developed by P. Stadelmann [76].

STEM simulation. Multislice HAADF-STEM image simulations were performed using Dr. Probe software [77,78] on the basis of atomic models relaxed by first-principles density functional theory (DFT) calculations and using experimental imaging parameters.

4.5 Spectroscopic techniques

Raman. Samples were placed in a chamber under the microscope interfaced to a confocal Raman microspectrometer LabRam (Horiba Scientific, Lille, France). A video image of the sample was utilised for accurate positioning of the laser spot on the material and at 523 nm excitation wavelength was chosen. The Raman spectra were analysed using the Labspec 6.0 software.

Chemical analysis. The concentration of chemical compounds Li, Ni, Mn was determined by inductively coupled plasma optical emission spectroscopy (ICP-OES, OPTIMA 4300 DV, PerkinElmer). The samples were dissolved in a mixture of hydrochloric and hydrofluoric acid at 235 °C for 3 h with the pressure digestion system DAB 2 (Berghof). Oxygen was determined by carrier gas hot extraction, which is known as insert gas fusion method (LECO TC 600).

XPS. X-ray photoelectron spectroscopy (XPS) investigations were carried out on a K-α XPS Spectrometer (ThermoFisher, East Grinsted, UK) using a micro-focused, monochromatic Al K-α spectrometer X-ray source. Data acquisition and processing was carried out using the Thermo Avantage software.

XAS. X-ray absorption spectroscopy (XAS) measurements were performed at XAS beamline of synchrotron radiation source at KIT and at the CLAESS beamline at ALBA synchrotron Light facility (Barcelona, Spain) [79]. The XAS data were recorded at the Mn K-edge (6539 eV), Ni K-edge (8333 eV) in transmission mode. Fourier transformed (FT) k^2-weighted $\chi(k)$-functions of the X-ray absorption near edge structure (XANES) spectra were obtained by subtracting the pre-edge background from the overall absorption and normalizing with a spline fit using the ATHENA software package. The k^2-weighted $\chi(k)$ data in k-space were Fourier transformed to real (R) space using a hanning windows (dK =1 Å^{-1}) to separate the extended X-Ray absorption fine structure

(EXAFS) contributions from various coordination shells. $\Delta \boldsymbol{k}$ = 3.1-11.4 $Å^{-1}$ and R_{bkg} = 1.15 Å were used for Ni K-edge while $\Delta \boldsymbol{k}$ = 2.6-11 $Å^{-1}$ and R_{bkg} = 1.3 Å were used for Mn K-edge.

NMR. Solid-state ^{7}Li magic-angle spinning (MAS) nuclear magnetic resonance (NMR) experiments were performed on a Bruker Avance 200 MHz spectrometer with a magnetic field of 4.7 T using a 1.3 mm MAS probe and a spinning speed of around 60 kHz together with a rotor-synchronized Hahn-echo pulse sequence. All shifts are referenced to an aqueous 1 M LiCl solution.

4.6 Battery performance evaluation

Construction of coin cells. The electrochemical performance of the prepared materials was investigated by galvanostatic cycling in a coin-type half-cell (CR2032) setup *vs.* lithium metal anode. The batteries were fabricated under argon atmosphere in an MBraun glove box where the H_2O and O_2 concentrations were held below 0.1 ppm. A mixture of active material, super P conductive agent and polyvinylidene fluoride (PVdF) binder at a weight ratio of 80:13:7 was coated on an aluminium foil to prepare the cathode. The mass loading of the active material in the electrode was 3–4 mg cm^{-2}. Celgard 2325 membrane and $LiPF_6$ in ethylene carbonate (EC): dimethyl carbonate (DMC) 1:1 (w/w) (LP30 from Merck) was used as separator and the electrolyte, respectively.

Galvanostatic tests. The half-cell measurements were conducted at various C-rates (1 C = 320 mA g^{-1}) between 2.0 and 4.8 V (*vs.* Li^+/Li) at 25 °C. All electrochemical measurements were controlled by a Bio-logic VMP3 potentiostat.

5 Results and discussion

5.1 Controllable preparation of precursor

Hydroxide coprecipitation method is one of the most commonly used techniques to prepare transition metal hydroxide precursors because this method results in uniform and homogeneous precursor powders with good fluidity and high tap density. Step-wise reactions were proposed for hydroxide coprecipitation in the presence of ammonia, i.e. the transition metal (TM, TM = Ni and Mn) ions in the solution tend to be connected to ammonia to produce initial complexes, and they were slowly released into the basic solution to form hydroxide precipitates [80]. These two-step chemical reactions are as follows:

$$\mathrm{TM}^{2+}(aq) + n\mathrm{NH_3}\cdot\mathrm{H_2O}(aq) \rightleftharpoons [\mathrm{TM}(\mathrm{NH_3})_n]^{2+}(aq) + n\mathrm{H_2O} \quad (n = 1, 2, 3, 4, 5, 6) \tag{5.1}$$

$$[\mathrm{TM}(\mathrm{NH_3})_n]^{2+} + 2\mathrm{OH}^- \rightleftharpoons \mathrm{TM}(\mathrm{OH})_2(s) + n\mathrm{NH_3} \tag{5.2}$$

The coprecipitation route was employed to prepare the nanoflower-structured precursor for Li-rich layered oxides (LLOs) (see Figure 5.1).

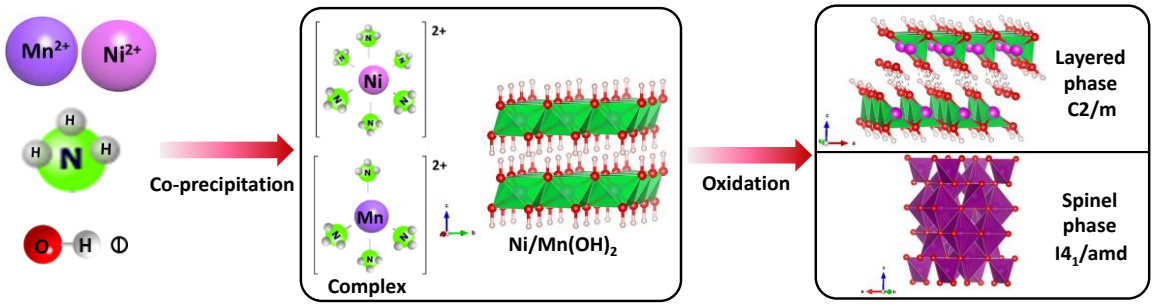

Figure 5.1 Schematic illustration for the production of precursor during the coprecipitation reaction.

5.1.1 The structure of precursor

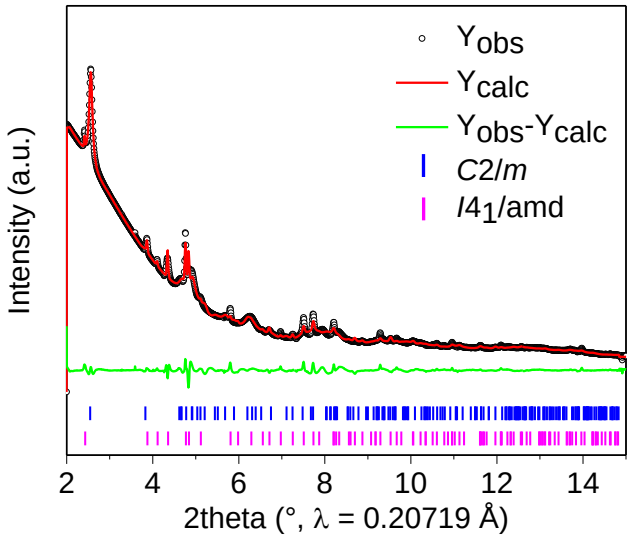

Figure 5.2 Rietveld refinement to SRD patterns of the precursor.

In order to get precise information on phase composition and the structure of the obtained precursor, synchrotron radiation diffraction (SRD) was measured at the powder diffraction beamline P02.1 at the storage ring PETRA-III at DESY (Hamburg, Germany). Figure 5.2 shows the SRD pattern of the precursor. The reflections of the SRD pattern can be indexed according to a tetragonal spinel phase with the space group symmetry of $I4_1/amd$ and a layered phase with the space group symmetry of $C2/m$. The results of Rietveld refinement (Figure 5.2 and Table 5.1) indicate that the weight fraction of layered and spinel structure in the precursor is approximately 74(4) wt.% and 26(2) wt.%, respectively.

Table 5.1 Lattice parameters and structural parameters of the LLO's precursor.

Layered phase ($C2/m$)					Spinel phase ($I4_1/amd$)					
a (Å)	b (Å)	c (Å)	beta	fraction (wt.%)	a (Å)	b (Å)	c (Å)	fraction (wt.%)	R_p (%)	R_{wp} (%)
5.1606	2.9128	9.3244	83.88	74(4)	5.7901	5.7901	9.2978	26(2)	14.7	18.6

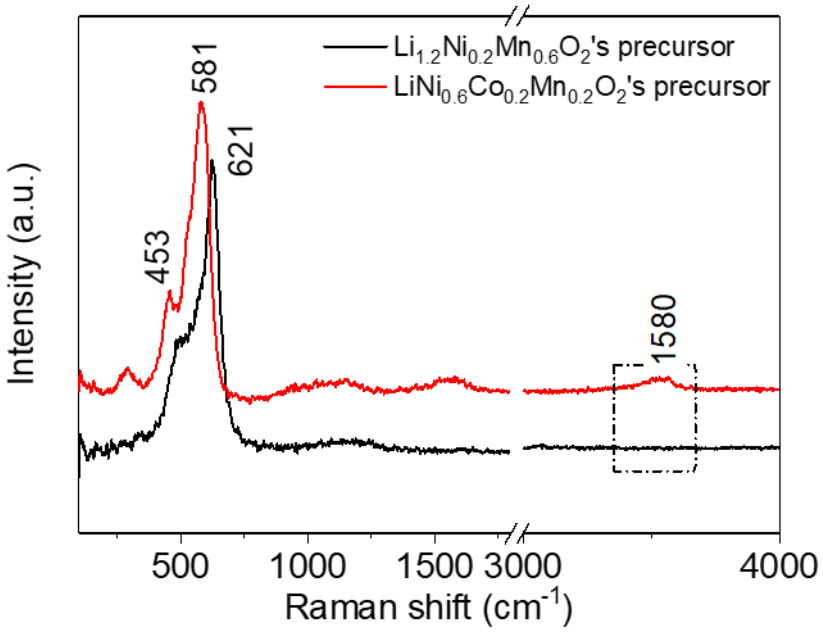

Figure 5.3 Raman spectra of two typical cathode material's precursors.

Figure 5.3 shows the Raman spectra of the precursors for Ni-rich $LiNi_{0.6}Co_{0.2}Mn_{0.2}O_2$ and Mn-rich $Li_{1.2}Ni_{0.2}Mn_{0.6}O_2$ materials. For the precursor of $LiNi_{0.6}Co_{0.2}Mn_{0.2}O_2$ material, the Raman feature observed at 453 cm^{-1} is characteristic for lattice vibrations of $Ni(OH)_2$ phase and the presence of 581 cm^{-1} Raman peak corresponds for the Ni-O vibrations of NiOOH phase.[81] In contrast, the Raman peak of LLO's precursor at about 621 cm^{-1} is ascribed to the Mn-O vibrational modes of MnOOH.[82] Raman spectra were also acquired at high wavenumbers (3000–4000 cm^{-1}) to detect the ν(O–H) modes of the $Ni(OH)_2$ phases. Note that the Raman stretching mode ν(O–H) at around 3580 cm^{-1} is only observed in the precursor of $LiNi_{0.6}Co_{0.2}Mn_{0.2}O_2$, which invalidates the possibility of trigonal hydroxide structures ($P3m1$) in the precursor of LLOs. Combined with the analysis of SRD and STEM data, the LLO's precursor powder is thought to be a composite of a dominating TMOOH ($C2/m$) phase and a minority tetrahedral phase ($I4_1/amd$). The reason is the oxidation of manganese hydroxide that could induce the strong Jahn-Teller characteristic of high-spin Mn^{3+} ($3d^4$), and the local site around the Mn^{3+} ions would be distorted to form monoclinic structure ($C2/m$) rather than the trigonal phase ($P3m1$).[83]

5.1.2 The morphology of precursor

Scanning electron microscopy (SEM) photographs (Figure 5.4) display the morphology of the precursor. The precursor particles are three-dimensional (3D) nanoflower-like agglomerates,

which are formed by thin nanosheets with a thickness of about 20 nm and lateral dimensions ranging from 500 nm to 2 µm. In addition, several irregularly formed particles are also observed.

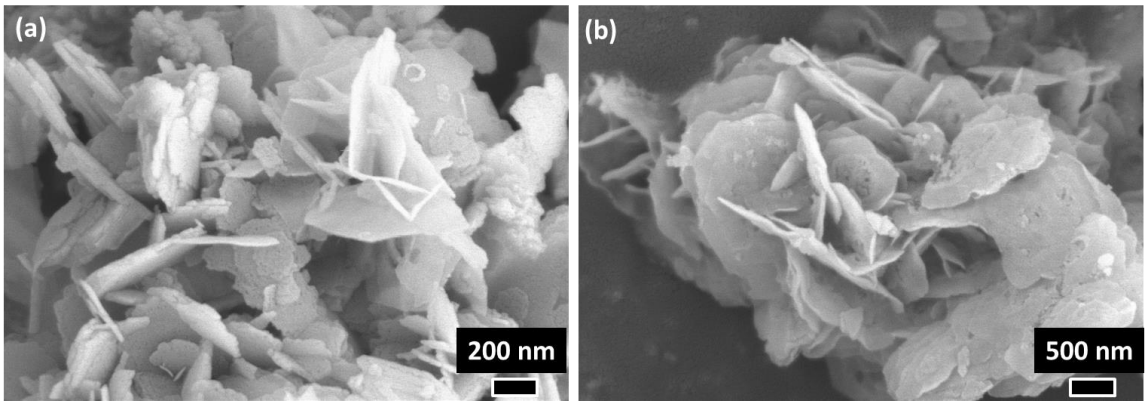

Figure 5.4 (a-b) SEM images of the prepared precursor for $Li_{1.2}Ni_{0.2}Mn_{0.6}O_2$ with different magnifications.

5.1.3 The microstructure and elemental distribution of precursor

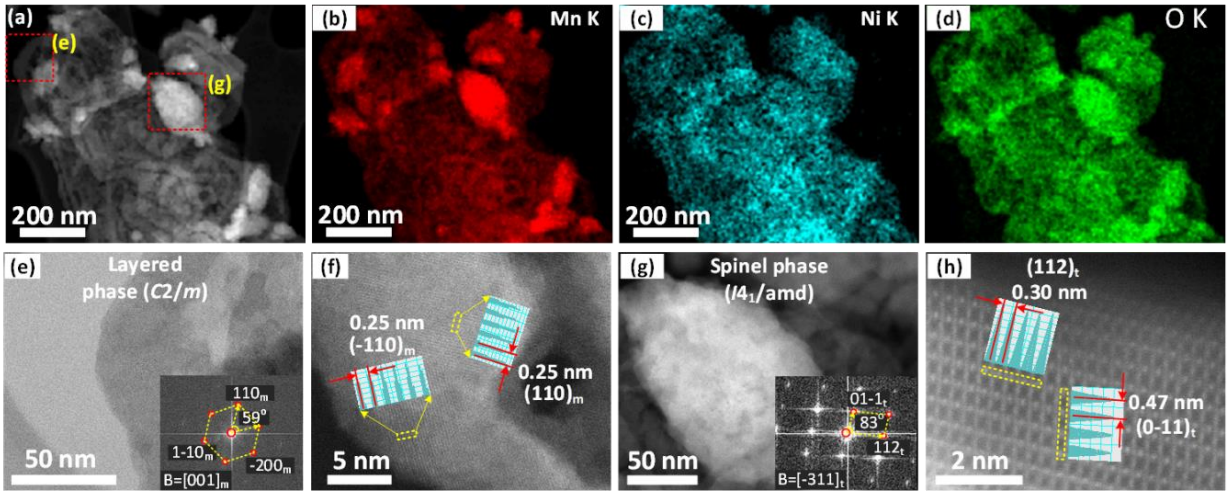

Figure 5.5 (a) HAADF-STEM image, STEM–EDX elemental distribution maps of (b) Mn, (c) Ni and (d) O for the precursor; (e-h) HAADF-STEM images of the nanosheets (selected area (e) in Figure (a)) and (g-h) HAADF-STEM images of the irregular particles (selected area (g) in Figure (a)). The insets in Figure (e) and (g) are the corresponding FFT patterns of STEM images.

An aberration-corrected high angle annular dark-field scanning transmission electron microscopy (HAADF-STEM) - energy dispersive X-ray (EDX) mapping technology was utilized to further probe the microstructure and the elemental distribution of the precursor. Interestingly, beside the 3D flower-like particles, irregularly shaped particles can also clearly be observed (Figure 5.5(a)). EDX maps (Figure 5.5(b-e)) show that Ni and Mn are distributed homogeneously within the nanosheets, while a higher amount of Mn seems to exist at the irregularly shaped

crystalline grains. High-resolution HAADF-STEM images (Figure 5.5(e-h)) were collected for the nanosheets and irregular agglomerates. As shown in Figure 5.5(f), for the nanosheets, two sets of lattice fringes with the same interplanar spacing of 0.25 nm are assigned to the $(\bar{1}10)_m$ (m means monoclinic phase) and $(110)_m$ planes of monoclinic structure, respectively. In contrast, another two sets of the interplanar distances of 0.47 and 0.30 nm are observed in irregular particles (Figure 5.5(h)), which correspond to the $(0\bar{1}1)_t$ (t means tetragonal phase) and $(112)_t$ planes of tetragonal spinel structure. The Raman results (Figure 5.3) and Fourier transform (FFT, Figure 5.5(e & g), inset) patterns also confirm that the precursor is composed of a layered (*C*2/*m*) phase and a spinel phase ($I4_1/amd$).

5.1.4 Oxidation state of transition metals

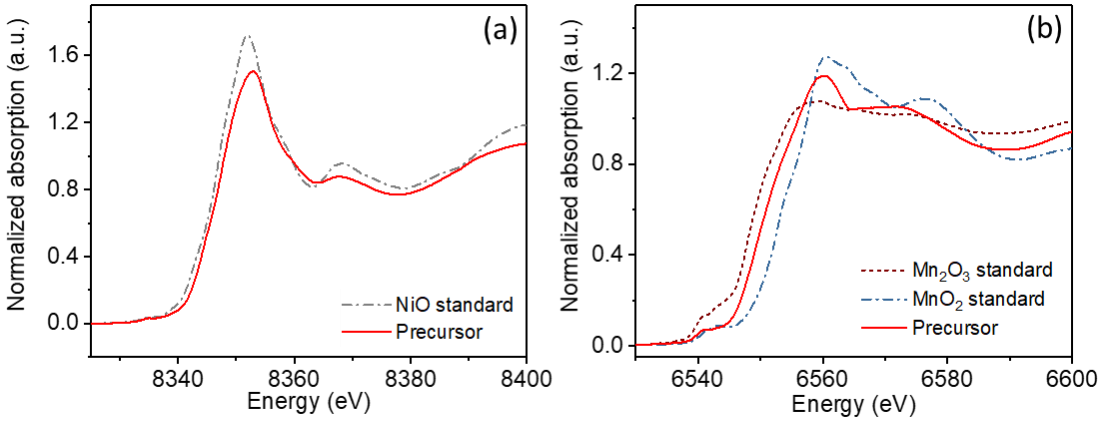

Figure 5.6 X-ray absorption spectra of the (a) Ni-K edge and (b) Mn-K edge for the precursor.

X-ray absorption spectroscopy (XAS) was performed to investigate the oxidation state of nickel and manganese in the precursor, see Figure 5.6. Compared to the standard of NiO (Ni^{2+}), Mn_2O_3 (Mn^{3+}) and MnO_2 (Mn^{4+}), the nickel and manganese valence states are determined to be +2 and +3/+4, respectively. These results indicate the oxidation of manganese compared with its pristine state before precipitation (+2), which could result in the formation of a minor tetragonal phase according to a series of possible transition reactions [71,84]:

$$\mathrm{Ni}^{2+}_{0.25}\mathrm{Mn}^{2+}_{0.75}(\mathrm{OH})_2 \xrightarrow{\text{air}} \mathrm{Ni}^{2+}_{0.25}\mathrm{Mn}^{2+}_{0.75-x}\mathrm{Mn}^{4+}_{x}(\mathrm{OH})_{2-2x}\mathrm{O}_{2x}$$
$$\xrightarrow{\text{air}} x\mathrm{Ni}^{2+}_{0.25}\mathrm{Mn}^{3.33+}_{0.75}\mathrm{OOH} + \frac{(1-x)}{3}(\mathrm{Ni}^{2+}_{0.25}\mathrm{Mn}^{2.88+}_{0.75})_3\mathrm{O}_4 \qquad (5.3)$$

5.2 Li-rich layered oxides formation mechanism from precursor

The regular route used to prepare the lithium insertion oxides involves two procedures: synthesis of the precursor and subsequent high-temperature solid-state reaction.[85,86] Therefore, both precursor and lithium source are critical for the formation of LLOs.

Based on the results of the LLO's precursor in section 5.1, it is found that the instability of manganese (II) hydroxide after air drying results in a mixed phase in the precursor, which makes it difficult to understand the high-temperature reaction mechanism of the precursor and lithium source. Hence, this section utilizes two sintering processes, i.e. (1) only precursor and (2) a mixture of the precursor together with lithium source (Li_2CO_3), respectively, designed to better elucidate the origin of lithium-insertion-induced oxygen uptake.

5.2.1 Thermal analysis

The thermogravimetric (TG) and differential scanning calorimetric (DSC) analysis curves of the (a) Li_2CO_3, (b) precursor and (c) their mixture are exhibited in Figure 5.7. It can be seen from Figure 5.7(a) that there appears a sharp weight loss and a distinct exothermic peak at around 742 °C for Li_2CO_3 due to the violent decomposition of carbonate ($Li_2CO_3 \rightarrow Li_2O+CO_2$). With respect to precursor, the TG curve presents three weight loss stages in air. The first weight loss of about 3 % below 200 °C is likely due to the removal of adsorbed water. The second weight loss (~ 6 %) between 200 to 400 °C can be attributed to the dehydration reaction of the TMOOH. The third weight loss and the endothermic peak at 685 °C is probably associated to the phase transformation of TMO_2/TM_2O_3 to TM_3O_4 resulting from the O loss (see Figure 5.8 and 5.9).[87] In TG profiles of the mixture of precursor and Li_2CO_3 (Figure 5.7(c)), the total weight loss is about 23% for the mixture, which agrees well with the theoretical value. It is worth to note that DTG curve show an obvious mass loss at 490 °C, which corresponds to decomposition of Li_2CO_3. The produced Li_2O would react with the attached powders and form Li-containing oxides. As will be shown in detail in section 5.2.3, *in situ* SRD results (Figure 5.10) show that the material obtained at 500 °C is a composition of spinel-like phase and residual Li_2CO_3. As a continuous lithiation reaction, the layered LLO materials are finally formed at approximately 850 °C. Further heat treatment at higher temperature (above 850 °C) would lead to the evolution of O_2 and Li (Figure 5.7(a & b)).[88] These results indicate that the calcination process plays a great role in the formation of the target materials.

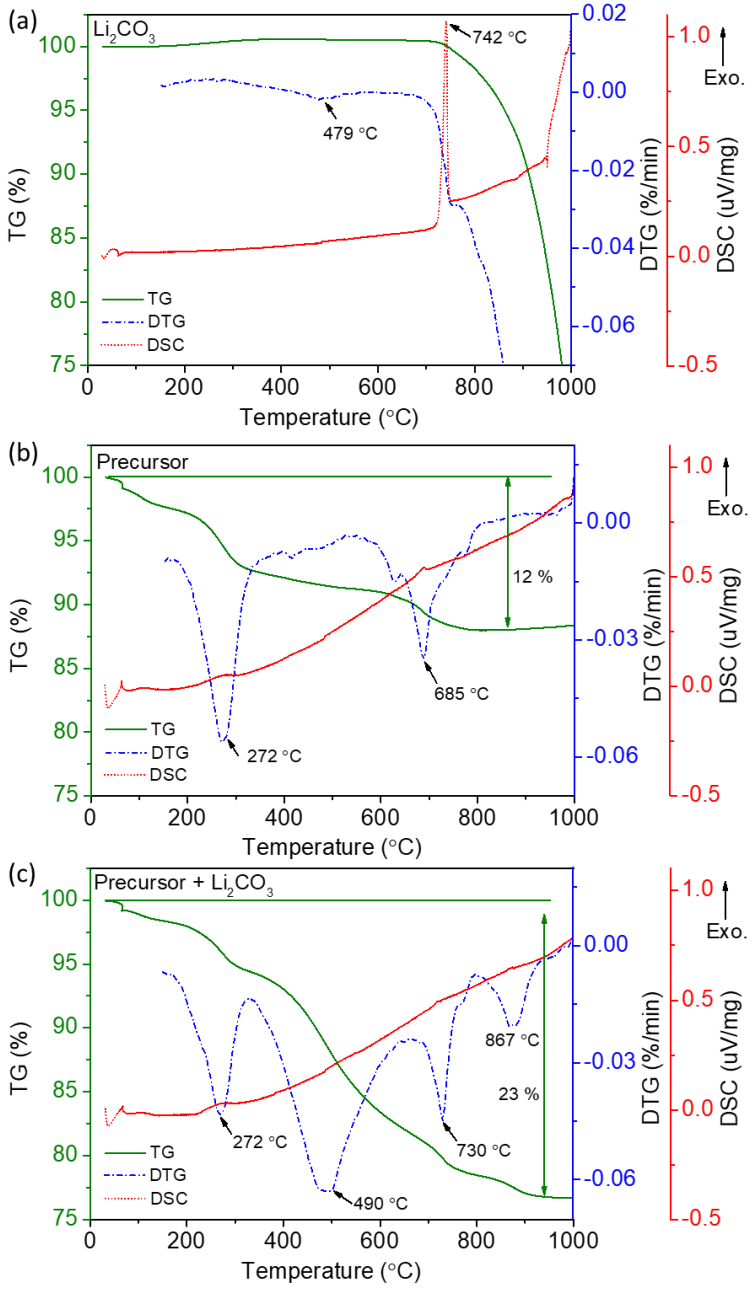

Figure 5.7 TG/DTG/DSC curves of the Li_2CO_3, precursor and their mixture.

5.2.2 Structural evolution of the precursor without lithium source during heating

In order to investigate the structural evolution of the LLO's precursor without lithium source during thermal treatment, *in situ* high-temperature SRD measurements were performed at P02.1 beamline, PETRA III (Hamburg). The heating ramp consisted of a heating to a specific temperature followed by a SRD measurement. The heating step was 50 °C up to the final temperature of 850 °C with exposure time of 60 s for each settled temperature.

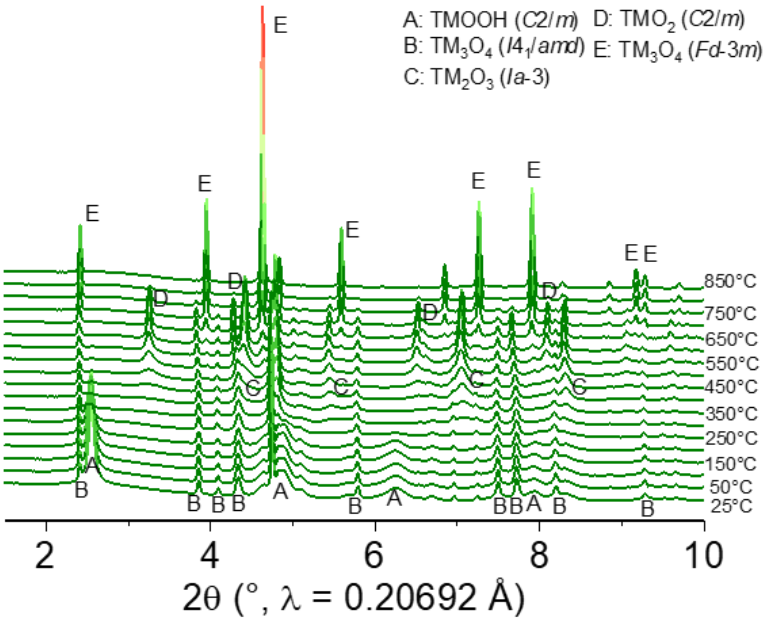

Figure 5.8 Time-resolved high-temperature SRD patterns of the LLO's precursor during heating.

With increasing temperature up to 200 °C, no significant changes in the SRD pattern are observed, indicating that the weight loss of the precursor at this stage observed in Figure 5.7 originates from the release of adsorbed water. When the temperature is higher than 300 °C, two new phases, i.e. a corundum-type TM_2O_3 (*Ia*-3) and an nsutite-type TMO_2 (*C*2/*m*), start to form and grow at the expense of TMOOH (*C*2/*m*), as shown in Figure 5.8. After increasing the temperature to higher than 750 °C, all the reflections can be indexed according to a single cubic spinel phase with the space group of $Fd\bar{3}m$, pointing out that all the tetragonal TM_3O_4 ($I4_1/amd$), cubic TM_2O_3 (*Ia*-3) and monoclinic TMO_2 (*C*2/*m*) become a solid solution phase (TM_3O_4) as a consequence of oxygen loss. All these results are consistent with the TG and DSC analysis.

The SRD pattern of the precursor heated to 850 °C was selected to learn more about the structure of the formed cubic spinel TM_3O_4 phase using Rietveld refinement method (Figure 5.9). The refinement was performed by using a single cubic spinel Mn_3O_4 structure model where manganese is located on both 8*a* and 16*d* sites, and oxygen is positioned on 32*e* sites. The good fit proves the proposed cubic spinel model to be reasonable. The refinement yields lattice parameters of $a = b = c = 8.2621(2)$ Å, and $V = 563.98(2)$ Å^3, respectively. These results demonstrate that the layered structure cannot be formed at the surface and in the inner part of the crystallites when only the precursor is heated at high temperature (> 550 °C), see the formation of the heterostructured

LLNMO-650-2 in section 5.3.4 and the layered LLNMO-750-2 in section 5.3.5. Therefore, lithium source was used to react with the precursor for preparation of LLOs in the following part 5.2.3.

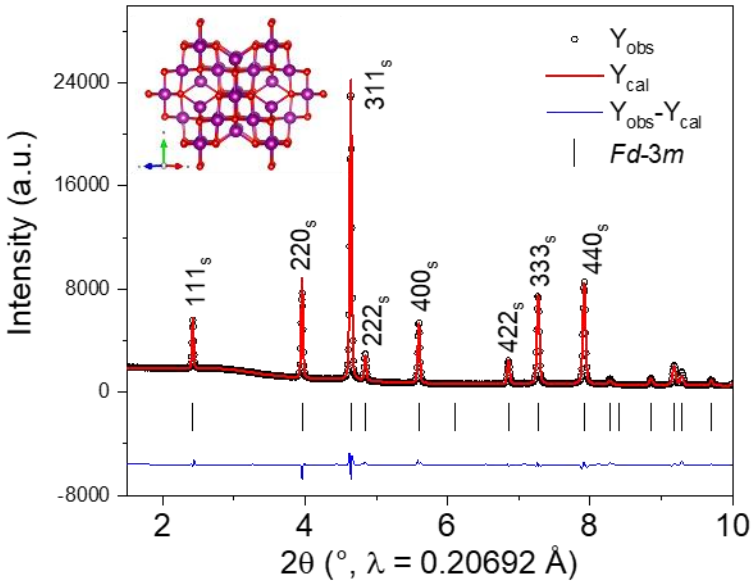

Figure 5.9 Rietveld refinement to SRD patterns of the precursor obtained at 850 °C and the resulting structure.

5.2.3 Structural evolution of the precursor with lithium source during heating

To explore the Li/O insertion during synthesis of LLOs, *in situ* high-temperature SRD technique was used to investigate the structural evolution of a mixture of lithium resource (i.e. Li_2CO_3) and the precursor. The *in situ* SRD patterns of the mixture during heating are shown in Figure 5.10 and Figure 5.11. Each diffraction pattern was analysed using Rietveld refinement (data not shown), and the selected refinement results were listed in Table 5.2.

As increasing the calcination temperature, the layered phase with the space group symmetry of *C*2/*m* in the precursor transforms to the cubic spinel phase (space group $Fd\bar{3}m$) because of the dehydration reaction. It is worth noting that the lithiation during thermal treatment accelerates the phase transition of the precursor and promotes the disintegration of Li_2CO_3 (melting point: 723 °C), which agrees well with the TG and DSC analysis in Figure 5.7. When the temperature is higher than 550 °C, both tetragonal spinel ($I4_1/amd$) and cubic spinel ($Fd\bar{3}m$) phases gradually convert to Li-containing rock-salt-type phase ($Fm\bar{3}m$) and Li-containing layered phases (*C*2/*m* and *P*3*m*1). Whether a compound contains Li or not will be displayed in the analysis of ^{7}Li MAS NMR results (Figure 5.15), section 5.3.1. The over-lithiated layered 1T-Li_2TMO_2 phase (*P*3*m*1) and the spinel phases (cubic and tetragonal phase) change into a Li-containing rock-salt-type phase ($Fm\bar{3}m$) and

a monoclinic layered phase (*C*2/*m*) at approximately 740 °C. Bearing in mind that all the lithium ions are located on the tetrahedral positions in the CdI_2-type structure of over-lithiated 1T-Li_2TMO_2 phase, this reveals a progressive phase transformation and a rearrangement of cations during lithium and oxygen incorporation into the host spinel framework (see Figure 5.11). The generation of layered 1T-Li_2TMO_2 phase can be ascribed to the high lithium content at the surface of the particles, indicating the lithium penetration into the crystal core from its surface. Finally, the monoclinic layered LLOs are produced at the expense of the Li-containing rock-salt-type phase at higher temperature (> 840 °C) according to the following lithiation reaction (5.4):

$$\underbrace{0.2Ni^{2+} + 0.6Mn^{2+} + 1.6OH^{-} \xrightarrow{NH_3 \cdot H_2O} \xrightarrow{\text{air-drying}} TMOOH + TM_3O_4}_{\text{hydroxide coprecipitation reaction}} \text{(precursor)}$$

$$\underbrace{\text{Precursor} + 0.6Li_2CO_3 \xrightarrow{\Delta,\ \text{air}} Li_{1.2}Ni_{0.2}Mn_{0.6}O_2}_{\text{high-temperature lithiation reaction}} \qquad (5.4)$$

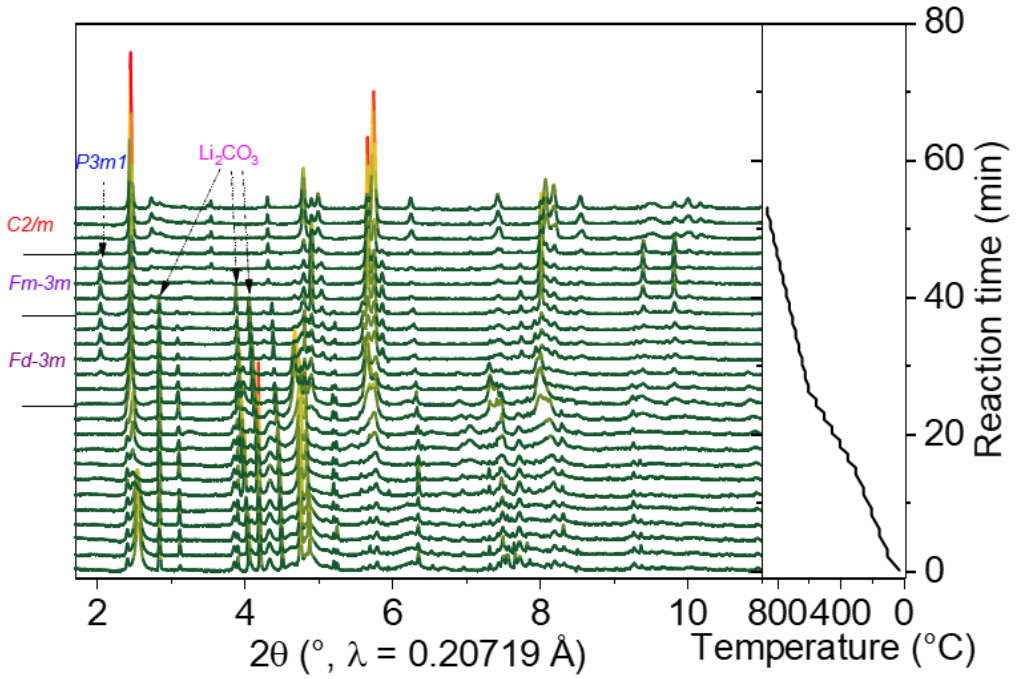

Figure 5.10 Time-resolved high-temperature SRD patterns of a mixture of LLO's precursor and Li_2CO_3, and the heating temperature as a function of reaction time.

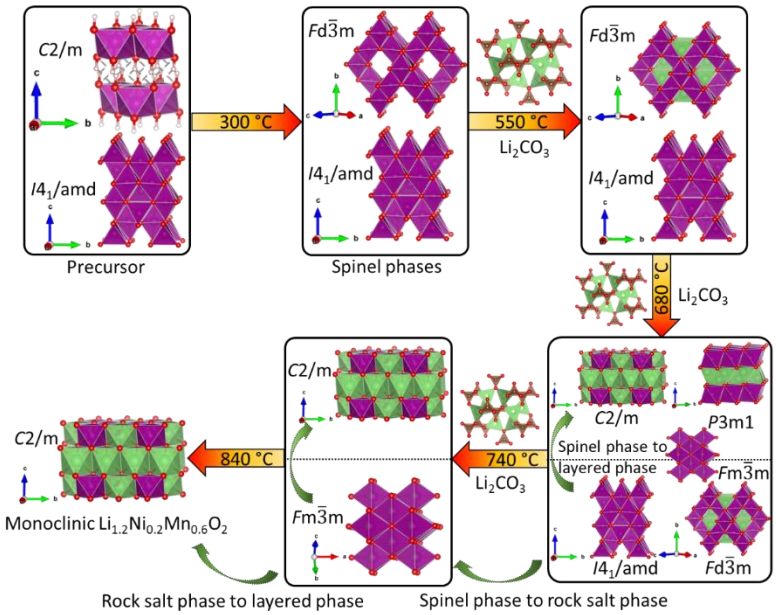

Figure 5.11 Schematic diagram for the phase transition of LLO's precursor and Li_2CO_3 during high-temperature lithiation reaction.

Table 5.2 Phase fractions of the mixture of LLO's precursor and Li_2CO_3 at different temperatures, as refined against the corresponding SRD patterns.

SRD pattern collected at different temperatures	Phase fraction (wt.%)							
	Li_2CO_3 (*C*2/*m*)	TMOOH (*C*2/*m*)	TM_3O_4 (*I*4$_1$/*amd*)	$Li_xTM_{1-x}TM_2O_4$ (*I*4$_1$/*amd*)	$Li_xTM_{1-x}TM_2O_4$ (*Fd*$\bar{3}$*m*)	Li_2TMO_3 (*C*2/*m*)	$Li_xTM_{1-x}O$ (*Fm*$\bar{3}$*m*)	Li_2TMO_2 (*P*3*m*1)
25 °C	43.22 (1.72)	43.38 (2.75)	13.41 (0.96)	/	/	/	/	/
300 °C	65.71 (4.16)	23.88 (3.68)	10.41 (0.69)	/	/	/	/	/
550 °C	46.56(2.57)	/	/	29.36 (1.86)	23.89 (1.64)	/	/	/
680 °C	24.89(1.89)	/	/	/	9.42 (4.70)	24.73 (1.72)	34.47 (3.49)	6.49 (1.29)
740 °C	/	/	/	3.67 (0.36)	0.46 (0.18)	25.01 (1.19)	56.44 (2.40)	8.36 (1.15)
820 °C	/	/	/	/	/	89.96 (2.51)	3.18 (0.72)	/
840 °C	/	/	/	/	/	90.02 (2.42)	/	/

Note: the impurity of Li_2SiO_3 in the sample obtained at 740 °C, 820°C and 840 °C was not accounted in this table.

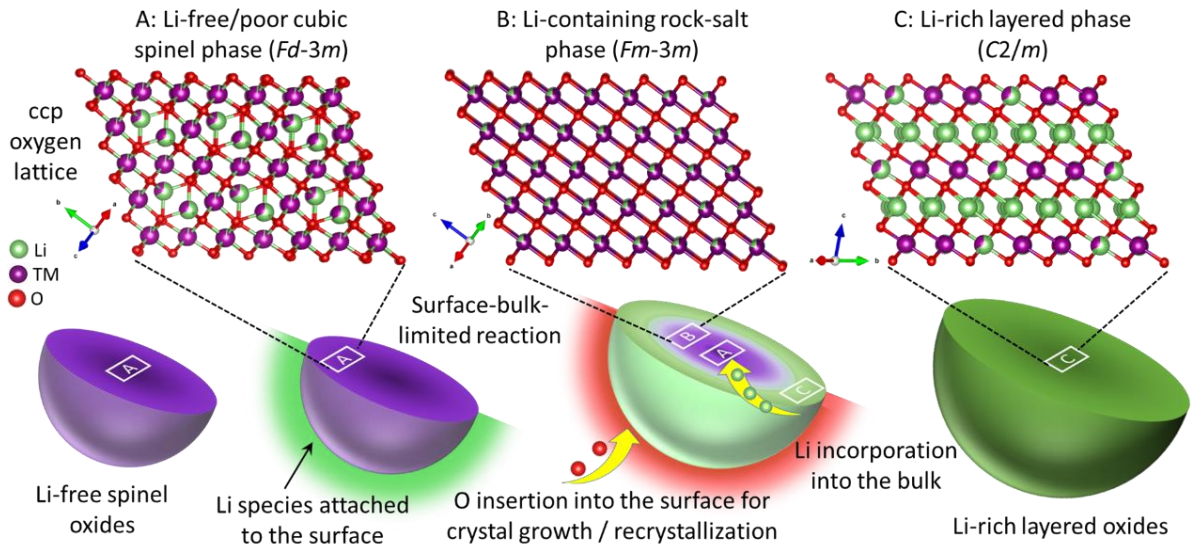

Figure 5.12 Schematic illustration of a possible formation mechanism of LLOs during calcination via lithium/oxygen incorporation into Li-free spinel crystallites derived from precursor.

The phase transition uncovered by *in situ* high-temperature SRD (Figure 5.10) reveals that the lithiation during the formation of LLOs is a surface-bulk-limited reaction. It is well known that the intermediate Li-free/containing spinel and Li-containing rock-salt-type phases have a cubic close-packed (ccp) oxygen lattice similar to that of the Li-rich layered phase.[89] During lithium incorporation into the spinel matrix, therefore, oxygen atoms are supposed to be only added to the oxygen surface lattice, thus providing the possibility of crystal growth and/or recrystallization. The oxygen uptake is crucial for crystal growth and phase transition from Li-free/poor spinel to Li-containing rock-salt-type phase respectively to Li-rich layered phase. This is due to the inserted surface oxygen that creates more metal coordination sites, not only for the Li ions incorporated into the surface structure, but also for the TM cations that are pushed/pulled to the crystal surface caused by Li intercalation into their previous positions in the interior structure.

5.3 Microwave-assisted synthesis of Li-excess layered oxides

Owing to the significance of the calcination process for the synthesis of LLOs, a very fast and efficient calcination process, i.e. microwave heating, was utilized. [90–92] On the basis of the *in situ* high-temperature SRD results, the temperatures for lithiation during microwave annealing were respectively chosen as 500, 600, 650, 700, 750 and 800 °C for two hours. The obtained sample was correspondingly labelled as LLNMO-500-2, LLNMO-600-2, LLNMO-650-2, LLNMO-700-2, LLNMO-750-2 and LLNMO-800-2, respectively.

5.3.1 Structural evolution during microwave annealing

The products obtained according to the different preparation conditions were investigated by X-ray powder diffraction (XRD) (Figure 5.13). In the XRD pattern of LLNMO-500-2, all the reflections can be indexed according to an unreacted Li_2CO_3 phase (space group, *C*2/*c*) and a cubic spinel phase ($Fd\bar{3}m$). As the annealing temperature is increased, the shift in position and the change of the full-width at half-maximum (FWHM) of the reflections are indicative for the change of the phase composition and the continuous crystal growth. With increasing reaction temperature, the intensities of reflections corresponding to spinel-like phase in the final product decreases gradually. The layered phase in the product starts to form at 600 °C and its concentration increases successively as temperature increases. Raman spectra were additionally recorded to further investigate the phase transformation (Figure 5.14). The main peak observed for all temperatures of synthesis, from 500 to 800 °C, shifts from 630 to 603 cm^{-1}, indicating the evolution A_{1g} vibration of Raman-active mode from spinel to layered phase.[93]

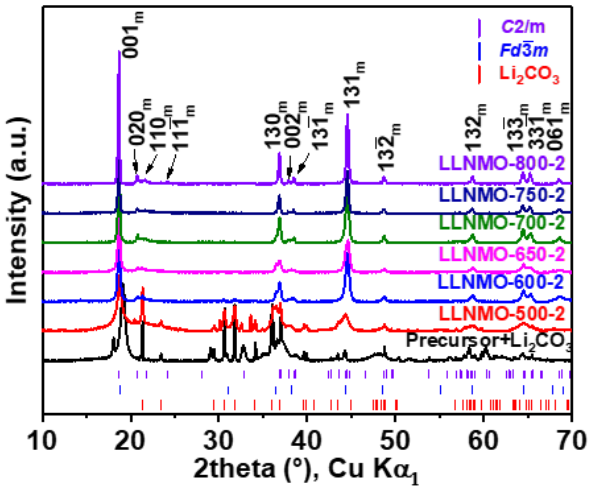

Figure 5.13 XRD patterns of the materials at each heating step.

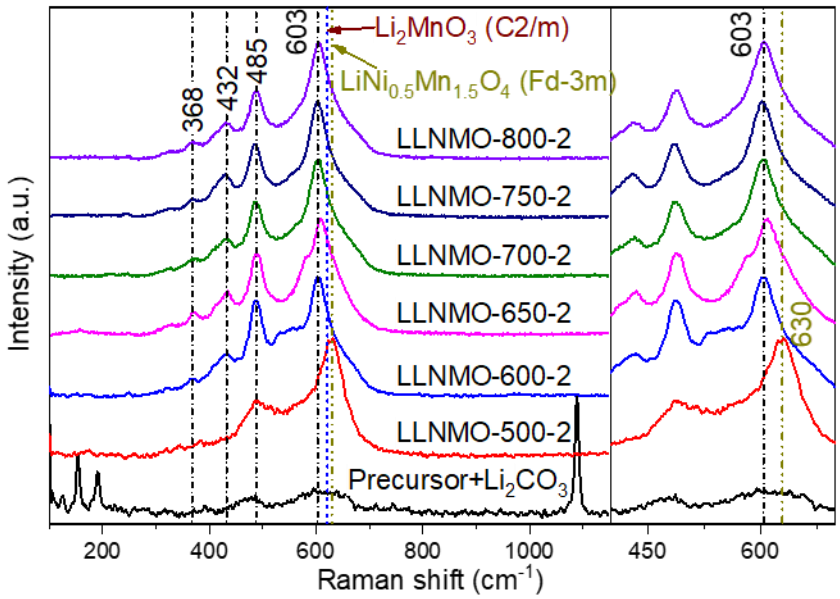

Figure 5.14 Raman spectra of the samples.

In contrast to XRD, which is insensitive to lithium, ^{7}Li magic-angle spinning (MAS) nuclear magnetic resonance (NMR) is a powerful tool to probe lithium in the lithium containing materials. Thus, high-resolution ^{7}Li MAS NMR spectroscopy was carried out to determine the changes in local lithium environment in a series of lithium containing compounds (Figure 5.15). The resonances at 1440 ppm and 1270 ppm can be attributed to Li coordinated by six TM atoms in the TM layer, respectively, and the resonances at 710 ppm and 550 pm can be assigned to lithium in the lithium layer.[94] The very large NMR shifts observed for these resonances are caused by paramagnetic TM atoms in the environment around the Li, i.e. transfer of electron spin density from the TM to Li via TM-O-Li bonds.[95] Therefore, these resonances can be clearly assigned to Li ions located in paramagnetic phases. As shown in Figure 5.15, these two groups of resonances appear in all samples revealing a gradual transformation of the oxide to the monoclinic phase during lithiation. As the temperature increases to 700 °C, the overall intensity of these peaks is rising, associated by the decline of the peak at ≈ 0 ppm. The latter peak is representing Li in a diamagnetic environment and thus shows an accelerated decomposition of Li_2CO_3. A weak resonance at around 940 ppm is observed for synthesis temperatures up to 750 °C, suggesting the production of the intermediate cubic spinel phase $LiNi_{0.5}Mn_{1.5}O_4$.[96]

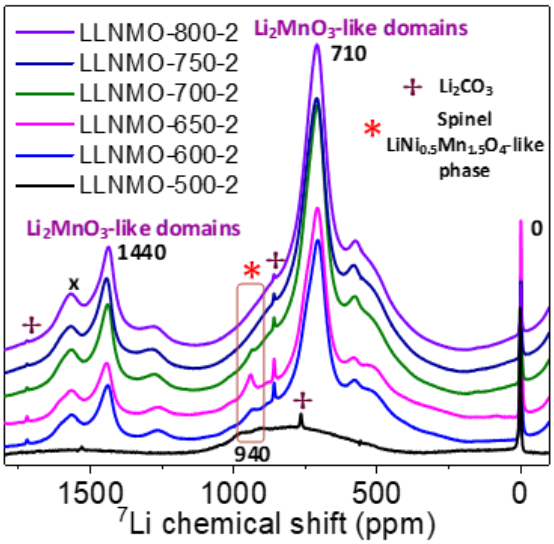

Figure 5.15 ^{7}Li MAS NMR spectra of the samples (spinning sidebands are marked with a plus and a cross).

5.3.2 Morphological evolution

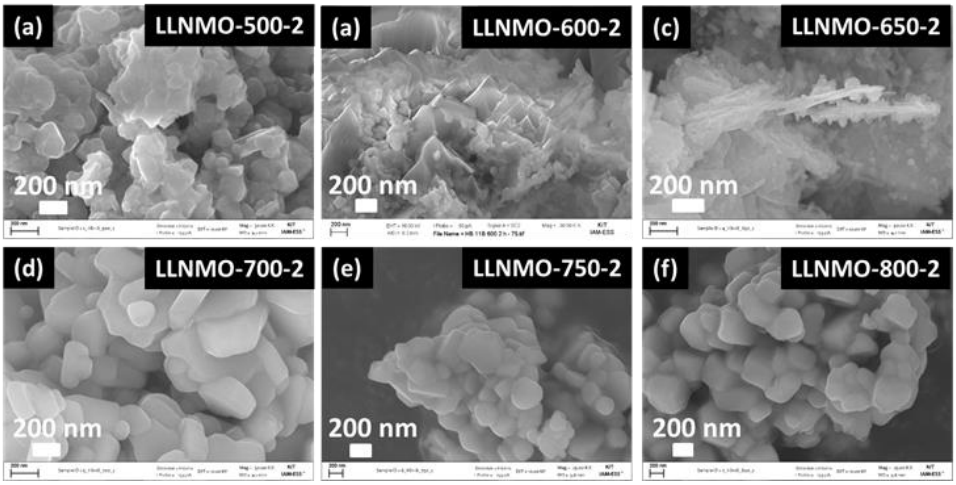

Figure 5.16 SEM images of the samples collected at different temperatures.

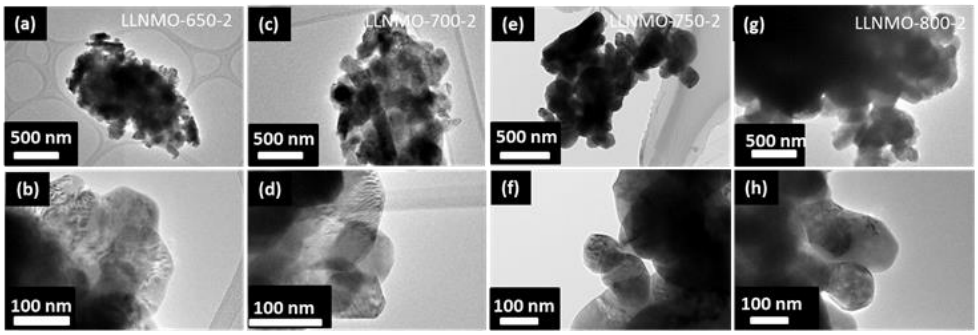

Figure 5.17 TEM images of the selected samples: (a-b) LLNMO-650-2, (c-d) LLNMO-700-2, (e-f) LLNMO-750-2, (g-h) LLNMO-800-2.

A morphological change of the particles/crystallites induced by the phase transformations occurring during the annealing process of the samples was detected by SEM and transmission electron microscopy (TEM) investigations (Figure 5.16 and Figure 5.17). When the reaction temperature is increased up to 600 °C, the original nanoflower-architecture of the precursor transforms into polyhedron-shaped particles, demonstrating the formation of spinel grains. At the same time, these particles tend to gradually agglomerate and grow in size according to the proposed mechanism in Figure 5.19. During this growth process, $(111)_s$ (s means spinel phase) facets of cubic spinel crystallites have the lowest surface energy so that the polyhedron-shaped particles are formed, [6,97] which are similar to the shape observed when the precursor alone is tempered at high temperature (Figure 5.48).

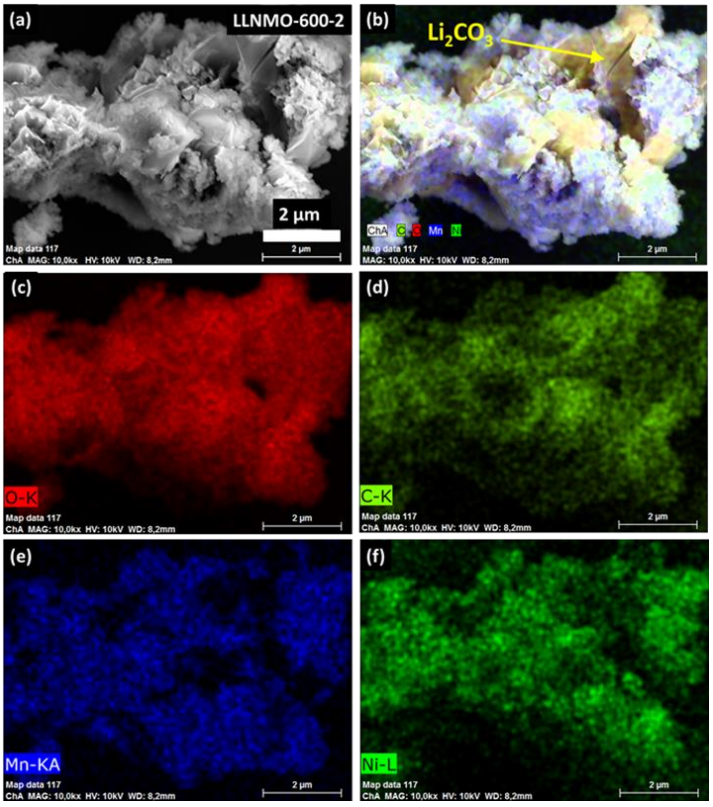

Figure 5.18 SEM-EDX maps of LLNMO-600-2.

As the heating temperature is increased to 650 °C, lithium oxide released from Li_2CO_3 constantly reacts with the attached polyhedral particles (Figure 5.18) to produce thin $(001)_m$ (m means layered monoclinic phase) dominated nanosheets, demonstrating the formation of crystal nuclei of layered phase and a significant surface reconstruction. The formed nanosheets can be attributed to a more stable $(001)_m$ facet of layered phase according to the Wulff theorem.[98,99] At

further increased process temperature, the thickness of nanosheets expands and the particles continue to grow through the well-known process of Ostwald ripening. The crystal growth throughout the whole process therefore can be considered as a "dissolution-nucleation-recrystallization" mechanism, i.e. in order to minimize the surface energy of the grains, small particles are consumed to form larger particles with simultaneous surface reconstruction.

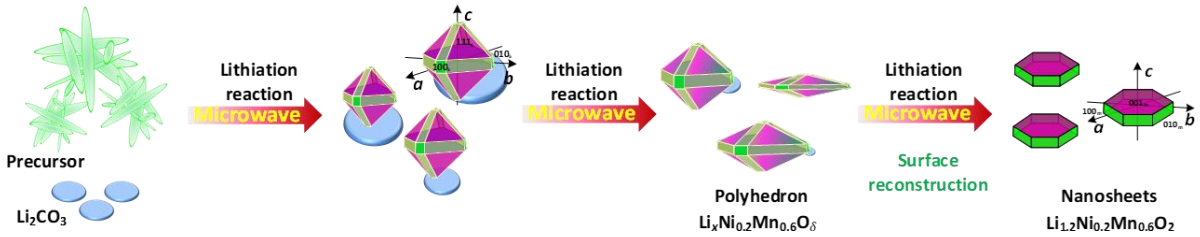

Figure 5.19 Schematic illustration of the formation of the Li-Mn-rich cathode and possible crystal growth mechanism during microwave heating.

Table 5.3 Results of chemical analysis and specific surface area of the samples.

Samples	Molar ratio					Specific surface area (m^2 g^{-1})
	C	Li	Ni	Mn	O	
LLNMO-500-2	0.13	1.23	0.2	0.56	2.67	/
LLNMO-650-2	0.09	1.29	0.2	0.56	2.11	5.81
LLNMO-700-2	0.04	1.29	0.2	0.56	2.00	4.83
LLNMO-750-2	0.02	1.30	0.2	0.57	2.00	3.57

Standard deviation: < 2 %.

The atomic ratio of Ni:Mn in the composition of these samples measured by ICP-OES is close to the theoretical value (1:3) (see Table 5.3). The content of carbon and oxygen in the samples decreases at a higher temperature while Li concentration among these specimens is approximately constant, which provides the evidence for the decomposition of Li_2CO_3 ($Li_2CO_3 \xrightarrow{\Delta} Li_2O+CO_2$) and the chemical incorporation of produced Li_2O into the attached particles under an air atmosphere during calcination.

5.3.3 Changes in oxidation state of transition metals

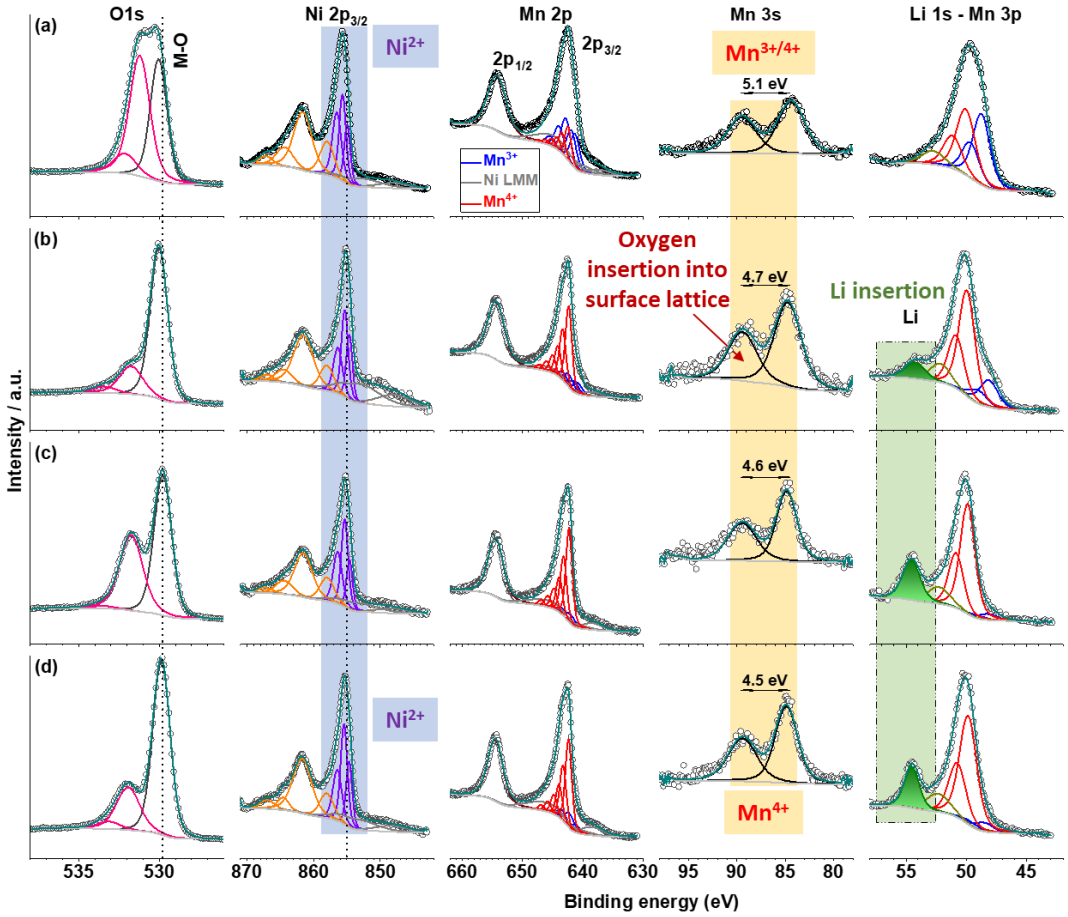

Figure 5.20 XP spectra of a) the precursor, *b) LLNMO-500-2, c) LLNMO-650-2, and d) LLNMO-750-2.*

In order to investigate the chemical state of the transition metals in the as-synthesized samples, XPS measurements were performed on the precursor, LLNMO-500-2, LLNMO-650-2 and LLNMO-750-2. The complete results can be found in Figure 5.20 and Table 5.4. The analysis shows that the oxidation state of the Ni ions for these three samples remains the same as in the precursor and all are assigned to the Ni^{2+} state. However, the Mn ions in the three samples are found to be mainly in the Mn^{4+} state. According to the splitting in the Mn 3s spectra and the multiplet fitting of the Mn 3p and Mn 2p spectra, around 5 %, 10 % and 20 % Mn^{3+} can be estimated for LLNMO-750-2, LLNMO-650-2, and LLNMO-500-2, respectively. Therefore, it can be concluded that the higher calcination temperature induces higher amounts of fully oxidized Mn^{4+} cations on the surface of the materials. Since higher lithium content is detected in the samples obtained at a higher temperature (NMR results in section 5.3.1), it is reasonable to assume that oxygen atoms are progressively inserted into the oxygen surface lattice of crystals to provide

necessary and sufficient conditions for crystal growth and recrystallization induced by phase transition during high-temperature lithiation.

Table 5.4 XPS quantification results of the samples.

Item	LLO's precursor	LLNMO-500-2	LLNMO-650-2	LLNMO-750-2
Atomic concentration normalized to Ni				
Li	0.0	4.8	6.2	4.8
Ni	1.0	1.0	1.0	1.0
Mn	1.2	2.8	1.7	1.5
O	1.7	6.2	4.7	4.6
C as Li_2CO_3	0.0	0.2	0.7	0.2
Binding energies (eV)				
Li		54.3	54.6	54.5
O in LNMO lattice		530.0	529.8	529.9
C as Li_2CO_3		290.1	290.0	290.2
Chemical state of transition metals				
Mn^{3+}/total Mn content	60 %	20 %	10 %	5 %
Ni		In Ni^{2+} state		

Standard deviation: < 10% of atomic concentration, except for Li which is higher than 10%. Binding energy uncertainty: ±0.2 eV.

Considering the difficulty of quantification of Li with XPS, after proper fitting of overlapping Mn 3p spectra, the peak found at 54.5 eV is assigned to Li as supported by the fact that this peak is absent in the spectrum of the precursor. The content of Li, normalized to Ni (after subtracting the Li_2CO_3 content), is listed in Table 5.4. These results illustrate that Li species are gradually released from Li_2CO_3 during heating, and then preferably enter into the surface of the attached powders forming a Li-rich surface region at a relatively lower temperature (e.g., LLNMO-650-2). These results are consistent with the intermediate over-lithiated layered Li_2TMO_2 phase in Figure

5.10, and the Li-containing layered phase on the surface of LLNMO-650-2 in Figure 5.25. According to the Mn/Ni ratio, an enrichment of Ni in the surface region can be suggested.

In order to understand the changes of the bulk oxidation states and local coordination of the samples, XAS studies were conducted at the CLAESS beamline, ALBA synchrotron radiation light source, Spain. The X-ray absorption near edge spectra (XANES) region of the XAS spectrum were analyzed for evaluating the electronic state of the Ni and Mn. Virtually no changes in the Ni K edge spectra were found among all the samples (Figure 5.21(a)), proving that nickel exists as Ni^{2+} for all applied temperatures of the synthesis process. Contrary, changes in the Mn K edge spectra of the samples can clearly be observed, as shown in Figure 5.21(c). A shift of the whole edge to higher energies with increasing temperature indicates an increased amount of Mn^{4+} at higher temperature. During the process of lithium penetration into the interior of the crystallites, the oxygen atoms inserted into the precursor are additionally inserted from air atmosphere to keep electric neutrality during lithiation. Li_2O as formally electronically neutral compound obtained by release of CO_2 during decomposition of Li_2CO_3 would not be capable to change the transition metals' oxidation states of the host material by its incorporation alone. By comparing the XANES region of Mn K edge of both LLNMO-650-2 and LLNMO-750-2 with the standard Mn_2O_3 and MnO_2, it can be concluded that the manganese in both samples is predominantly present as Mn^{4+} while the Mn in the precursor exists as Mn^{3+} and Mn^{4+}. Fourier transformation (FT R-space) of the spectra of Ni and Mn was performed to explain the changes in the local environment of the TM ions, see Figure 5.21(b) and (d). Two clear signals are visible in the FT R-space profiles for both Ni and Mn corresponding to TM-O interaction in the first coordination shell at around 1.5 Å and TM-TM paths (about 2.5 Å) in the second coordination shell. Regarding the EXAFS region of Mn K edge of the samples, the LLNMO-650-2 and the LLNMO-750-2 show a similar local structure around the Mn site, and both of them possess a more disordered structure around the Mn site compared to the LLNMO-500-2, indicating a compression in the second shell (Mn-TM) in the samples prepared at higher temperature. While the Mn-O distance of the high temperature samples ($\geq$ 500 °C) is not affected clearly by the temperature, which is compatible with a main Mn^{4+} character.[100] With respect to the FT R-space of the spectra of Ni, an average Ni-O and Ni-TM bond distance of the sample shrinks as increasing the temperature, revealing that the temperature treatment is acting continuously on the local structure, which is in agreement with the EXAFS results of Mn K edge of the samples. The most significant changes in asymmetry of the shape are

observed at the first shell of the Ni-O bonding during the preparation process, especially for LLNMO-650-2. These shifts might be attributed to the overlapping paths of the Ni-O bonding in the layered and spinel/rock-salt-type coherent structure,[101] see Figure 5.25(a). The LLNMO-750-2 shows the intensity of the Ni-O FT peak lower than the one of the Ni-TM FT peak, demonstrating a more ordered Ni-TM network and a disordered Ni-O network in the layered phase.

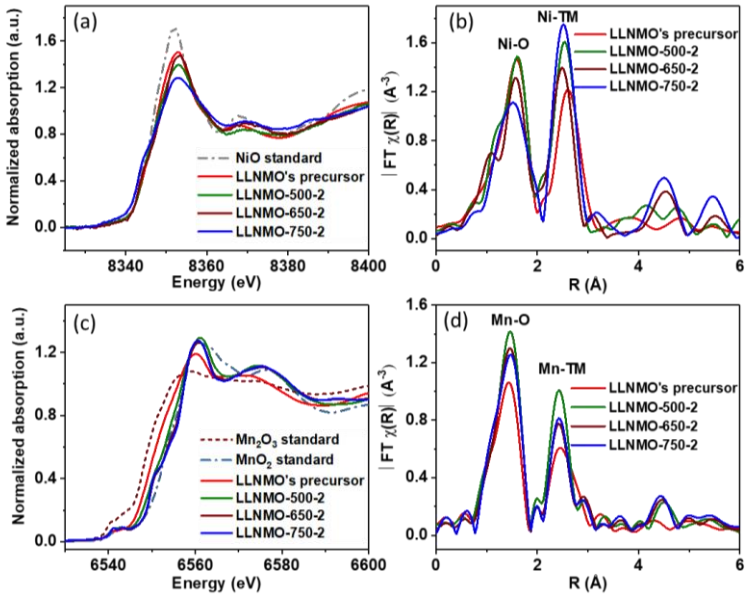

Figure 5.21 The normalized X-ray absorption near edge structure (XANES) spectra at the (a) Ni K edge and (c) Mn K edge of the same samples. Fourier transformed (FT) k^2-weighted $\chi(k)$ function of the extended X-ray absorption fine structure (EXAFS) spectra for the (b) Ni K edge and (d) Mn K edge.

5.3.4 Coherent layered and spinel/rock-salt-type phases on a single crystallite

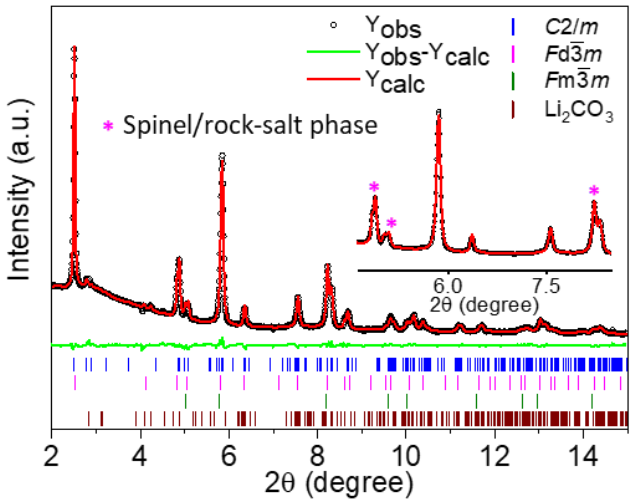

Figure 5.22 Rietveld refinement on SRD patterns (λ = 0.20717 Å) of LLNMO-650-2.

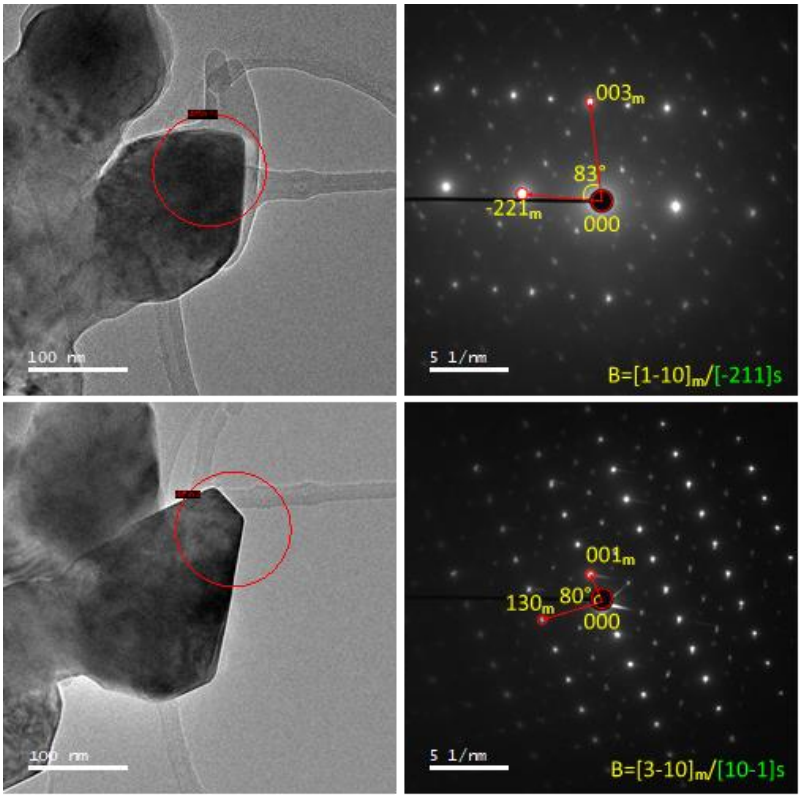

Figure 5.23 STEM images and SAED patterns of LLNMO-650-2 collected for different positions at one particle.

A spinel/rock-salt-type/layered heterostructured LLNMO-650-2 was selected to investigate the structural characteristics that are present at the intermediate state from the spinel-like phase to the layered phase. In order to get more information on phase composition and actual structure of this material, SRD experiments were performed. Rietveld refinement against the SRD pattern of LLNMO-650-2 was carried out using a multiple phase model, i.e. layered $Li_{oct}[Li_{0.2}Ni_{0.2}Mn_{0.6}]_{oct}O_2$, spinel $Li_{8a}[Ni_{0.5}Mn_{1.5}]_{16d}O_{4\ 32e}$, rock-salt-type $[Li_x\ TM_{1-x}]_{4a,oct}O_{4b}$, and unreacted Li_2CO_3 (*C*2/*c*), as shown in Figure 5.22. The good fitting suggests that the proposed structure model is reasonable. The weight fraction of unreacted Li_2CO_3, layered, spinel and rock-salt-type phases is 9(1) %, 80(1) %, 9(0.5) % and 2(1) %, respectively.

To study the heterogeneity of LLNMO-650-2, STEM images and SAED patterns were selected for two different areas at one crystallite (Figure 5.23). It can be seen that the layered and the cubic spinel/rock-salt-type structure are always coexisting coherently within a single particle, revealing that these structurally compatible phases with a common ccp oxygen lattice are coherently grown during the calcination process.

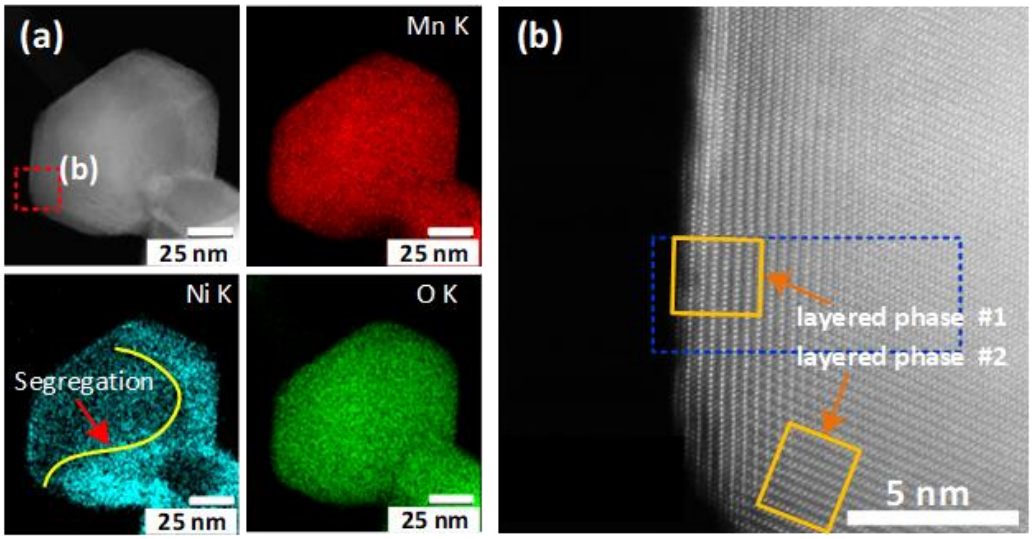

Figure 5.24 (a) HAADF-STEM-EDX mapping images of LLNMO-650-2; (b) HAADF-STEM image of LLNMO-650-2 for the area shown in (a).

Figure 5.24(a) shows the STEM-EDX maps of LLNMO-650-2. Although manganese and oxygen elements are homogeneously distributed in the selected particle, a strong nickel segregation on the surface is clearly observed, revealing that surface reconstruction during the process of phase transition leads to an extensive migration of nickel atoms. Figure 5.24(b) exhibits the HAADF-STEM image from the $[3\bar{1}0]_m/[101]_s$ projection. Full transformation from the cubic spinel/rock-salt-type structure to the monoclinic layered structure occurring during thermal treatment together with lithium source can most obviously be observed for surface near regions. Because the transition from cubic (spinel) to rhombohedral (layered) phase offers four degrees of freedom regarding the rhombohedral axis (stacking direction), layered phases with various crystallographic directions are commonly found as shown in the Figure 5.24(b).

Figure 5.25(a) shows a HAADF-STEM image that covers a region containing the surface and part of the inner crystallite. Insets in Figure 5.25(a) are the HAADF-STEM simulation images based on the monoclinic $Li[Li_{0.2}Ni_{0.2}Mn_{0.6}]O_2$ phase ($C2/m$) model from a $[3\bar{1}0]_m$ direction, rock-salt-type $Li_{0.28}Ni_{0.72}O$ (having a structure similar to that of $[Li_{1.2}Ni_{0.2}Mn_{0.6}]_{oct}O_2$) phase ($Fm\bar{3}m$) model from a $[10\bar{1}]_r$ projection, the spinel $LiNi_{0.5}Mn_{1.5}O_4$ ($[Li_{0.4}]_{tet}[Ni_{0.2}Mn_{0.6}]_{oct}O_{1.6}$) phase ($Fd\bar{3}m$) model from a $[10\bar{1}]_s$ projection, respectively. At surface-near regions, some extra scattering contrast is also detected, which can exclusively be attributed to the overlapped domains with pure Li-containing spinel, Li-containing rock-salt-type and Li-containing layered structure

because all the TM cations are located at the octahedral positions in these phases, see the simulation results in Figure 5.25(a). This probably represent an intermediate state from spinel/rock-salt-type phase to layered phase forming the lattice mismatch (see also the *in situ* high-temperature SRD results in Figure 5.10 in section 5.2.3).

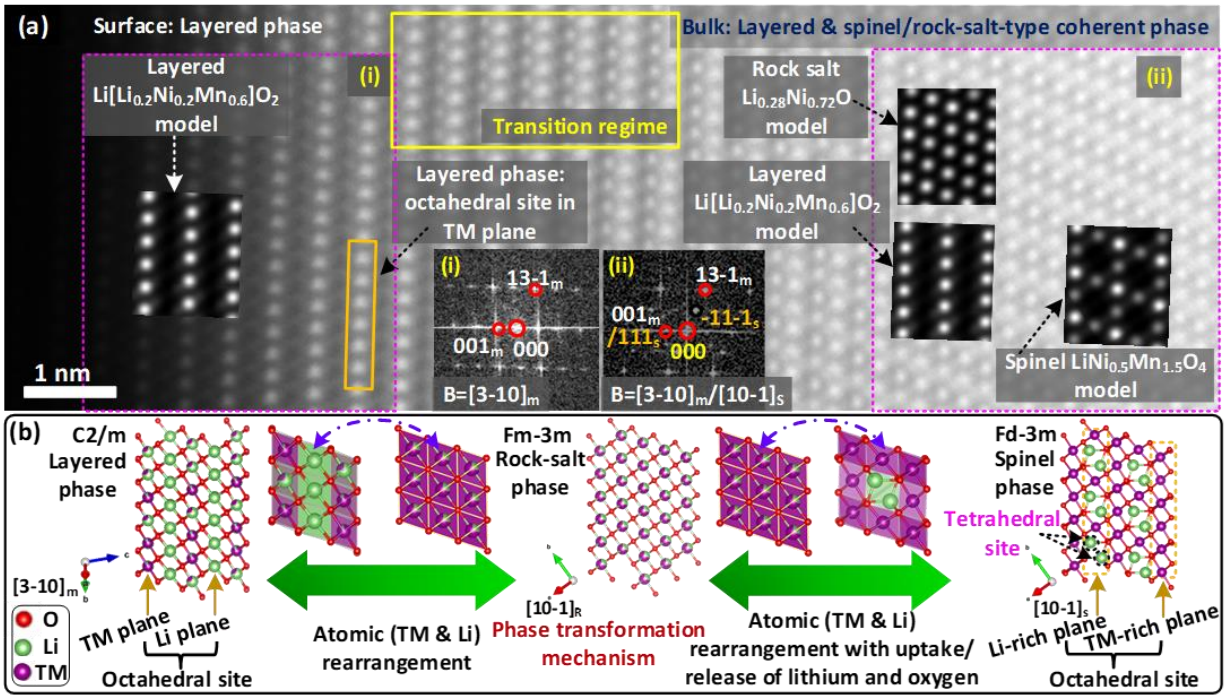

Figure 5.25 (a) Magnification of the blue rectangle region given in Figure 5.24, revealing the local nature of the structural transformation occurring; (b) schematic illustration of the possible atomic rearrangement mechanism from spinel/rock-salt-type to layered phase.

The pure layered structure is most clearly observed at the surface near region (i) in Figure 5.25(a), the region (ii) follows towards the interior part of the crystallite exhibiting a very different pattern of atom columns that cannot be interpreted by a single layered structure. Overall, the atomic column pattern in region (ii) can rationally described by a Li-containing rock-salt-type structure, see inserted $Li_{0.28}Ni_{0.72}O$ model. This Li-containing rock-salt-type structure can be considered as a non-isomorphic cubic supergroup when all the lithium and TM cations are completely disordered within all layers starting from a rhombohedral layered structure model ($R\bar{3}m$). However, because an additional contrast seems to be superimposed onto that of a pure Li-containing rock-salt-type phase, it cannot be excluded that Li-containing spinel structures and/or Li-containing layered structures with various orientations contribute to the contrast observed in region (ii). Thus, such rock-salt-type structure is supposed to be a kind of intermediate structure that exists between the

"Li-rich" layered structure at the surface and the "Li-poor" spinel phase that remains in the interior bulk part of the particle (see Figure 5.26).

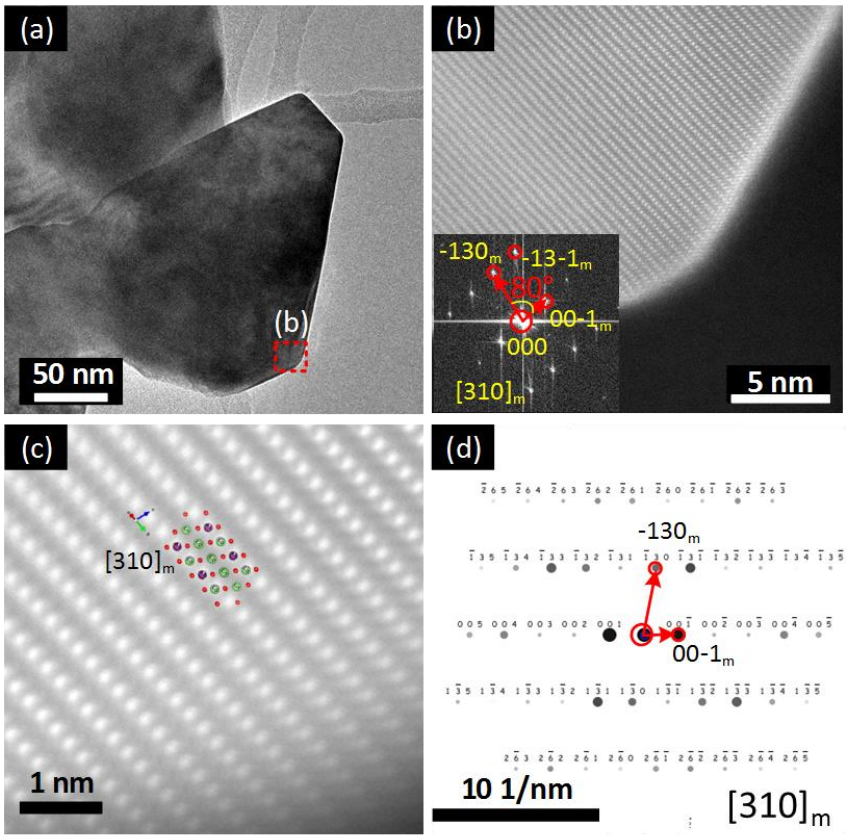

Figure 5.26 (a-c) HAADF-STEM images, (b, inset) the corresponding FFT patterns and (d) ED simulation patterns of LLNMO-650-2, indicating the formation of layered phase on the selected particle at this region.

Figure 5.26 presents the HAADF-STEM images taken from another area of the selected LLNMO-650-2 crystallite. As shown in Figure 5.26(b), the corresponding FFT patterns suggests a layered motif, which cannot be formed by a crystalline material with a cubic structure. The coherent structure on a single crystallite unambiguously supports a multiple-phase concurrent phase transition mechanism, which is also the origin of the single crystallite heterostructure. During thermal treatment, the spinel structure is initially generated from the precursor. Hence, lithium and oxygen tend to preferably enter the host spinel matrix via the $\{100\}_s$ facets that possess a relatively low atomic surface packing density. Subsequently, as part of the phase transition from spinel/rock-salt-type phase to layered phase, there is a collective atomic segregation of the TM ions from one metal layer to the other metal layer in exchange with lithium caused by incorporation of lithium and oxygen. That is, the equally distributed TM and Li cations in the spinel/rock-salt-

type structure are separated into a predominant Li layer and a predominant TM layer for the layered structure, see Figure 5.25(b). Therefore, the densely packed $(111)_s$ surface of the spinel progressively becomes the $(001)_m$ surface of the layered phase during the transition process, see Figure 5.12 and 5.19.

5.3.5 Optimized layered $Li[Li_{0.2}Ni_{0.2}Mn_{0.6}]O_2$ cathode material

After high-temperature lithiation during microwave calcination, LLO with high concentration of the layered phase is obtained. What is still not clear, however, is whether LLOs should be regarded as a composite of nano-domins of a layered rhombohedral structure ($R\bar{3}m$) and a layered monoclinic structure or rather as a monoclinic single-phase solid solution.

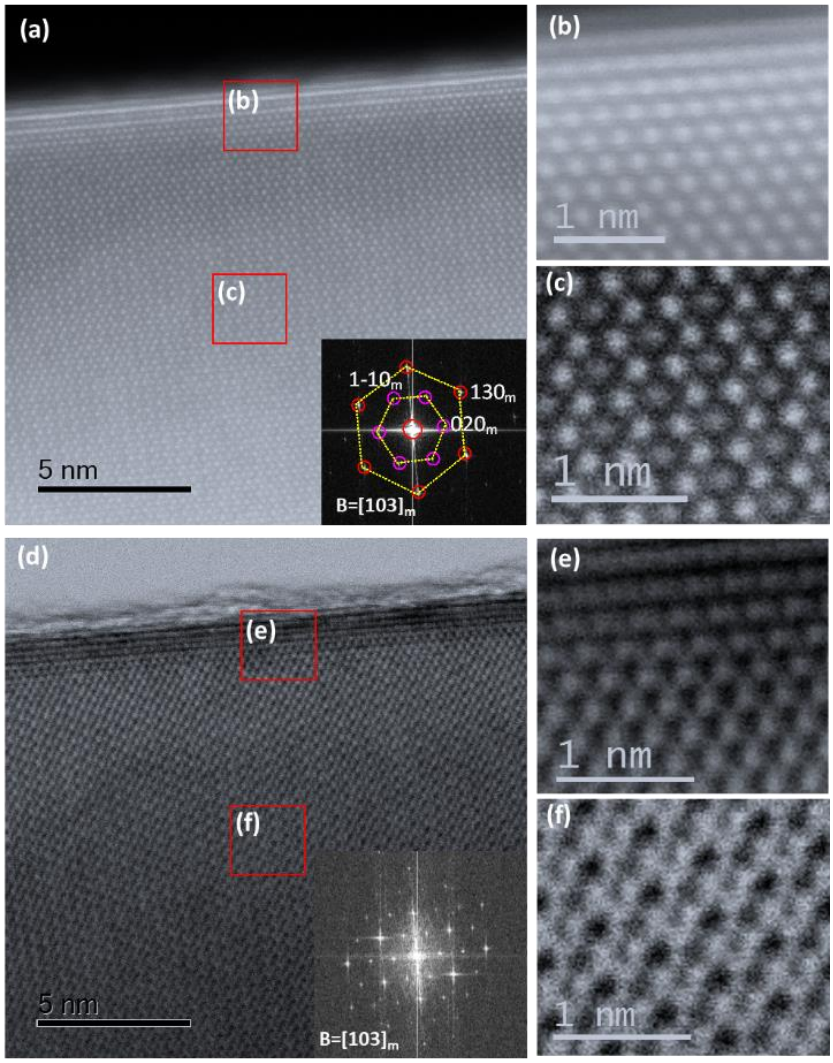

Figure 5.27 (a-c) HAADF, (d-f) ABF STEM images and FFT patterns (inset in (a) and (d)) from frontal view of the selected nanosheet.

Because the annular bright-field (ABF) - STEM technology is sensitive to low-Z elements, a combination of HAADF and ABF STEM measurements was carried out for visualizing the local atomic structure of LLNMO-750-2. Figure 5.27 shows the HAADF and ABF images taken from frontal view of the nanosheet ($[103]_m$ orientation). The centre of hexagon demonstrates a comparatively low intensity because the column is shared by Li and TM ions. Very importantly, the arrangement of the metal cations in this plane (i.e. $(001)_m$ face) is unique to the monoclinic structure and cannot be generated by a crystal with a rhombohedral structure ($R\bar{3}m$). HAADF profiles and FFT patterns (Figure 5.27, inset) further offer evidence for the quasi-hexagonal symmetry of the $(001)_m$ plane in the real space. This kind of contrast is found throughout the selected particles ruling out to some extent that a composite of two layered nano-domains ($C2/m$ and $R\bar{3}m$) is present in a single crystallite for our sample.

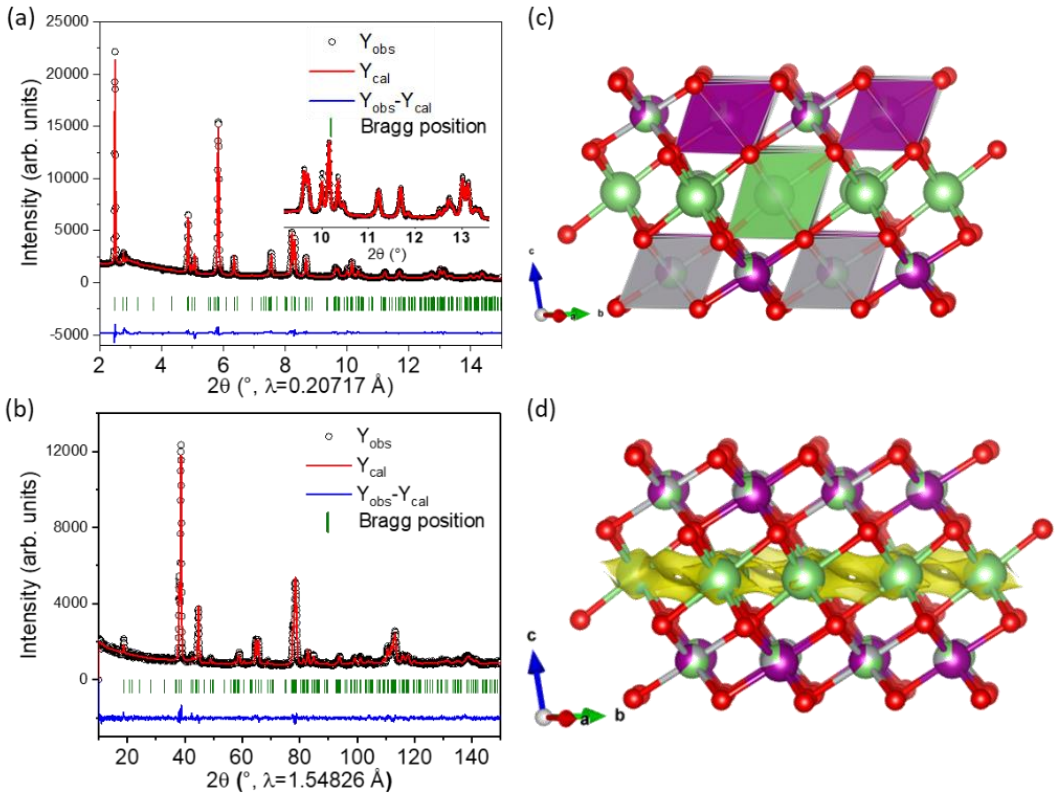

Figure 5.28 Simultaneous Rietveld refinement on (a) SRD and (b) NPD patterns of LLNMO-750-2; (c) the obtained structural model of $Li_{1.2}Ni_{0.2}Mn_{0.6}O_2$, and (d) possible two dimensional diffusion pathway of lithium ions in the $Li_{1.2}Ni_{0.2}Mn_{0.6}O_2$ structure as deduced from bond valence sum (BVS) iso-surfaces (yellow).

High-resolution NPD is a powerful tool to discriminate between Ni and Mn, and to really detect Li (see the following neutron scattering factor, Li: -1.90 fm; Ni: 10.3 fm; Mn: -3.73 fm; O: 5.803 fm), while high-resolution SRD helps to gain the precise lattice parameter and symmetry. Therefore, a simultaneous refinement against SRD and NPD of LLNMO-750-2 was utilized to determine the real structure of LLNMO-750-2. Rietveld refinement was performed by assuming a single monoclinic layered structure model with the space group of *C*2/*m*, see Figure 5.28 and Table 5.5, the small weighted profile (R_{wp}) evidences the proposal structure model is reliable. Figure 5.28(c) shows a section of the monoclinic crystal structure using the structural parameters obtained from the Rietveld refinement, in which the atoms shown by cyan, red, purple, and gray colour correspond to Li, O, Mn and Ni, respectively. Figure 5.28(d) exhibits the differential bond valence map [102] of lithium in the structure, showing the possible 2D diffusion pathway for Li-ions. The resulting chemical composition of LLNMO-750-2 is very close to the target composition (i.e. $Li[Li_{0.2}Ni_{0.2}Mn_{0.6}]O_2$). Taking the analysis of SRD, NPD, ABF- and HAADF- STEM images into account, these results confirm that the structure of LLNMO-750-2 is a single monoclinic solid solution layered structure.

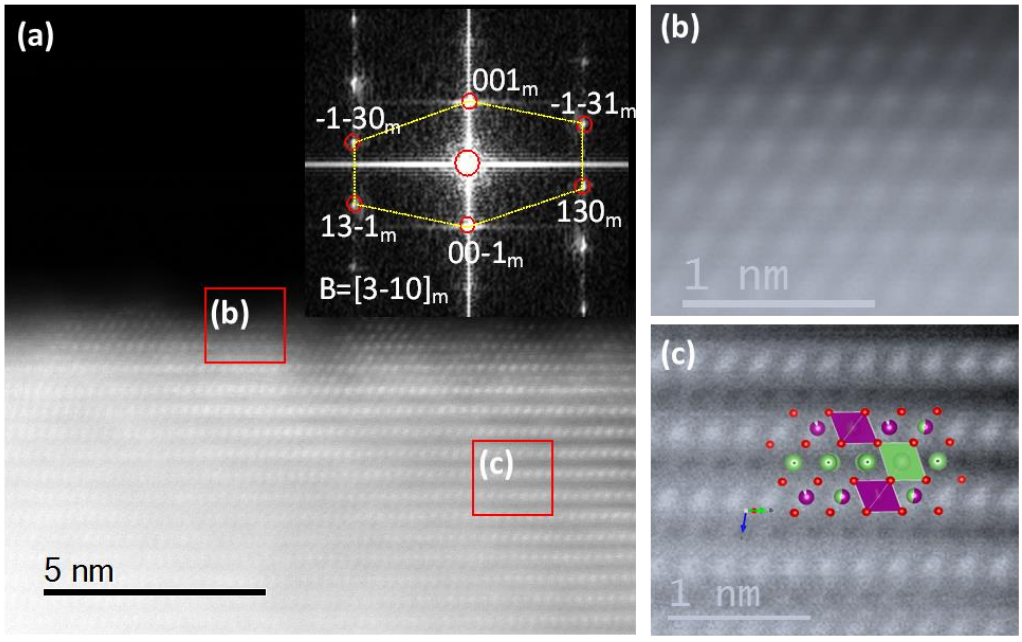

Figure 5.29 (a-c) HAADF and (d-f) ABF STEM images and FFT patterns (inset in (a) and (d)) along lateral view of LLNMO-750-2.

Figure 5.29 shows the HAADF-STEM images of LLNMO-750-2 with the $[3\bar{1}0]_m$ zone axis. Only TM atoms located on octahedral positions can be observed, indicating the completion of the

spinel/rock-salt-type to layered phase transition. It is worth to mention that the HAADF-STEM images virtually present only the signal of nickel and manganese, and it is almost impossible to distinguish Mn from Ni in the STEM images because their scattering power is nearly identical. Since no evident lithium signal is observed in ABF-STEM images, the conclusion on Li and TM migrations are thus indirectly deduced from the TM lattice of corresponding structure models.

Table 5.5 Crystallographic parameters of LLNMO-750-2.

Cell parameters

Space group: *C*2/*m*, a = 4.9628 Å, b = 8.5662 Å, c = 5.0324 Å , V = 201.9245 Å^3, β = 109.29°

Atomic positions

Name	site	*x*	*y*	*z*	B_{iso}	Fract
Li1	2*c*	0.000	0.000	0.500	0.102	1.000
Li2	4*h*	0.000	0.684	0.500	0.102	0.944
Ni2	4*h*	0.000	0.684	0.500	0.102	0.056
Ni1	2*b*	0.000	0.500	0.000	0.102	0.205
Li3	2*b*	0.000	0.500	0.000	0.102	0.416
Mn2	2*b*	0.000	0.500	0.000	0.102	0.380
Mn1	4*g*	0.000	0.176	0.000	0.102	0.710
Ni3	4*g*	0.000	0.176	0.000	0.102	0.142
Li4	4*g*	0.000	0.176	0.000	0.102	0.149
O1	4*i*	0.215	0.000	0.222	0.887	1.000
O2	8*j*	0.249	0.332	0.226	0.616	1.000

Refinement parameters

R_{wp}= 2.80 %, R_p= 4.49 %, χ^2: 2.36 for synchrotron radiation powder diffraction

R_{wp}= 3.70 %, R_p= 4.80 %, χ^2: 2.08 for neutron powder diffraction

Selected interatomic distance (Å)

Li1-O1 bond length: 2.017(5); Li2-O1 bond length: 2.266(4)

Ni1-O1 bond length: 2.074(8); Ni1-O2 bond length: 1.990(7)

Mn1-O1 bond length: 1.964(6); Mn1-O2 bond length: 1.924(6)

Note: B_{iso} is the thermal displacement parameter, Fract is the fractional occupancy of the atom on this site.

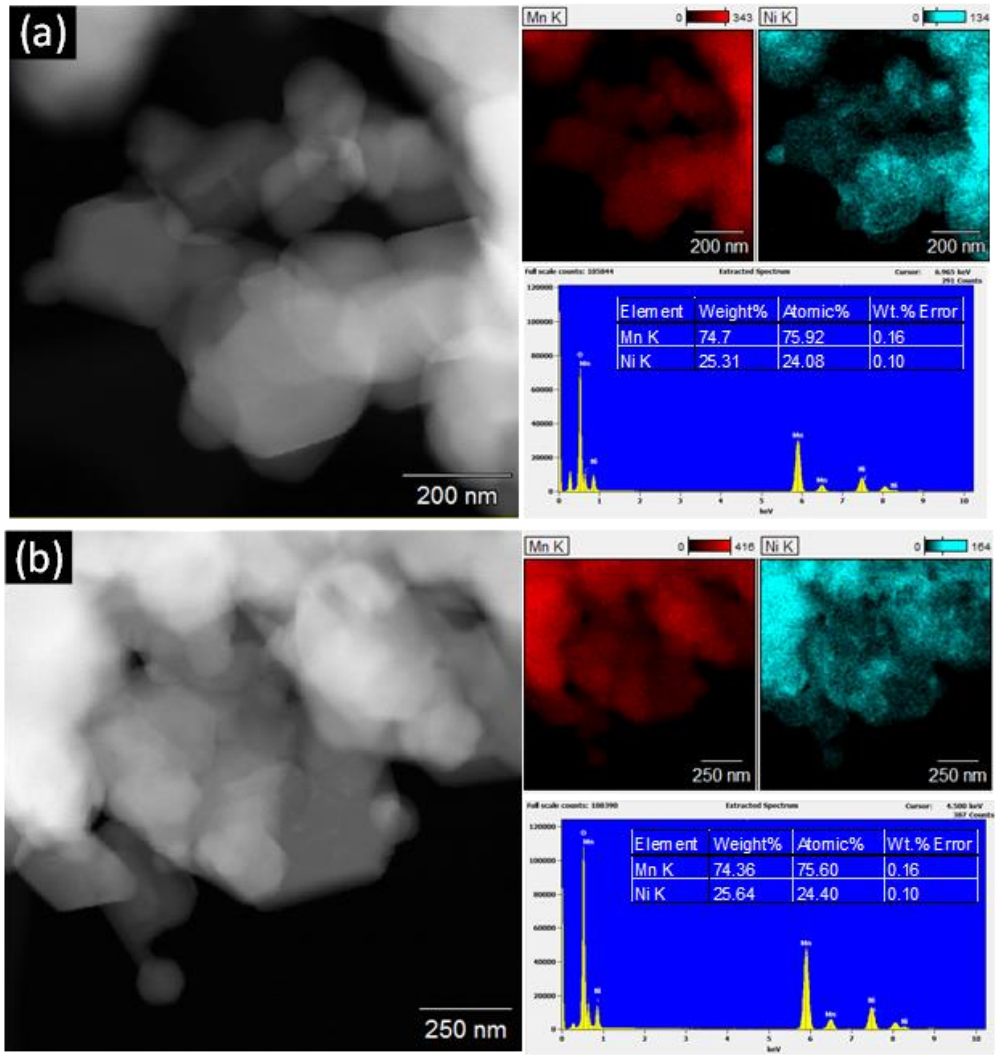

Figure 5.30 HAADF-STEM-EDX results of LLNMO-750-2.

Additionally, Figure 5.27 and Figure 5.29 also shows an ultra-thin surface with antisite defects. The atomic ratios of Mn:Ni in the LLNMO-750-2 is very to the theoretical value (i.e. 3:1), see Figure 5.30. STEM-EDX maps indicate that small amounts of nickel migrates to the surface at the expense of manganese, resulting in the heterogeneity of atomic composition at the surface. This nanoscale gradient in LLNMO-750-2 is probably ascribed to the electron beam damage and/or the surface reconstruction induced by Li/O loss. However, when compared with the nickel surface segregation of LLNMO-650-2, the surface migration of nickel on LLNMO-750-2 is highly alleviated. It is very interesting that the cubic spinel/rock-salt-type phase is only observed in the interior part of heterostructured LLNMO-650-2, while at a higher preparation temperature the layered oxide, i.e. LLNMO-750-2, in surface near regions transforms back to the cubic spinel/rock-

salt-type phase. This surface reconstruction might be a result of Li/O incorporation into the crystal surface at a lower temperature of 650 °C, and a small amount of Li/O release from surface at 750 °C.

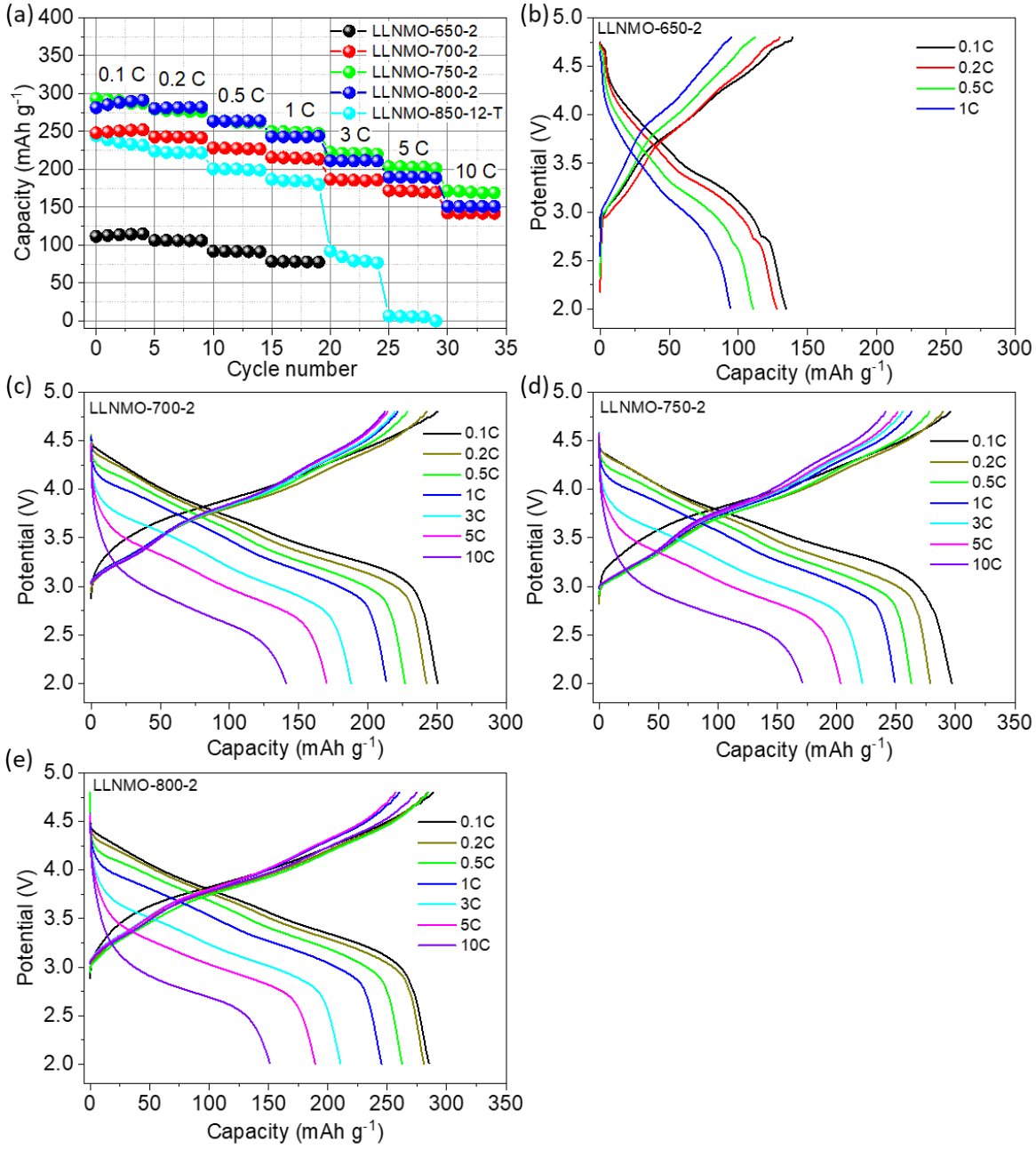

Figure 5.31 Rate capabilities and the corresponding charge-discharge curves of the electrodes.

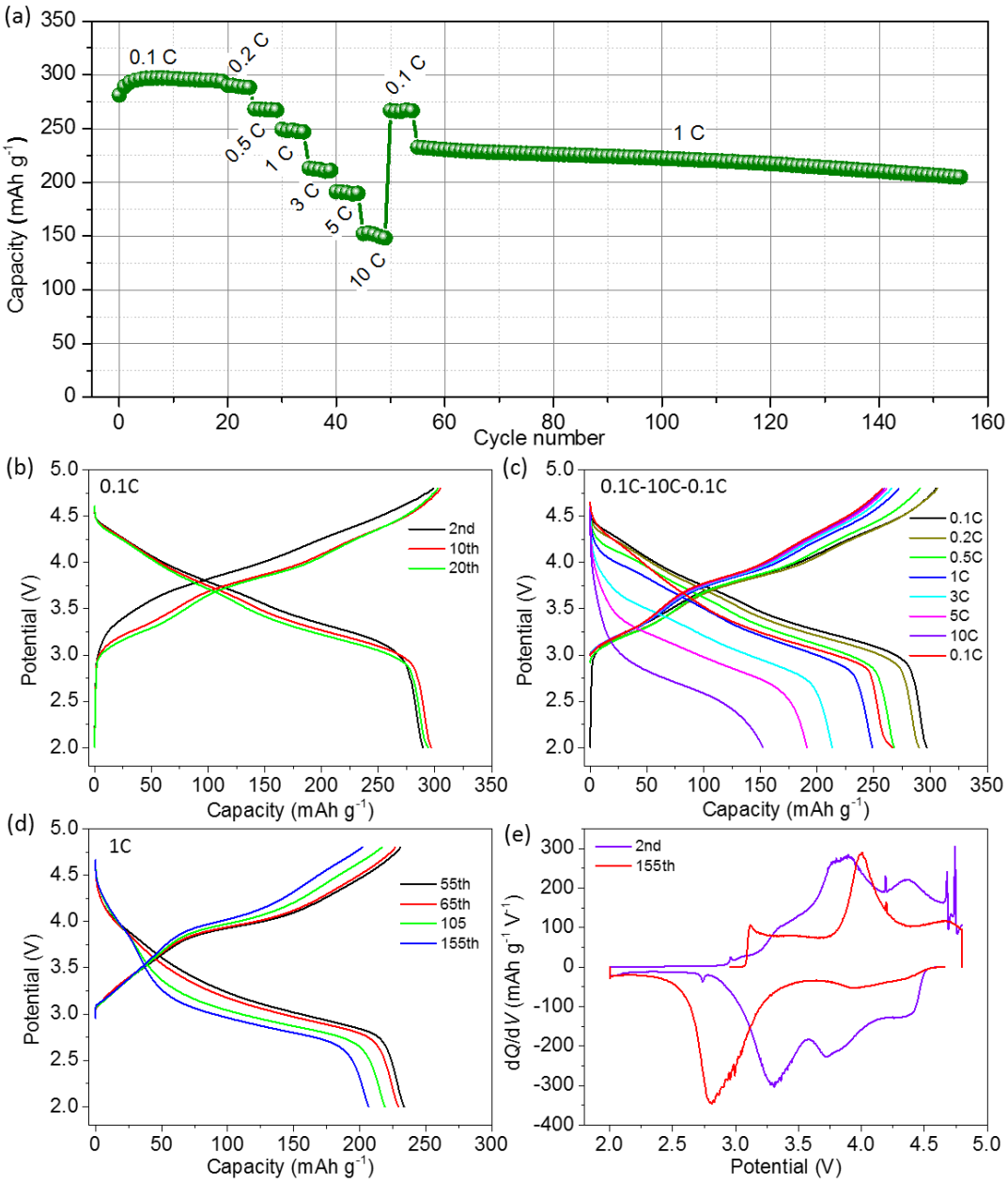

Figure 5.32 (a) The comprehensive electrochemical performance, (b-d) the charge-discharge profiles and (e) the dQ/dV curves of LLNMO-750-2 electrode.

In order to unravel the relationship between crystal structure and electrochemical properties, electrochemical characterizations were performed on CR2032-type coin cells at room temperature. The cells were galvanostatically charged to 4.8 V using a current density of 0.1 C (1 C = 320 mA g^{-1}) and discharged to 2.0 V at various C-rates from 0.1 to 10 C. The high-rate capabilities of the cathodes are shown in Figure 5.31. LLNMO-650-2 with a multiple-phase composition delivers a much lower discharge specific capacity of 111 mAh g^{-1} at 0.1 C compared to other electrodes (>

250 mAh g^{-1}). It can be seen that LLNMO-750-2 shows the best rate performance, which is also higher than that of the $Li_{1.2}Ni_{0.2}Mn_{0.6}O_2$ electrode material prepared by traditional furnace heating at 850 °C for 12 hours (LLNMO-850-12-T). The specific discharge capacities of LLNMO-750-2 electrode at 0.1 C, 3 C, 5 C and 10 C are 293, 222, 203 and 171 mAh g^{-1}, respectively, see Figure 5.31(f), which are superior to the latest reported values for Li-rich cathodes in the same voltage window (Table 5.6).[40,71,103–109]

Figure 5.32(a) presents a comprehensive high-rate performance test of LLNMO-750-2 and the corresponding charge-discharge plots displayed in Figure 5.32(b-d). The specific discharge capacity (around 290 mAh g^{-1}) at 0.1 C is slightly increased due to the activation process [110] and no pronounced voltage decay is found after 20 cycles. The capacity gradually decreases with raising the current density, and the reversible capacity is 270 mAh g^{-1} at 0.1 C after ultra-high charge and discharge process. Furthermore, the long-term cycling performance of LLNMO-750-2 was tested at 1 C for 100 cycles. The electrode still exhibits a high discharge capacity of 200 mAh g^{-1} after prolonged cycling. The improved electrochemical performance of LLNMO-750-2 is ascribed not only to the optimized phase composition, but also to the proper microwave calcination temperature. The LLNMO-650-2 obtained at a lower temperature is composed of multiple phases with the large lattice mismatch that can induce a higher activation barrier for Li-ion diffusion and thus lower capacity.[111] As shown in Figure 5.16, large and dense particles can be easily formed at high temperature since crystal growth rate is increased exponentially with increasing annealing temperature.[62,109] Unfortunately, a large crystal size and a low porosity architecture might not be beneficial for the charge (Li-ions and electrons) transport, resulting in a worse electrochemical property for LLNMO-800-2.

Table 5.6 Comparison of the electrochemical performances of the LLNMO-750-2 with reported results.

Sample	Strategies	Discharge Capacity (mAh g^{-1}) between 2.0 and 4.8 V	Ref.
$Li[Li_{0.2}Mn_{0.568}Ni_{0.2}Sn_{0.032}]O_2$	Doping	125 (100 mA g^{-1})	[103]
Ultrathin Spinel Membrane coated $Li_{1.2}Ni_{0.2}Mn_{0.6}O_2$	Surface modification	~ 125 (10 C); 200 (5 C)	[104]
Li_2MnO_3 coated $0.5Li_2MnO_3$–$0.5LiNi_{0.44}Mn_{0.32}Co_{0.24}O_2$		~ 120 (10 C); 153 (5 C)	[40]
Heterostructured $Li_{1.2}Ni_{0.2}Mn_{0.6}O_2$	Coprecipitation followed by solid-state reaction	~ 160 (5 C)	[71]
Hierarchical structured $Li_{1.2}Ni_{0.2}Mn_{0.6}O_2$	Hydrothermal method with organic solvent and calcination route	163 (10 C); 188 (5 C)	[105]
Heterostructured $Li_{1.2}Ni_{0.2}Co_{0.08}Mn_{0.52}O_2$ nanoplates		~ 180 (5 C)	[106]
Hetero-epitaxial nanostructured $Li_{1.26-x}Ni_{0.11}Co_{0.04}Mn_{0.59}O_2$ ($0 < x < 0.3$)		200 (5 C)	[108]
Porous hierarchical structured $Li_{1.2}Ni_{0.12}Co_{0.12}Mn_{0.56}O_2$		176 (5 C)	[107]
LLNMO-750-2	Fast coprecipitation coupled with microwave annealing method	171 (10 C); 203 (5 C)	This work

5.4 Degradation mechanism of layered $Li[Li_{0.2}Ni_{0.2}Mn_{0.6}]O_2$ cathodes

Despite the fact that the LLNMO-750-2 cathode displays an excellent rate performance, a plateau at about 2.7 V is obvious after 155 cycles, see Figure 5.32 in section 5.3.5, suggesting a transformation from layered to spinel-like phase for a small amount of the active material. In this section, to figure out the reasons why the LLNMO-750-2 electrode suffers from the obvious voltage decay, *in situ* high-resolution SRD was firstly used to study the structural evolution of LLNMO-750-2 during the first cycle. High-resolution TEM and electron diffraction were utilized to investigate the mechanical and structural degradation of LLNMO-750-2 cathode after 155 cycles. *In situ* high-resolution synchrotron diffraction was exploited to understand the underlying voltage decay in LLNMO-750-2 after ten cycles.

5.4.1 Unit cell 'breathing mechanism' of LLNMO-750-2 cathode during the first cycle

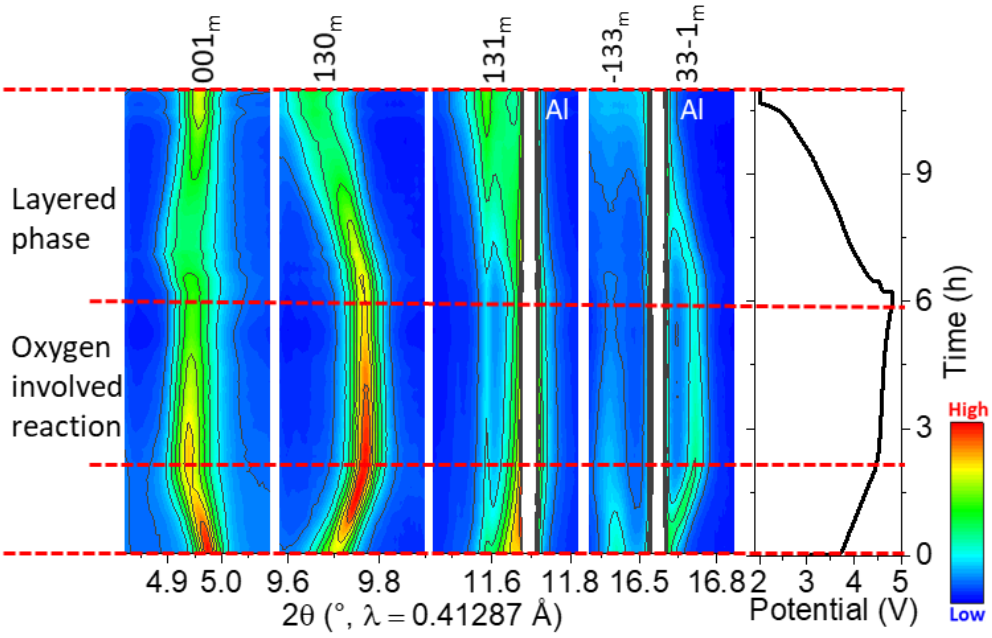

Figure 5.33 In situ high-resolution SRD patterns of layered LLNMO-750-2 during first charge and discharge process between 2.0 and 4.8 V.

In order to clearly illustrate the structural evolution of the LLNMO-750-2 electrode during the first cycle, the contour plots of the reflection intensity and position for several main reflections as a function of reaction time are exhibited in Figure 5.33. All reflections in the *in situ* SRD patterns of LLNMO-750-2 can be indexed according to a layered structure with *C*2/*m* space group

symmetry, except for strong reflections at ~ 11.7° and ~ 16.6°, which originate from the Al current collector. It should be mentioned that 001_m and $\bar{1}33_m$ reflections sensitively reflect the changes along *c* axis, while the 130_m and $33\bar{1}_m$ reflections are indicative of the evolution concerning the *a* and *b* axis of the monoclinic layered structure.

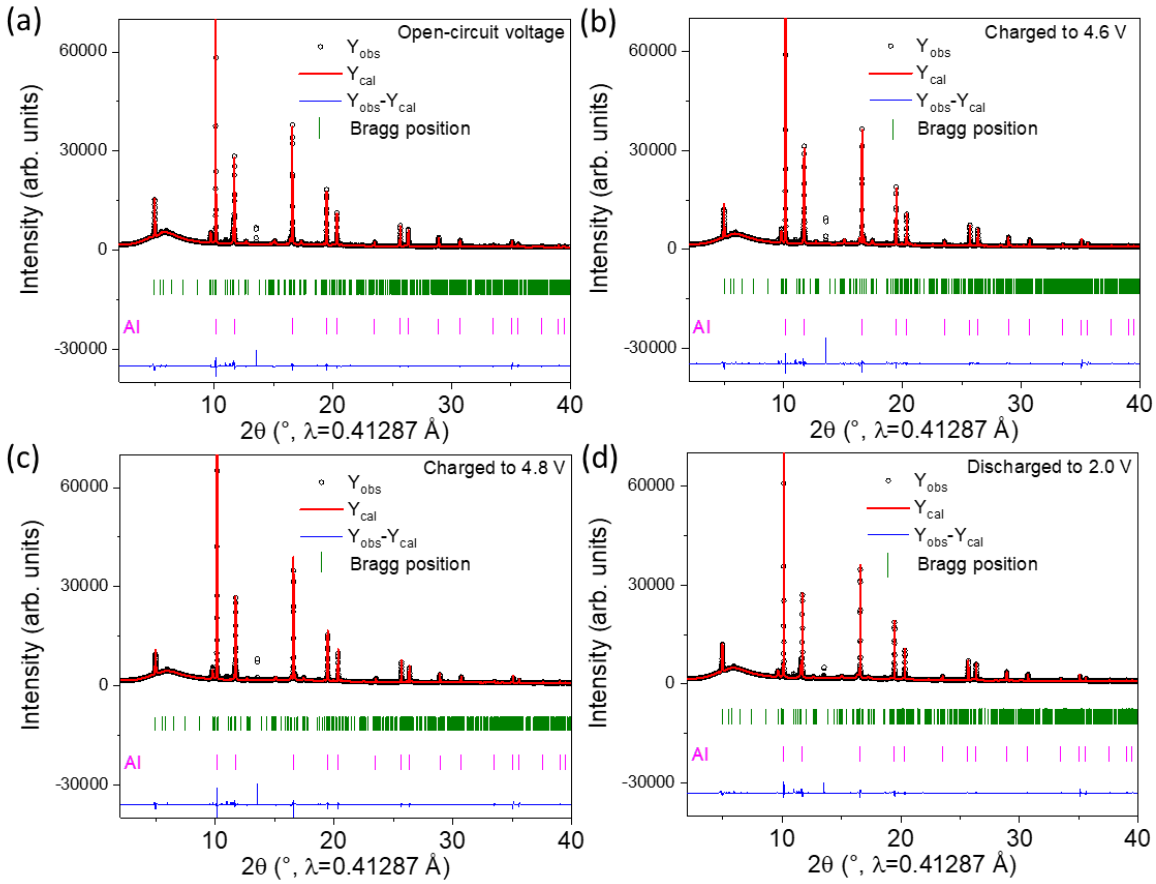

Figure 5.34 Rietveld refinement revealing the structural evolution of LLNMO-750-2 electrode: (a) open-circuit voltage; (b) charged to 4.6 V; (c) charged to 4.8 V and (d) discharged to 2.0 V.

During first charging process, the 001_m and $\bar{1}33_m$ reflections continuously shift to lower scattering angles between the open-circuit voltage and 4.5 V, while 130_m and $33\bar{1}_m$ reflections move to higher 2-theta angles, indicating a solid solution reaction with an increasing *c* parameter and reduced lattice parameters of *a* and *b* as for the layered monoclinic phase. In the voltage region from 4.5 to ~ 4.8 V, the 001_m and $\bar{1}33_m$ reflections slightly shift back to higher angles but 130_m and $33\bar{1}_m$ reflections remain nearly constant, revealing that the *c*-lattice parameter is relatively compressed again and the lattice constants of *a* and *b* remain almost the same beyond 4.5 V upon loss of the Li ions. This is in good agreement with a smooth and monotonous charging feature

within the low voltage window and a pronounced voltage plateau (electrochemical activation process) at about 4.6 V, respectively. During lithiation (discharge) period, all the reflections tend to move back to their initial position signifying the evolution of lattice parameters in the reverse direction.

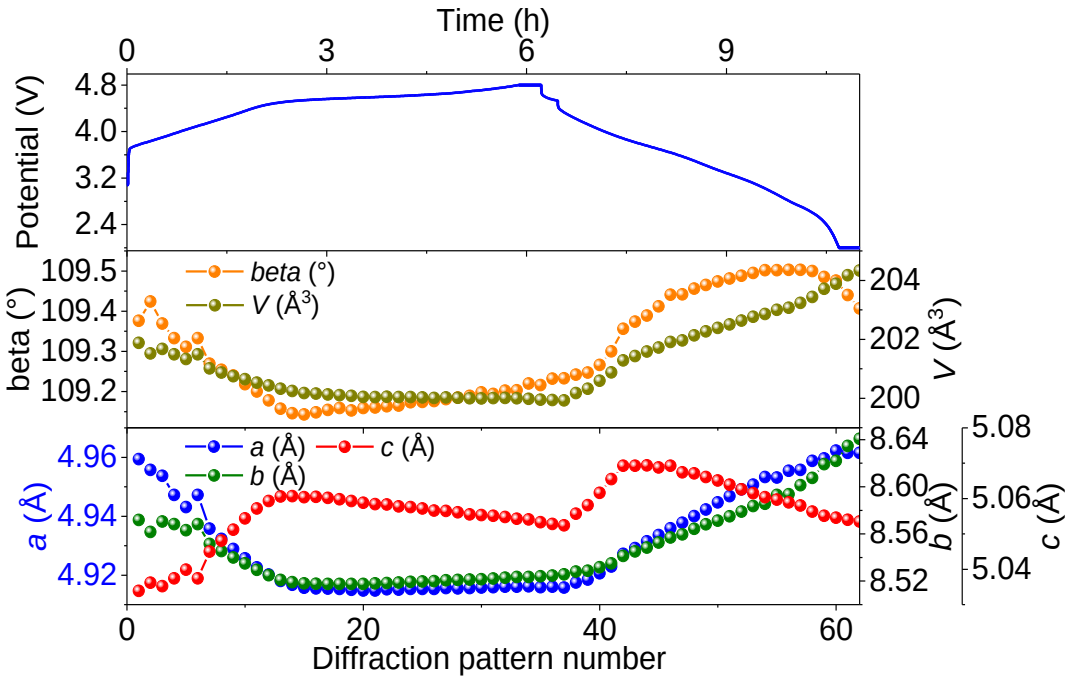

Figure 5.35 Evolution of lattice parameters versus diffraction pattern number as obtained from Rietveld refinement to in situ SRD measurements of LLNMO-750-2 electrode during the first cycle.

Each *in situ* SRD pattern during first cycle was fitted using Rietveld refinement with the *C*2/*m* structure model, see Figure 5.34. The corresponding lattice parameters obtained are shown in Figure 5.35. From open-circuit voltage to 4.5 V, parameter *c* of the layered monoclinic phase increases from 5.034(1) to 5.061(1) Å. The expansion of the *c* value is supposed to be caused by the increased electrostatic repulsive force within the fcc oxygen lattice resulting from the decreased number of lithium ions in the lithium layer of LLNMO-750-2. The parameter *a* decreases from 4.959(1) to 4.917(1) Å, and the parameter *b* reduces from 8.572(1) to 8.519(1) Å, respectively. The contracting *a* and *b* parameters can be ascribed to the reducing radii of Ni cations at higher valence states ($Ni^{2+} \rightarrow Ni^{4+} + 2e^-$) [112]. With the voltage further increasing to 4.8 V, lattice parameter *c* shows a slight decrease from 5.061(1) to 5.055(1) Å and the parameters of *a* and *b* do not change noticeably as a significant amount of lithium ($0.4 < x < 1.2$) is extracted from the layered $Li_{1.2-x}Ni_{0.2}Mn_{0.6}O_2$. This phenomenon is probably attributed to the formation of oxygen

vacancy or spinel-like nano-domains, which results from the oxygen release and the TM migration, leading to a reduction of the electrostatic repulsion between oxygen-oxygen layers along the *c*-axis.[89] During the lithiation (discharge), the lattice parameter *c* increases significantly and then decreases slightly, but it does not reach the original value before cycling. The difference in lattice constant *a*, *b* and *c* before and after the first cycle is 0.002(1) Å, 0.069(1) Å, and 0.019(1) Å, respectively. This discrepancy can be ascribed to the irreversible loss of Li and/or oxygen after activation process and thus resulting in a low coulombic efficiency of the LLNMO-750-2 electrode (~ 78 %) in the first cycle.

5.4.2 Mechanical degradation of LLNMO-750-2 cathode after long-term cycling

After 155 cycles, severe fractures on the nanosheets can clearly be revealed from STEM images shown in in Figure 5.36(a), demonstrating the mechanical degradation of the cycled LLNMO-750-2 cathode material. This can be attributed to the volume variation induced by anisotropic lattice strain during non-equilibrium (de)lithiation. The STEM and SAED patterns of the cycled electrode manifest a co-signature of monoclinic and cubic phase, as shown in Figure 5.39(b & c), revealing that a part of the layered structure converts to the spinel/rock-salt-type structure after lithium loss and oxygen evolution during prolonged cycling. A previous study suggested that this spinel-like phase is the main contributing factor for the voltage fading of the LLOs.[11]

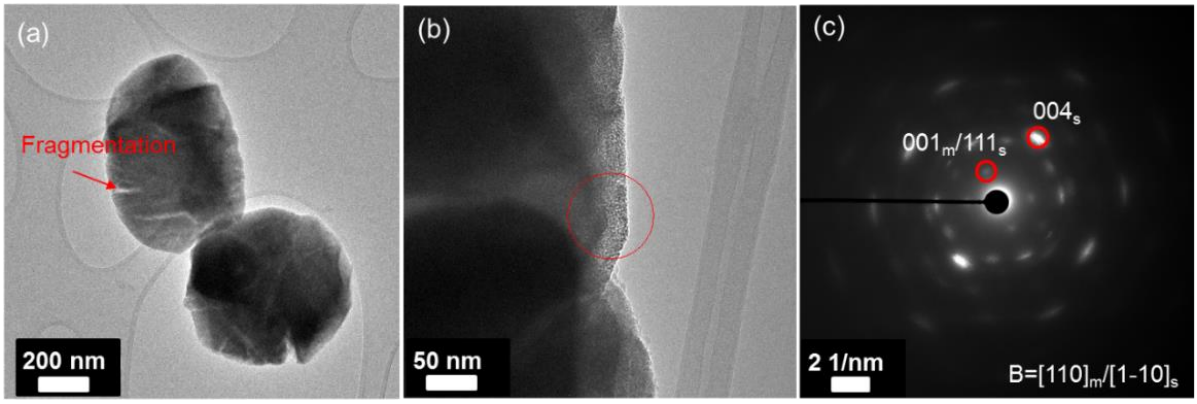

Figure 5.36 (a-b) STEM images and (c) SAED patterns of the LLNMO-750-2 electrode after long-term cycling.

5.4.3 Structural evolution of LLNMO-750-2 cathode during the 11th cycle

In situ SRD technique was exploited to further trace the structural evolution of LLNMO-750-2 electrode after 10 cycles, as shown in Figure 5.37 and 5.39. During delithiation, the 001_m and $\bar{1}33_m$ reflections gradually shift to lower scattering angles and then back to higher angles, revealing the

expansion and contraction of the *c*-lattice parameter during the removal of lithium ions from layered matrix. At the same time, the 130_m and $33\bar{1}_m$ reflections shift to higher scattering angles, demonstrating the reduction of the *a* and *b* lattice constants.[10,113] During lithiation, the changes of these reflections reverse directions but no pronounced activation process is found, demonstrating a typical solid solution reaction mechanism for the layered phase.

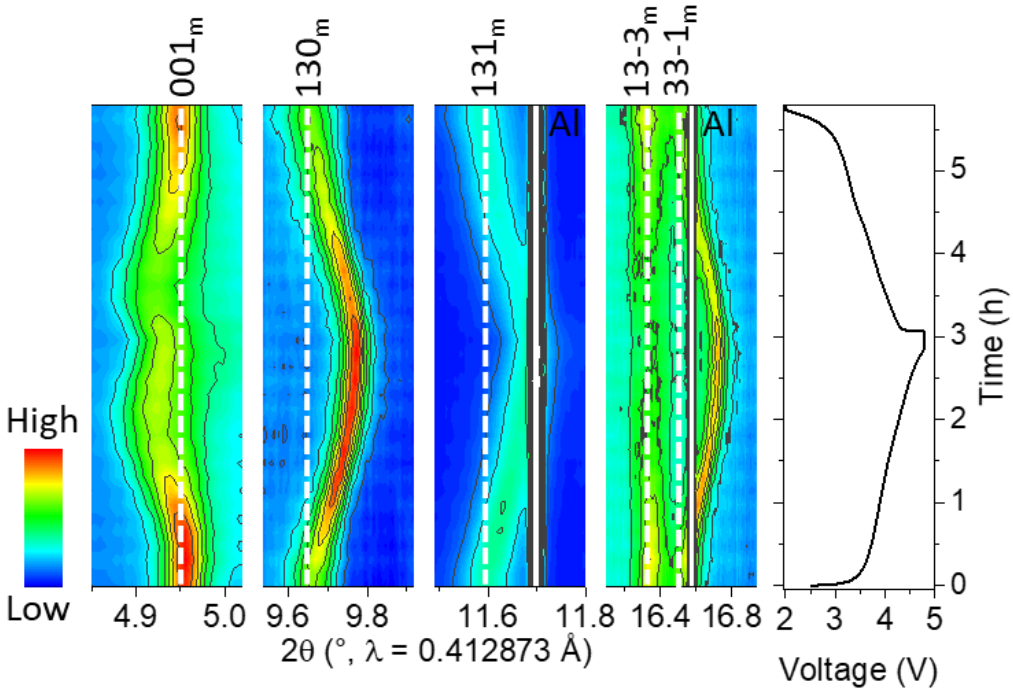

Figure 5.37 In situ SRD patterns of LLNMO-750-2 electrode during the 11th cycle.

The changes in the lattice parameters during the 11th de-lithiation and lithiation process are shown in Figure 5.39. Upon charging, *a* and *b* lattice parameters gradually decrease as the number of lithium ions is decreasing in the layered host structure, corresponding to reduced ionic radii of TM ions. In contrast, *c* parameter continuously increases from 5.052(1) Å at ~ 2.4 V to 5.074(1) Å at ~ 4.3 V, and it reduces rapidly to 5.061(1) Å at 4.8 V (vice versa during discharging), suggesting a severe structural 'collapse' in *c* direction upon deep de-lithiation to high cut-off voltage of 4.8 V. When the electrode is charged up to 4.8 V, a broad reflection at around 5.02° in the SRD patterns of LLNMO-750-2 electrode is observed (see Figure 5.37 and Figure 5.38). This might be attributed to the phase instability of highly de-lithiated states that results in the formation of an intermediate phase between layered and spinel phase. It should be mentioned that this intermediate phase probably contributes to the voltage decay in LLOs within the first ten cycles.

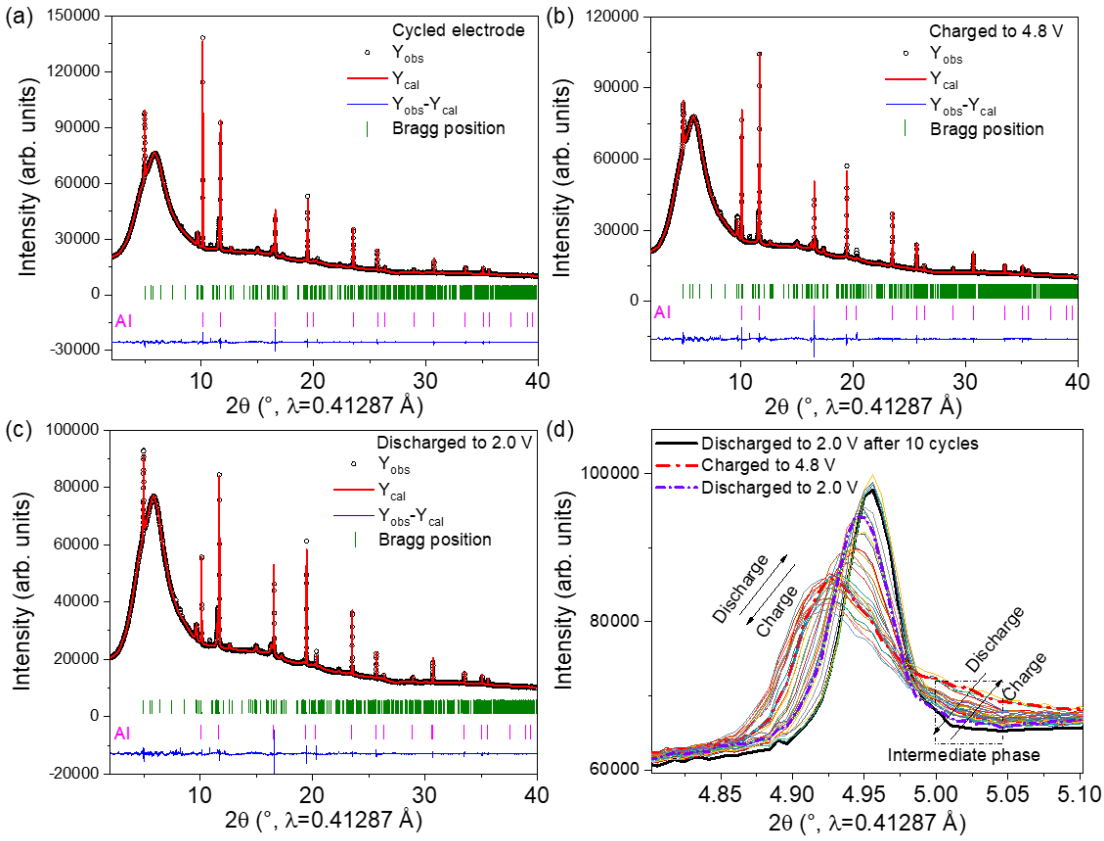

Figure 5.38 Rietveld refinement revealing the structural evolution upon charge/discharge: (a) discharged to 2.0 V after 10 cycles; (b) charged to 4.8 V; (c) discharged to 2.0 V. (d) diffraction patterns of LLNMO-750-2 electrode during the 11th charge and discharge process.

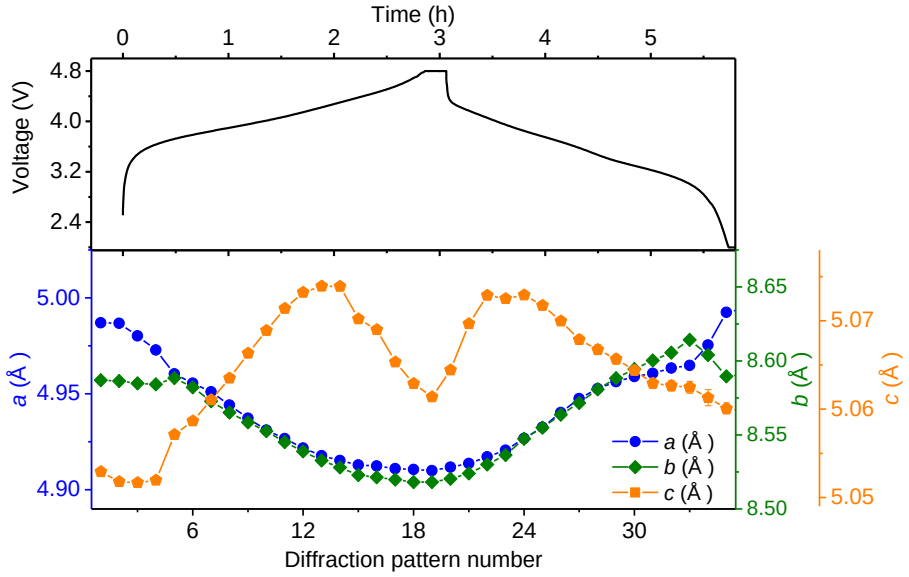

Figure 5.39 Evolution of crystallographic parameters obtained from Rietveld refinement to in situ synchrotron diffraction measurements during the 11th cycle.

5.5 Thermodynamically stable phase of $Li_xNi_{0.2}Mn_{0.6}O_y$

The above results suggest that the undesired transformation/degradation from layered $Li_{1.2}Ni_{0.2}Mn_{0.6}O_2$ to spinel-like phase during cycling is closely related to the lithium-depleted state of charge. Therefore, understanding what is the stable phase of $Li_xNi_{0.2}Mn_{0.6}O_y$ at low Li content is urgently required. A series of thermostable oxides with different concentrations of lithium was synthesized according to the following chemical reaction (5.5):

$$\underbrace{0.2Ni^{2+} + 0.6Mn^{2+} + 2OH^- \xrightarrow{NH_3\cdot H_2O} \xrightarrow{\text{air-drying}} \text{precursor}}_{\text{hydroxide co-precipitation reaction}}$$

$$\underbrace{\text{precursor} + \frac{x}{2}Li_2CO_3 \xrightarrow{850\,^\circ C,12h,air} Li_x\,Ni_{0.2}Mn_{0.6}O_y}_{\text{high-temperature lithiation reaction}}$$

$$(0.00 \leq x \leq 1.52) \qquad (5.5)$$

Correspondingly, the materials prepared by providing different amounts of lithium (*x* value) were labelled as L0.00, L0.08, L0.24, …, L1.52, respectively. The Li concentration in the as-synthesized oxides was somewhat decreased to Li(*x*-δ) due to the evaporation of Li at high temperature, see chemical analysis results of the selected samples (Table 5.7).

Table 5.7 Results of chemical analysis of the samples.

Samples	Molar ratio			
	Li	Ni	Mn	O
L1.28	1.24	0.2	0.55	1.95
L0.40	0.36	0.2	0.55	1.48

Standard deviation: < 2 %.

With lithium insertion into the compounds, the oxygen atoms are supposed to be simultaneously incorporated into $Li_xNi_{0.2}Mn_{0.6}O_y$ (*y* value is oxygen composition) oxides to provide more metal coordination sites. The prepared oxides can be classified according to three regions of offered Li content: (i) L0.00 to L0.40; (ii) L0.40 to L1.20 and (iii) higher than L1.20.

5.5.1 Crystal structure

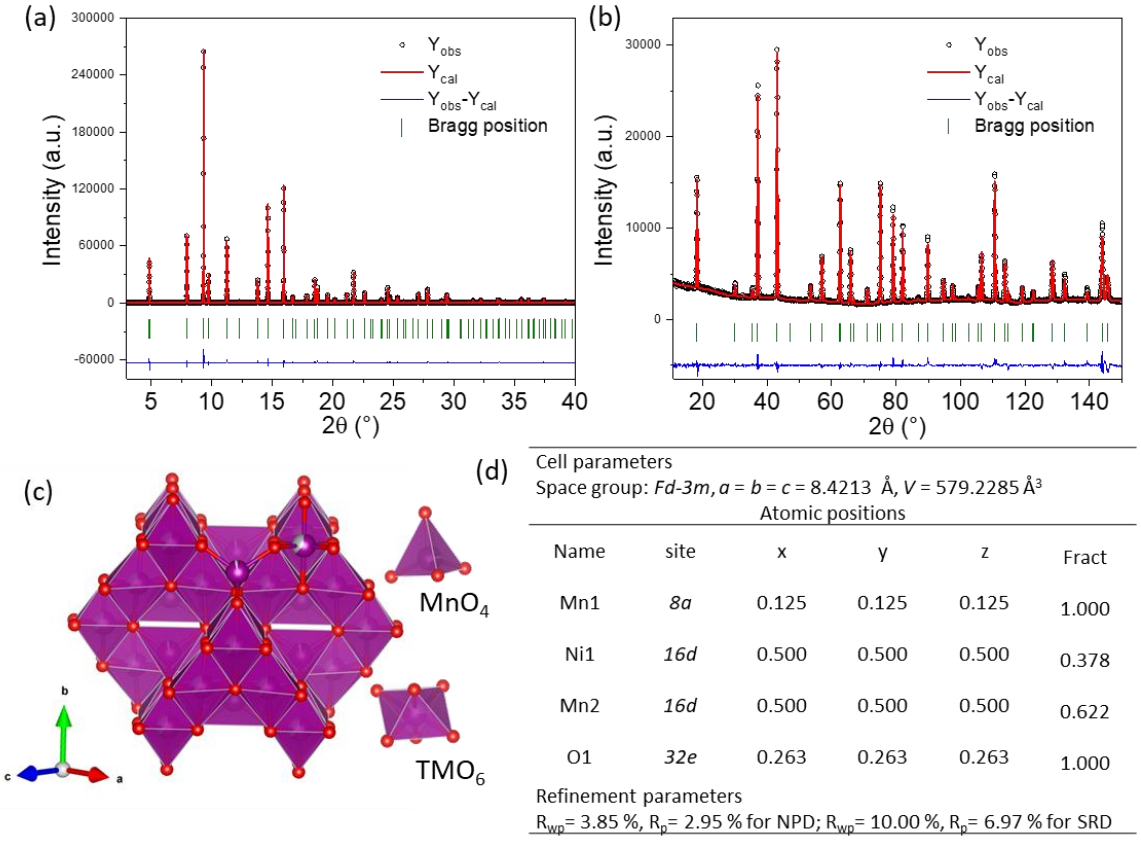

Figure 5.40 Simultaneous Rietveld refinement on (a) SRD (λ = 0.41231 Å) and (b) NPD (λ = 1.54825 Å) patterns of $Ni_{0.75}Mn_{2.25}O_4$ (L0.00); (c) the obtained structure model and (d) crystallographic parameters of L0.00, overall isotropic displacement (temperature) factor is 1.13.

From L0.00 to L0.40, as shown in Figure 5.40, all the reflections in the SRD patterns can be indexed to a single cubic spinel phase with the space group of $Fd\bar{3}m$. Considering that NPD can distinguish the elements with similar atomic numbers such as nickel and manganese, and it can really detect the low-Z elements like lithium, high-resolution NPD and SRD were used to determine the real structure of L0.00 and L0.40. Simultaneous Rietveld refinement results against NPD and SRD data confirm (Figure 5.40) that L0.00 oxide possesses a single spinel phase ($Fd\bar{3}m$) where nickel ions only occupy octahedral (16*d*) sites while manganese ions are located at both tetrahedral and octahedral (8*a* and16*d*) positions, respectively. In contrast, although L0.40 also has a cubic spinel structure ($Fd\bar{3}m$), the tetrahedral sites are mainly occupied by lithium ions and the octahedral positions are mostly occupied by nickel and manganese cations, see Figure 5.41. The obtained chemical formula of L0.00 and L0.40 is around $Mn_{8a}[Ni_{0.75}Mn_{1.25}]_{16d}O_{4\ 32e}$ and

$Li_{8a}[Ni_{0.5}Mn_{1.5}]_{16d}O_{4\ 32e}$, respectively. Therefore, these results provide the first straightforward evidence that lithium is incorporated into the tetrahedral positions of the spinel structure with oxygen uptake.

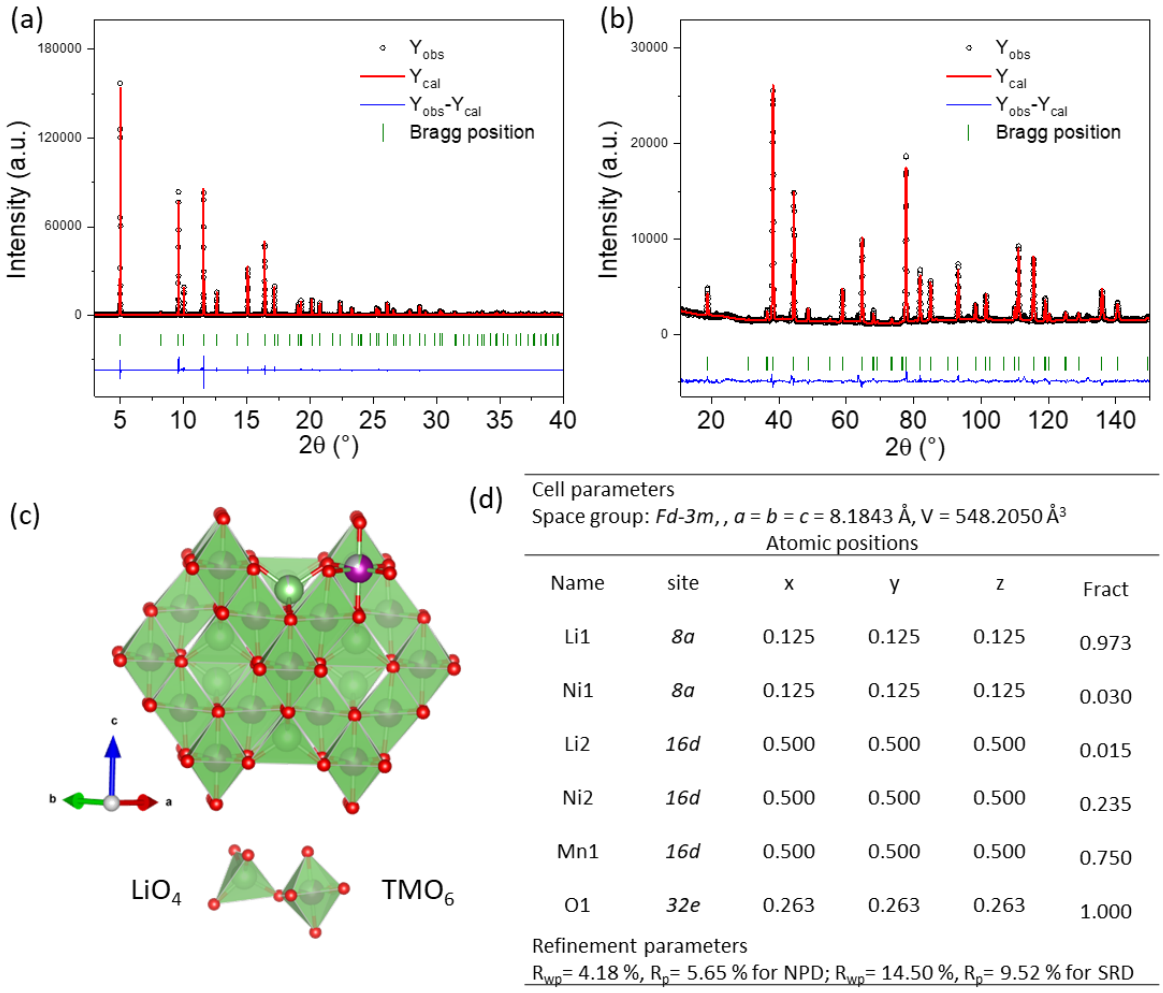

Cell parameters
Space group: *Fd-3m*, , $a = b = c = 8.1843$ Å, V = 548.2050 Å^3

Atomic positions

Name	site	x	y	z	Fract
Li1	*8a*	0.125	0.125	0.125	0.973
Ni1	*8a*	0.125	0.125	0.125	0.030
Li2	*16d*	0.500	0.500	0.500	0.015
Ni2	*16d*	0.500	0.500	0.500	0.235
Mn1	*16d*	0.500	0.500	0.500	0.750
O1	*32e*	0.263	0.263	0.263	1.000

Refinement parameters
R_{wp}= 4.18 %, R_p= 5.65 % for NPD; R_{wp}= 14.50 %, R_p= 9.52 % for SRD

Figure 5.41 Simultaneous Rietveld refinement on (a) SRD (λ = 0.41231 Å) and (b) NPD (λ = 1.54825 Å) patterns of $LiNi_{0.5}Mn_{1.5}O_4$ (L0.40); (c) the obtained structure model and (d) crystallographic parameters of L0.40, overall isotropic displacement (temperature) factor is 0.64.

To estimate the fractional occupancy of Li and TM cations on the tetrahedral and octahedral positions in the cubic spinel structure for the whole series from L0.00 to L0.40, Rietveld refinements on SRD were performed by using the structure model $Li_x\ Mn_{1-x_{8a}}[Li_y\ Mn_{1-y}]_{16d}O_{4\ 32e}$ (see Figure 5.42 & 5.43). With increasing lithium amount, the occupancy of lithium ions on 8*a* sites increases considerably from 0 % in L0.00 to ~ 97 % in L0.40,

revealing that lithium ions have a tendency to be preferentially positioned at 8*a* sites. Accordingly, when compared to the nearly constant occupancy of TM ions on 16*d* sites, the occupancy of TM cations on 8*a* positions decreases pronouncedly from ~ 99 % for L0.00 to ~ 4 % for L0.40, suggesting that the TM ions are displaced to be located at octahedral positions induced by insertion of lithium and oxygen. As predicted by the reflections' movement toward higher two-theta angles, refinement results (Table 5.8) demonstrate that the cubic unit cell is getting smaller, revealing the reduced ionic radii of the TM cations with increasing oxidation state of TM cations and/or the long-range crystallographic disorder-to-order transformation in the spinel structure with increasing lithium content.

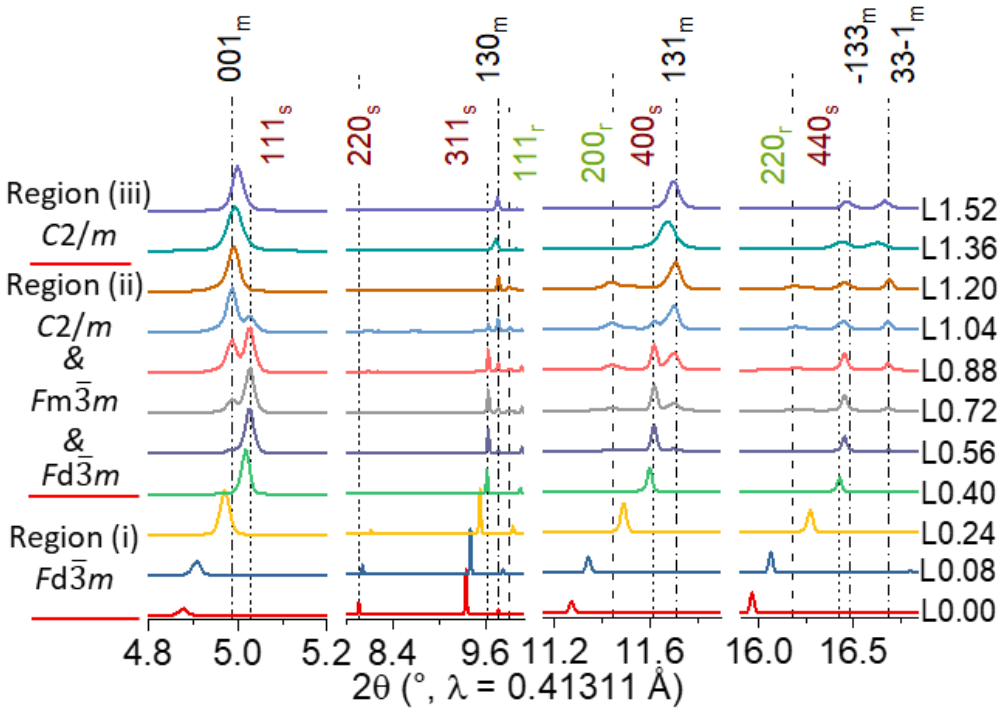

Figure 5.42 High-resolution SRD pattern of the samples (L0.00 to L1.52).

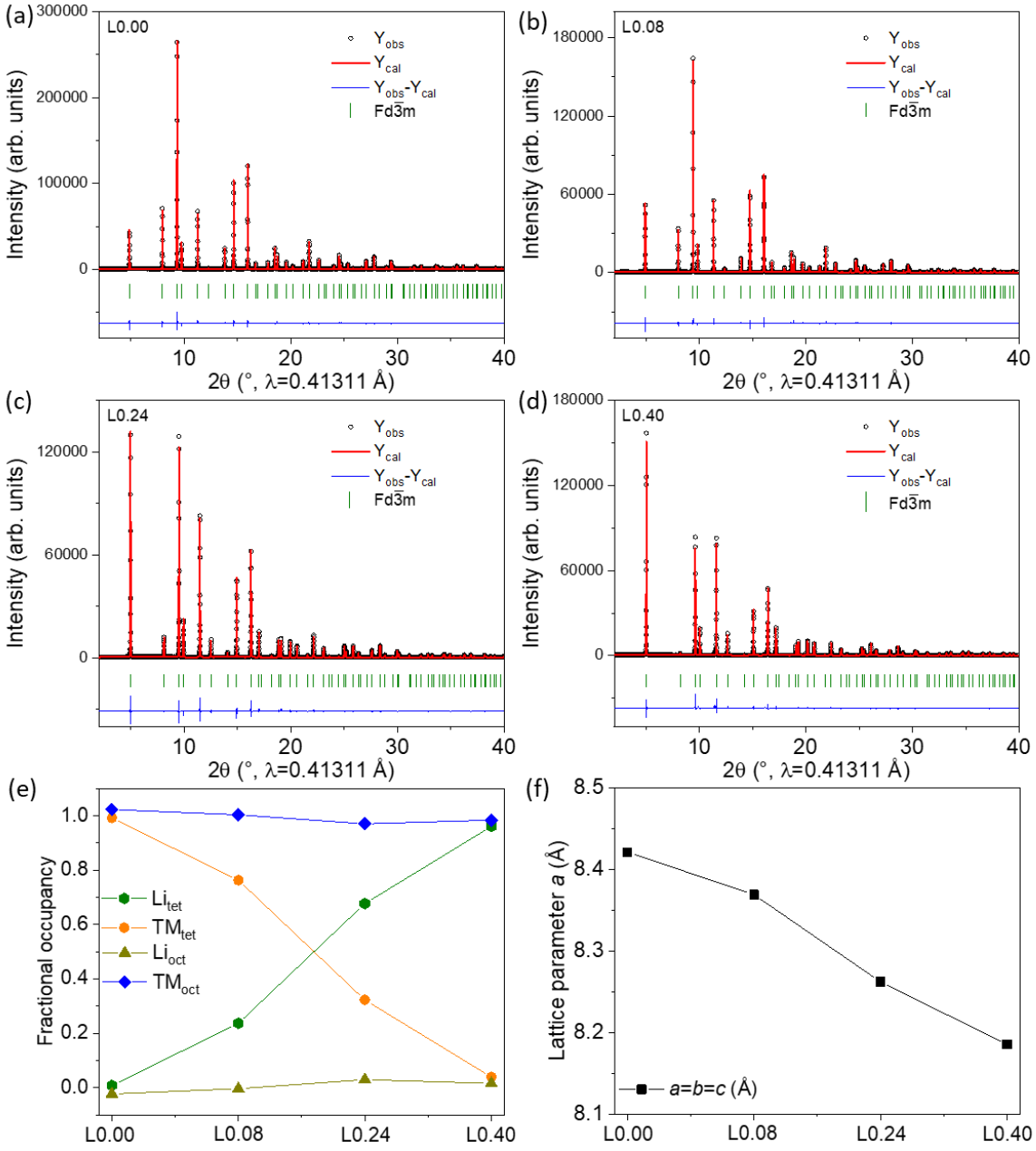

Figure 5.43 Rietveld refinement on synchrotron radiation diffraction patterns of (a) L0.00, (b) L0.08, (c) L0.24 and (d) L0.40 according to the structural model $Li_x\ Mn_{1-x}{}_{8a}[Li_y\ Mn_{1-y}]_{16d}O_4\ {}_{32e}$*; (e and f) the obtained lattice parameters of the samples.*

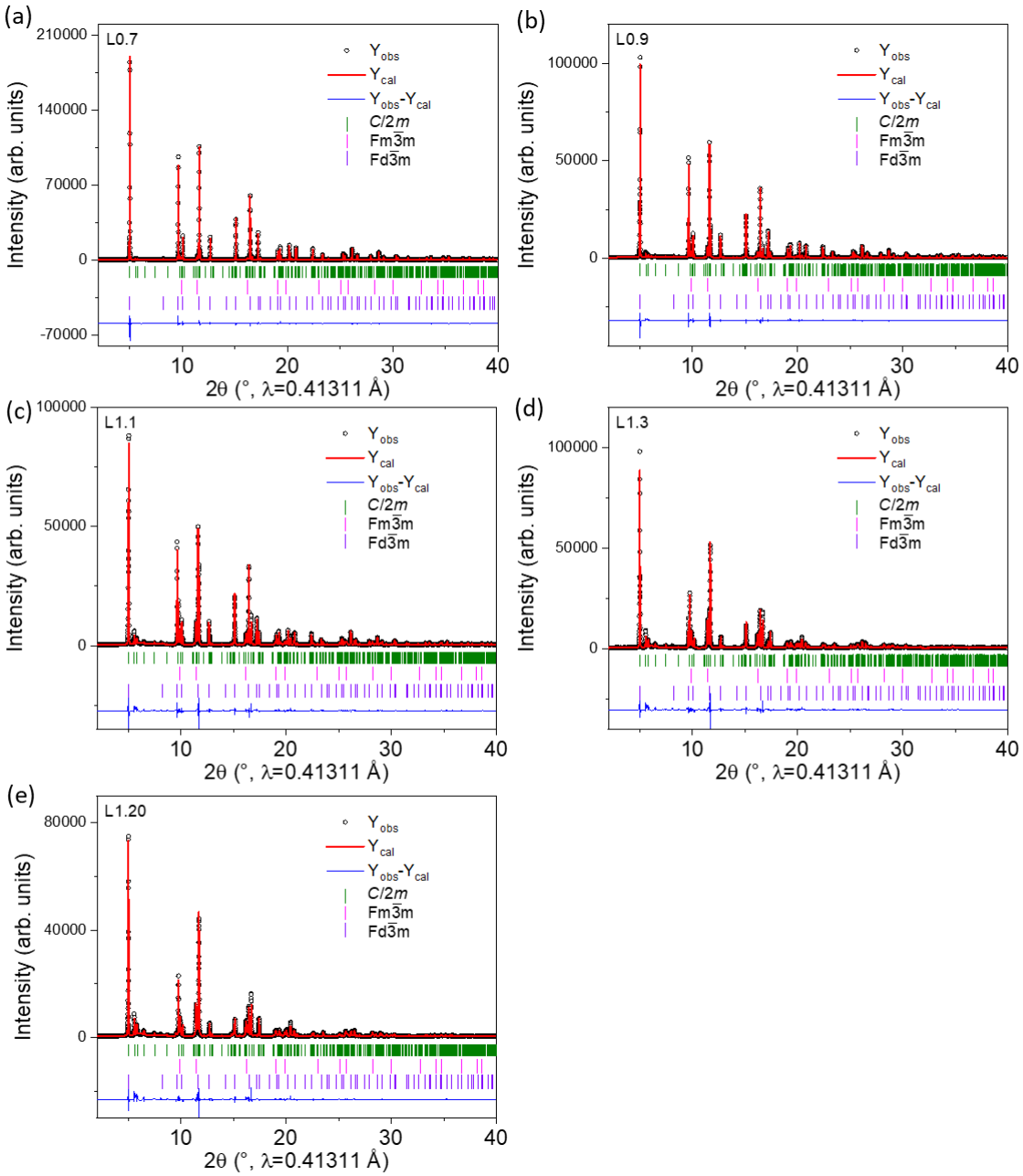

Figure 5.44 Rietveld refinement on synchrotron radiation diffraction patterns of (a) L0.40, (b) L0.56, (c) L0.72, (d) L0.88, (e) L1.04 and (f) L1.20.

From L0.40 to L1.20, all the specimens are assigned to a mixture of lithium-containing spinel phase ($Fd\,\bar{3}\,m$), lithium-containing rock-salt-type phase ($Fm\,\bar{3}\,m$) and lithium-containing monoclinic layered phase ($C2/m$) (see Figure 5.42). Rietveld refinements against SRD patterns were completed by using a mixed structure model, i.e. spinel$Li_{8a}[Ni_{0.5}Mn_{1.5}]_{16d}O_{4\ 32e}$, rock-salt-

type $[Li_x\ TM_{1-x}]_{4a,oct}O_{4b}$ and layered $Li_{oct}[Li_{0.2}Ni_{0.2}Mn_{0.6}]_{oct}O_2$, see Figure 5.44 and Table 5.8. With increasing lithium content, the weight fraction of the Li-containing spinel phase is successively reduced from ~ 100 % for L0.40 to ~ 5 % for L1.20, while the percentage of Li-rich layered phase and Li-containing rock-salt-type phase rises to ~ 82 % and ~ 12 % for L1.20, respectively. These results indicate that the spinel phase gradually transforms to the Li-rich layered phase accompanied by a production of a lithium-containing rock-salt-type phase. No clear variation in the lattice parameters is observed during phase transformation, illustrating a predominant two-phase transition mechanism. Provided that more lithium ions are inserted into the spinel $LiNi_{0.5}Mn_{1.5}O_4$ structure, the lithium ions and TM ions could migrate randomly to the remaining empty octahedra (16*c* position) and the other octahedra (16*d* site) to form a lithium-containing rock-salt-type structure $\{Li_{2x}TM_{2-2x}\}_{16c,oct}[Li_{2x}TM_{2-2x}]_{16d,oct}O_{4\ 32e}$ (i.e. $[Li_x\ TM_{1-x}]_{4a}O_{4b}$), in which the original spinel ccp oxygen framework is maintained.[114] The typical layered rhombohedral phase ($R\bar{3}m$) can be considered as a lithium-containing rock-salt-type derivative, where octahedrally coordinated lithium and transition metal cations ideally form alternating layers confined to the $(111)_r$ face of ccp oxygen lattice.[115]

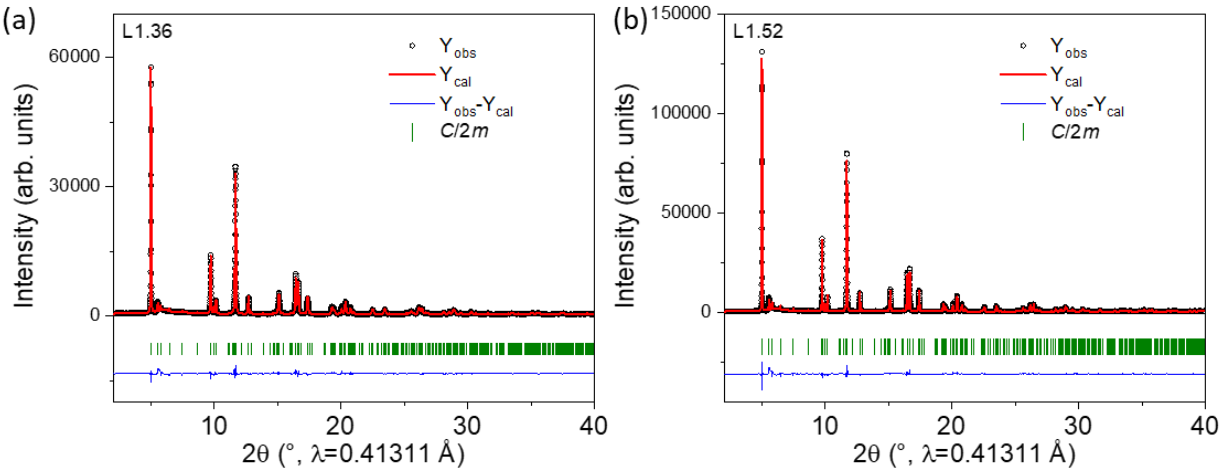

Figure 5.45 Rietveld refinement against synchrotron radiation diffraction patterns of (a) L1.36 and (b) L1.52.

When the added Li amount is higher than that of L1.20, both, Li-containing spinel and Li-containing rock-salt-type phases, have totally transformed into the Li-rich layered phase, as shown in Figure 5.42. Most of the reflections in SRD patterns for L1.36 and L1.52 can be indexed to a typical rhombohedral layered structure ($R\bar{3}m$), and a few weak reflections can be attributed to the superstructures corresponding to a monoclinic layered phase with the space group symmetry of

*C*2/*m*. Actually, both layered rhombohedral and monoclinic phases possess an O3-type structure. Unlikely the typical rhombohedral structure ($R\bar{3}m$), where the majority of TM ions are randomly positioned in the TM layer, a monoclinic layered structure (*C*2/*m*) could accommodate the excess lithium ions within the TM layer, thus forming the in-plane Li/TM ordering. Since all the reflections can be well indexed to a single monoclinic phase *C*2/*m*), Rietveld refinements were performed by using a layered monoclinic structural model $Li_{oct}[Li_{0.2}Ni_{0.2}Mn_{0.6}]_{oct}O_2$, see Figure 5.45 and Table 5.8. The reflections of L1.52 shift toward higher scattering angles compared to those of L1.36. The refinement results show that the lattice constants of L1.36 are slightly larger than those of L1.52, suggesting that the TM cations in L1.52 are further oxidized.

Table 5.8 Lattice parameters and structural parameters of the samples with provided different lithium contents.

Sample	Layered phase (*C*2/*m*)					Spinel phase ($Fd\bar{3}m$)		Rock-salt-type phase ($Fm\bar{3}m$)	
	a (Å)	*b* (Å)	*c* (Å)	beta	fraction (wt.%)	*a* (Å)	fraction (wt.%)	*a* (Å)	fraction (wt.%)
L0.00	/	/	/	/	/	8.4211	100 (0.49)	/	/
L0.08	/	/	/	/	/	8.3687	100 (0.32)	/	/
L0.24	/	/	/	/	/	8.2620	100 (0.36)	/	/
L0.40	/	/	/	/	/	8.1852	100 (0.64)	/	/
L0.56	4.9354	8.5449	5.0263	108.916	17.51 (0.27)	8.1712	77.63 (0.39)	4.1454	4.86 (0.19)
L0.72	4.9342	8.5459	5.0271	108.926	37.98 (0.42)	8.1705	54.47 (0.37)	4.1469	7.55 (0.26)
L0.88	4.9343	8.5464	5.0274	108.930	55.25 (0.58)	8.1693	34.57 (0.33)	4.1470	10.18 (0.34)
L1.04	4.9343	8.5465	5.0273	108.929	73.79 (0.78)	8.1693	13.41 (0.24)	4.1470	12.80 (0.42)
L1.20	4.9343	8.5464	5.0274	108.930	82.69 (0.84)	8.1693	5.04 (0.16)	4.1470	12.27 (0.46)
L1.36	4.9611	8.5651	5.0314	109.266	100 (0.55)	/	/	/	/
L1.52	4.9423	8.5541	5.0254	109.267	100 (0.56)	/	/	/	/

5.5.2 Electronic structure

XAS was used to investigate the changes of the bulk valence states of the transition metals in the samples (Figure 5.46). From L0.00 to L0.40, it is evident that the nickel valence state does not

change considerably, and remains around +2 by comparison with a nickel (II) oxide (NiO) standard. In contrast to nickel, the manganese valence state increases significantly, i.e. it changes from about +3 in L0.00 to +4 in L0.40. Correspondingly, the ionic radius of manganese ions reduces ($r_{Mn^{3+}}$ = 0.58 Å, $r_{Mn^{4+}}$ = 0.53 Å [116]), which is in good agreement with the contraction of the cubic spinel unit cell. Generally speaking, the manganese (III) ions can induce a tetragonal distortion in pure manganese spinel phase (Mn_3O_4) because of the Jahn-Teller effect.[117,118] Cubic manganese (III) oxide (Mn_2O_3) usually can be described as a corrundum structure (space group $Ia\bar{3}$) with hexagonal close packed (hcp) oxygen lattice. Interestingly, although manganese is dominantly in Mn (III) state, L0.00 possesses a cubic spinel phase as a consequence of the nickel-manganese solid solution. From L0.40 to L1.20, the valence state of both nickel and manganese for these samples remain the same as in L0.40, all are assigned to nickel (II) and manganese (IV), respectively. When the lithium amount is higher than L1.20, the oxidation state of manganese does not change pronouncedly, the nickel oxidation state in L1.52 is slightly increased, also in good agreement with a subtle shrinking of the unit cell and a continuous oxygen incorporation during lithium insertion into the layered structure.

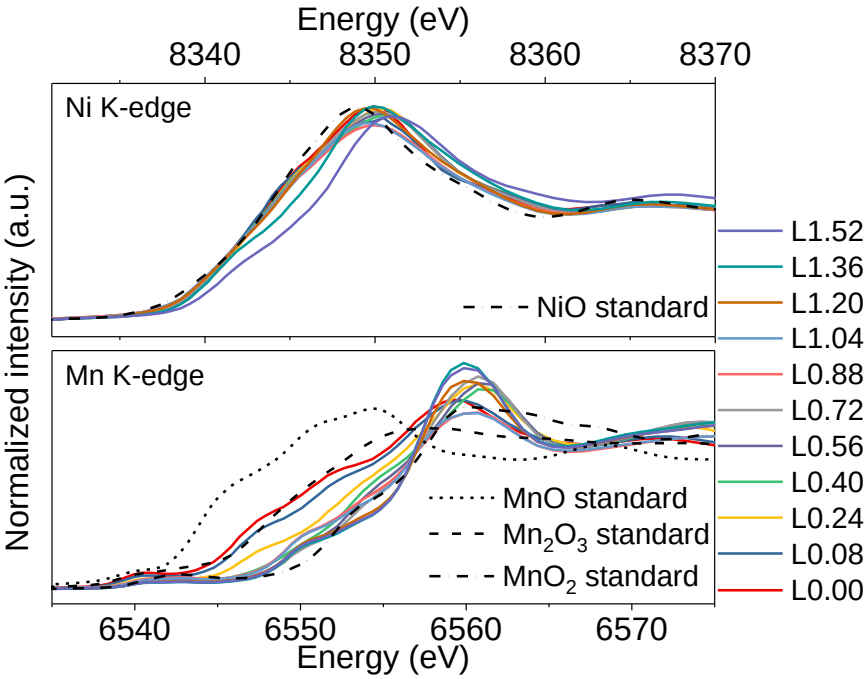

Figure 5.46 Normalised (a) Ni K-edge and (b) Mn K-edge XAS spectra for the samples (L0.00 to L1.52).

5.5.3 ^{7}Li MAS NMR analysis

^{7}Li MAS NMR was performed to understand the evolution of local environment of lithium ions in the prepared lithium insertion compounds (Figure 5.47). Each NMR spectrum was normalized with respect to the number of spectral acquisitions and the mass of specimens. The resonances observed at 3 ppm can be assigned to lithium in diamagnetic compounds such as lithium carbonate, the NMR resonances at 917 and 973 ppm correspond to lithium on tetrahedral potions (LiO_4) in the high-voltage spinel $LiNi_{0.5}Mn_{1.5}O_4$ [119]. The resonance at 741 ppm corresponds to lithium on octahedral positions (LiO_6) in the lithium layer in the typical layered NCM oxides.[119,120] The resonances observed at approximately 1302 and 1501 ppm correspond to lithium in the transition metal layer (octahedral coordination) typical for $Li[Li_{1/3}Mn_{2/3}]O_2$ phase.[119]

A broad NMR peak with a comparably large NMR shift appears in the samples from L0.00 to L0.40, indicating that lithium is inserted into the host spinel architecture with paramagnetic elements (lithium in lithium carbonate would cause a signal at about 3 ppm). In addition, the integral intensity of the resonance signal is rising and moving to continuously to the position of the resonances at 917 and 973 ppm with increasing lithium concentration, providing further evidence for lithium incorporation into the tetrahedral positions in the spinel structure. Such resonance shift is probably caused by an increase of the valence and spin states of manganese from low-spin Mn^{3+} (electronic configuration $3d^4$: $t_{2g}^4e_g^0$) to high-spin Mn^{4+} ($3d^3$: $t_{2g}^3e_g^0$) in spinel lithium insertion oxides [121]. Together, these results demonstrate that lithium insertion into the tetrahedral sites in the spinel structure would induce more TM cations to be located at the octahedral 16*d* sites. On the other hand, the nickel valence state keeps a constant value (Ni^{2+}, $3d^8$: $t_{2g}^6e_g^2$), while the manganese valence state increases gradually with increasing lithium content from L0.00 to L0.40. These results demonstrate that the oxygen anions are supposed to be absorbed from air atmosphere and/or lithium oxide into the host spinel structure to maintain electroneutrality, and to provide additional octahedral coordination sites for the moved TM cations and inserted Li ions. Overall, this region can be regarded as a ‘growth’ of the whole spinel crystals (see Figure 5.48).

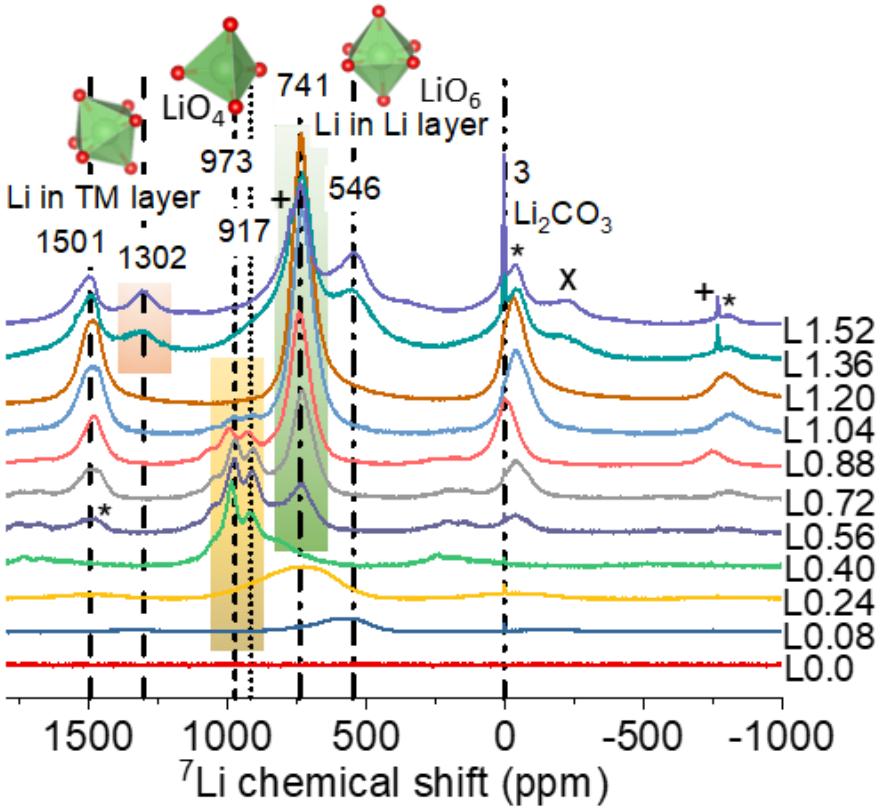

Figure 5.47 ^{7}Li MAS NMR spectra (spinning sidebands are marked with a plus, a cross and an asterisk) of the samples (L0.00 to L1.52).

From L0.40 to L1.20, intensity of NMR peaks found at 741 ppm increases significantly while the resonances at 917 ppm and 973 ppm decrease gradually, revealing that more and more lithium ions tend to be positioned at octahedral sites forming the Li-containing rock-salt-type/layered phase as lithium ions are further inserted into the host architecture. Due to the fact that the TM, both nickel and manganese, valence states do not change significantly from L0.40 to L1.20, the chemically induced phase transition from spinel to rock-salt-type/layered phase is supposed to be associated with an oxygen incorporation, atom rearrangement and surface reconstruction (accommodating more Li/O atoms).

When the lithium content (*x* value) is higher than 1.20, the new resonances at about 1302 and 1501 ppm are clearly observed, suggesting that the excess of lithium ions migrates to transition metal layer in the layered phase forming in-plane superlattice (see the superlattice reflections in Figure 5.45). Since the TM composition is constant within the rock-salt-type phase and the layered phase, as lithium and oxygen is inserted into the crystal structure, the equally distributed Li and

TM cations within the layers in the rock-salt-type structure separate into two different layers, i.e. a Li layer and a TM layer. Only few TM cations occupy the Li layer, while a large amount of lithium (around 20 %) occupies sites in the TM layer producing an in-plane Li/TM superstructure. As a result, lithium insertion into the layered structure is also supposed to be accompanied by an oxygen uptake and a 'growth' of the whole layered crystals.

5.5.4 Morphological changes

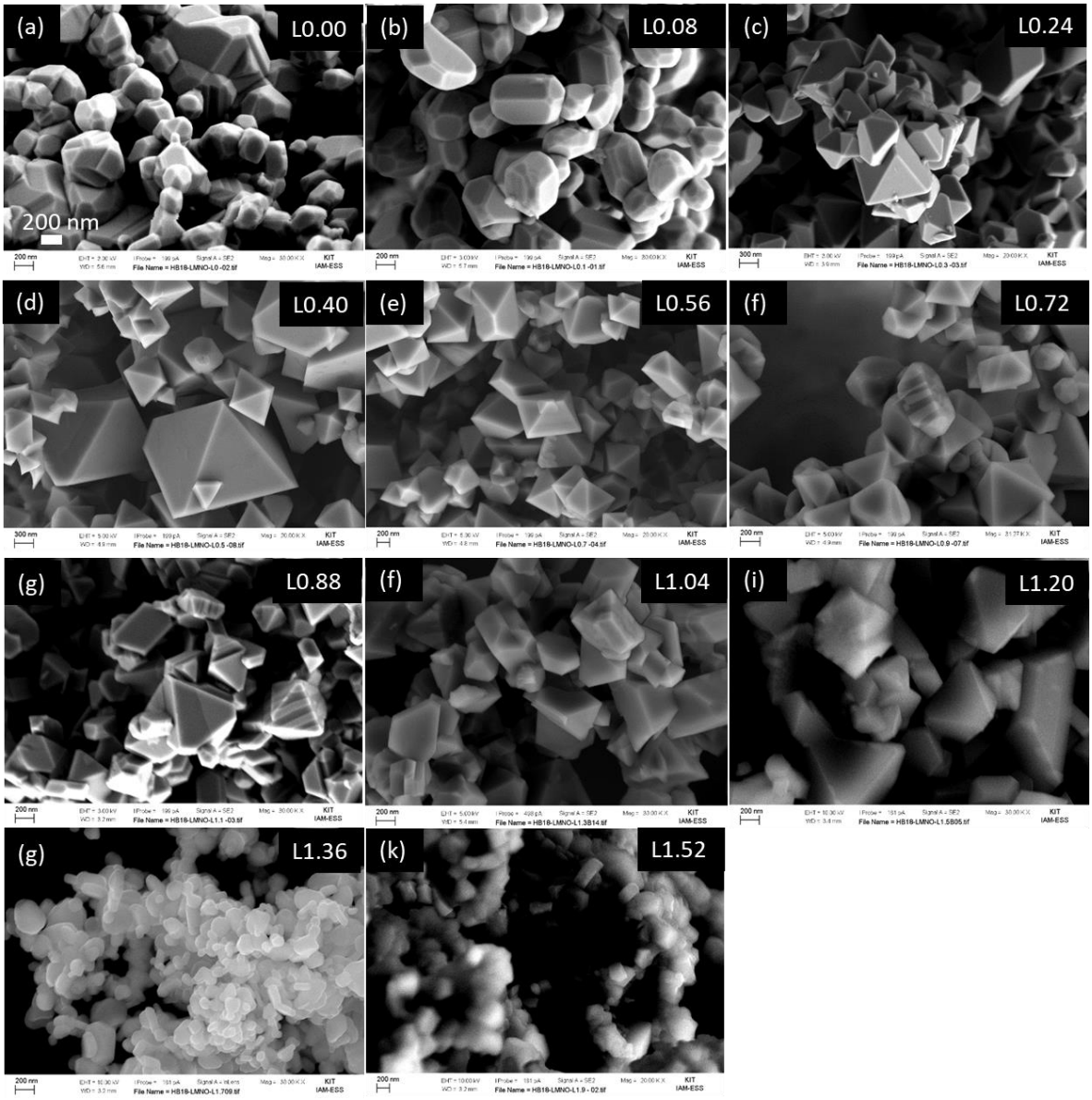

Figure 5.48 SEM images of the samples obtained by adding different amounts of lithium, the scale bar is 200 nm.

Figure 5.48 shows the morphological evolution of the samples with increase of the provided lithium concentration. Concerning L0.00, the particle with spinel structure has a polyhedral shape. When the Li content is increased to L0.40, these primary particles grow up to form an octahedron-like shape with pronounced edges and corners, revealing the growth of spinel crystals (see discussion above in section 5.5.3). From L0.40 to L1.20, the fine crystals tend to form the plate-like morphology, which agrees satisfactorily with the phase transition from cubic to layered structure. As Li concentration further increases to L1.52, the primary particle size of crystals has decreased and the plate-like particles (Figure 5.48(g)) have converted to spherical respectively polyhedral shape. These results provide an evidence for surface reconstruction to accommodate more lithium and oxygen atoms during thermal treatment.

5.6 High-temperature lithiation of spinel oxides

Previous research suggested that the migration of TM ions into tetrahedral sites would be beneficial for the stability of the delithiated layered structure.[11] Yang and co-workers proved that both Li-rich layered $Li_{1.2}Ni_{0.15}Co_{0.1}Mn_{0.55}O_2$ oxides and Li-containing spinel $LiNi_{0.5}Mn_{1.5}O_4$ cathodes at highly charged state experience a phase transition to Li-poor spinel phase (similar to L0.00 in section 5.5) accompanied by oxygen loss during heating.[122,123] It is therefore interesting to investigate how the structural evolution from spinel to Li-containing oxides occurs during synthesis (reverse direction).

In order to elucidate the Li/O insertion-induced structural evolution in $Li_xNi_{0.2}Mn_{0.6}O_y$ oxides, three different synthetic routes were used in this section, i.e. $Ni_{0.2}Mn_{0.6}O_{1.16-\delta}$ and Li_2CO_3 (n_{Li} : $n_{0.2Ni+0.6Mn}$ = 0.44), $Li_{0.4}Ni_{0.2}Mn_{0.6}O_{1.6-\delta}$ and Li_2CO_3 (n_{Li} : $n_{0.2Ni+0.6Mn}$ = 0.88) and $Ni_{0.2}Mn_{0.6}O_{1.16-\delta}$ and Li_2CO_3 (n_{Li} : $n_{0.2Ni+0.6Mn}$ = 1.32), respectively.

5.6.1 Formation of Li-containing spinel oxides

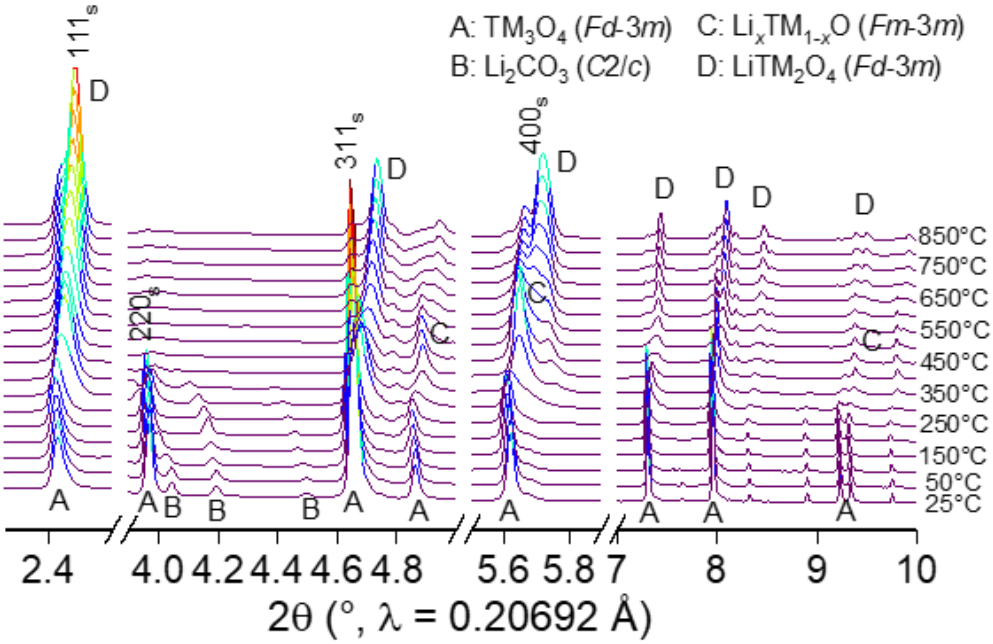

Figure 5.49 In situ high-temperature SRD patterns of a mixture of L0.00 and Li_2CO_3 during heating.

In this part, the Li-free spinel L0.00 ($Fd\bar{3}m$) was firstly mixed with a desired amount of Li_2CO_3 as starting materials for preparation of $LiNi_{0.5}Mn_{1.5}O_4$ oxides, as shown in Figure 5.49. The 220_s

reflection intensity is sensitive to the occupancy of TM ions located on tetrahedral sites. The intensity ratio of the 311_s to 111_s reflection is an indication for the degree of TM disorder between octahedral and tetrahedral sites in spinel structure, i.e. the ratio of $311_s/111_s$ intensity decreases with reducing the occupation of TM on the tetrahedral positions.[124] As the temperature increases to 550 °C, the intensity of the 220_s reflection at ~ 4.0° in the SRD diffraction pattern of the mixture is continuously reduced, together a the reduced intensity ratio of the $311_s/111_s$ reflections. The Rietveld refinements results (Figure 5.50(a & b)) show that the weight fraction of the Li-containing spinel and Li-containing rock-salt-type phases is increased, almost no spinel with TM on the tetrahedral sites is observed in the mixture heated to 550 °C. These results reveal that lithium ions could easily enter into the tetrahedral positions in the spinel structure, and push manganese cations to be positioned at octahedral 16*d* sites generating the more ordered lithium-containing spinel/rock-salt-type phase. Additionally, the high-temperature lithiation reaction at this stage promotes the decomposition of lithium carbonate, revealing that the spinel phase delivers a good reaction activity for lithiation during the synthesis process.

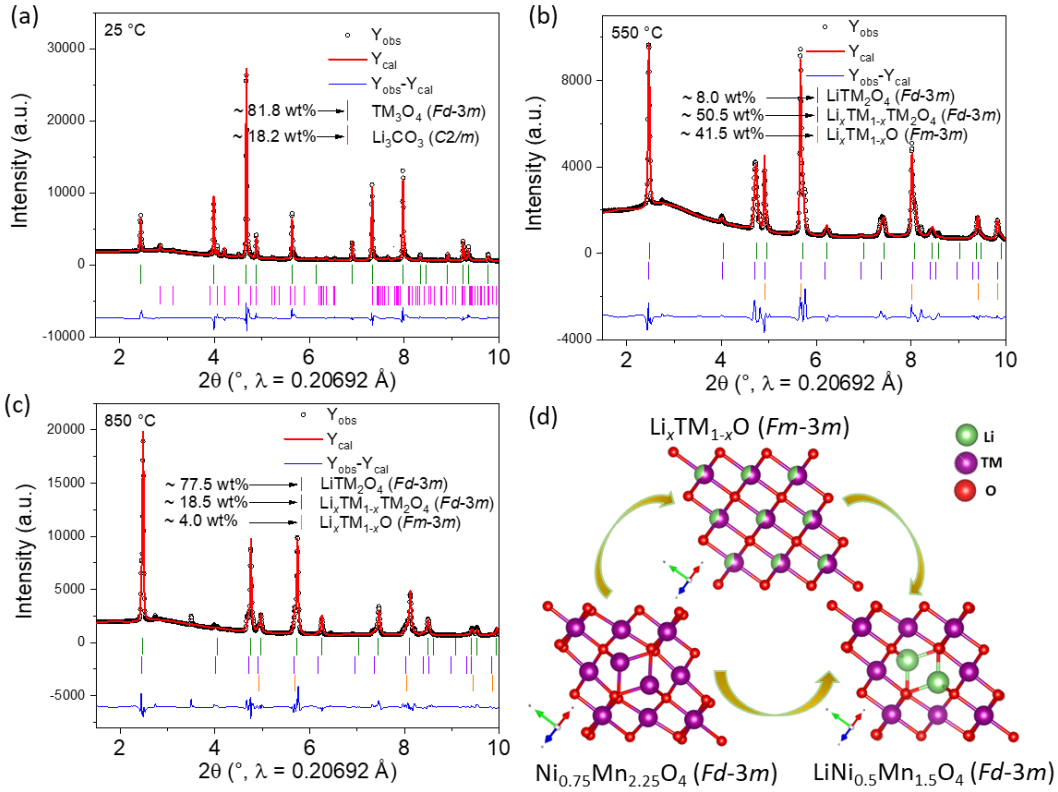

Figure 5.50 Rietveld refinement on SRD patterns of the mixture collected at (a) 25 °C, (b) 550 °C and (c) 850 °C; (d) an illustration of local structural evolution from Li-free spinel phase to Li-containing rock-salt-type/spinel phase.

As the temperature further increases to 850 °C, the Li-containing rock-salt-type phase gradually transforms to Li-containing spinel phase, implying that lithium ions have the tendency to occupy the tetrahedral positions only if a small amount of lithium is available during thermal treatment. Interestingly, the weak reflections of the mixture obtained at 850 °C can also be indexed to a cubic spinel phase ($Fd\bar{3}m$), Figure 5.49 and Figure 5.50(c), which might be attributed to the formation of Li-containing spinel phases with various lithium contents as lithium is incorporated into the crystal structure from the surface. During the process of lithium ion incorporation, the oxygen anions are supposed to be simultaneously inserted into spinel crystals to increase the manganese valance state and to provide additional metal coordination sites for both inserted Li ions and transferred TM cations. Based on the *in situ* high-temperature SRD results, a possible formation mechanism is proposed according to the following lithiation reaction:

$$\frac{2}{3}\underbrace{\mathrm{Mn_{tet}[Ni_{0.75}^{2+}Mn_{1.25}^{\sim 3+}]_{oct}O_4}}_{(Fd\bar{3}m)} + \frac{1}{2}\mathrm{Li_2CO_3} + \frac{5}{12}\mathrm{O_2}$$

$$\xrightarrow{\Delta} \underbrace{\mathrm{Li_{tet}[Ni_{0.5}^{2+}Mn_{1.5}^{4+}]_{oct}O_4}}_{Fd\bar{3}m} + \tfrac{1}{2}\mathrm{CO_2}\uparrow \qquad (5.6)$$

5.6.2 Formation of Li-rich layered oxides from Li-containing spinel oxides

Li-containing spinel L0.40 was mixed with a desired amount of Li_2CO_3 as starting materials for the synthesis of LLOs, as shown in Figure 5.51-5.52. When the temperature is higher than 500 °C, the layered phase with a monoclinic space group symmetry *C*2/*m* is successively produced from cubic spinel L0.40 according to the following reaction:

$$\frac{2}{5}\underbrace{\mathrm{Li_{tet}[Ni_{0.5}^{2+}Mn_{1.5}^{4+}]_{oct}O_4}}_{Fd\bar{3}\mathrm{m}} + \frac{2}{5}\mathrm{Li_2CO_3}$$

$$\xrightarrow{\Delta} \underbrace{\mathrm{Li_{oct}[Li_{0.2}Ni_{0.2}^{2+}Mn_{0.6}^{4+}]_{oct}O_2}}_{C2/m} + \tfrac{2}{5}\mathrm{CO_2}\uparrow \qquad (5.7)$$

In comparison with reaction (5.6) and (5.8), the lithiation reaction of Li-containing spinel phase composite and Li-source could have occurred at a relatively low temperature (~ 550 °C). This is probably due to the fact that the Li atoms already contained in the L0.40 can easily be displaced from their tetrahedral sites and therefore provide a low barrier for L0.40 to react with lithium and oxygen.

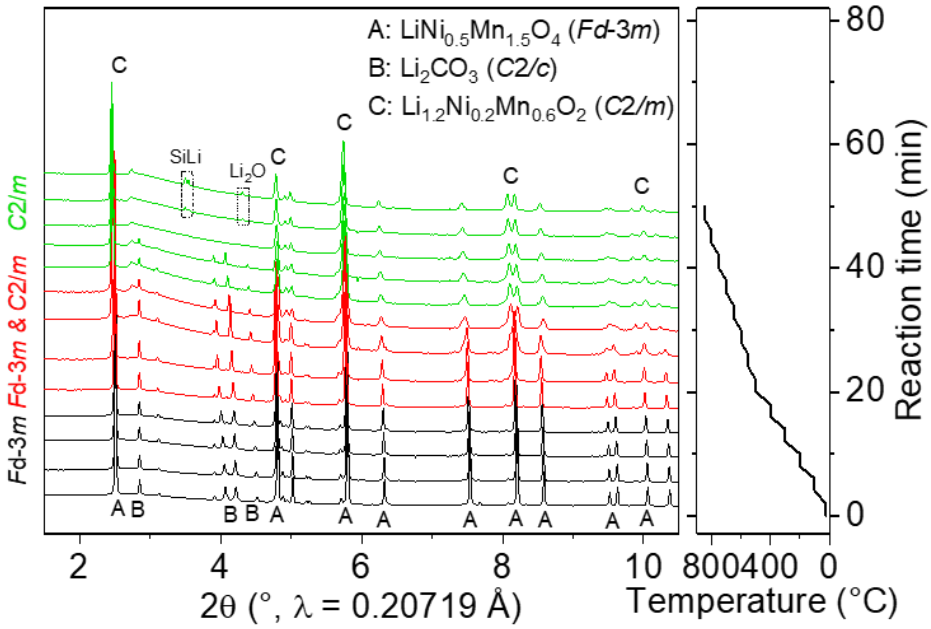

Figure 5.51 In situ high-temperature SRD patterns of a mixture of L0.40 and Li_2CO_3, and the heating temperature as a function of reaction time.

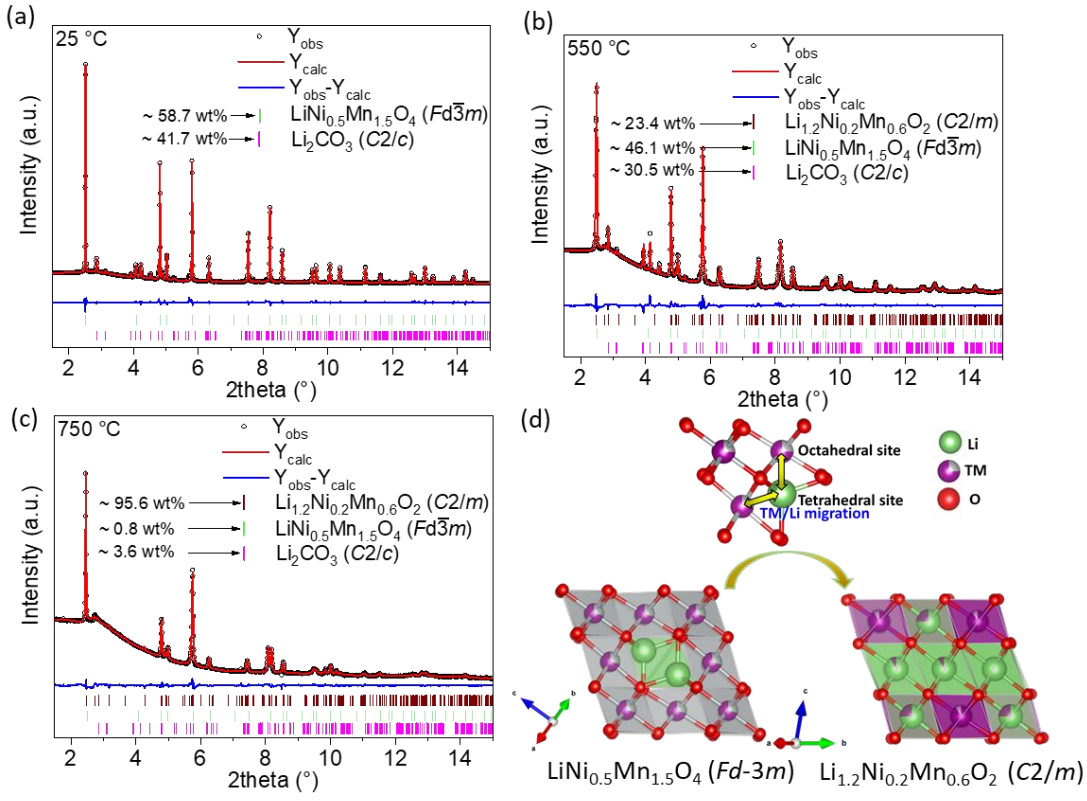

Figure 5.52 Rietveld refinement on synchrotron diffraction patterns of the sample collected at (a) 25 °C, (b) 550 °C and (c) 750 °C; (d) an illustration of local structural evolution from Li-containing spinel to Li-rich layered phase.

5.6.3 Formation of Li-rich layered oxides from Li-free spinel oxides

In order to understand the formation of Li-excess layered oxides from Li-free spinel phase, L0.00 together with a desired amount of Li_2CO_3 was used as raw materials for the synthesis of LLOs. During heating process, the Li-free spinel oxide rapidly transforms to the intermediate phases, i.e. over-lithiated Li_2TMO_2 phase ($P3m1$), Li-containing cubic ($Fd\bar{3}m$) and tetragonal ($I4_1/amd$) phases, and Li-containing rock-salt-type phase ($Fm\bar{3}m$), at an early stage of the lithiation, see Figure 5.53 & 5.55 and Table 5.9. The formation of over-lithiated layered phase ($P3m1$) can be assigned to the high lithium content at the surface of the Li-free spinel particles, revealing the production of Li-rich surface phases and Li-poor phases at the inner part of the crystallites during high-temperature lithiation reaction. The multiple intermediate phases convert into the lithium-containing rock-salt-type phase at about 800 °C and finally transform to the lithium-rich layered phase with an increase of calcination temperature at around 850 °C, implying that the lithiation reaction is rate-limited by the high activation barrier of phase transformation from lithium-containing rock-salt-type phase to lithium-rich layered phase.

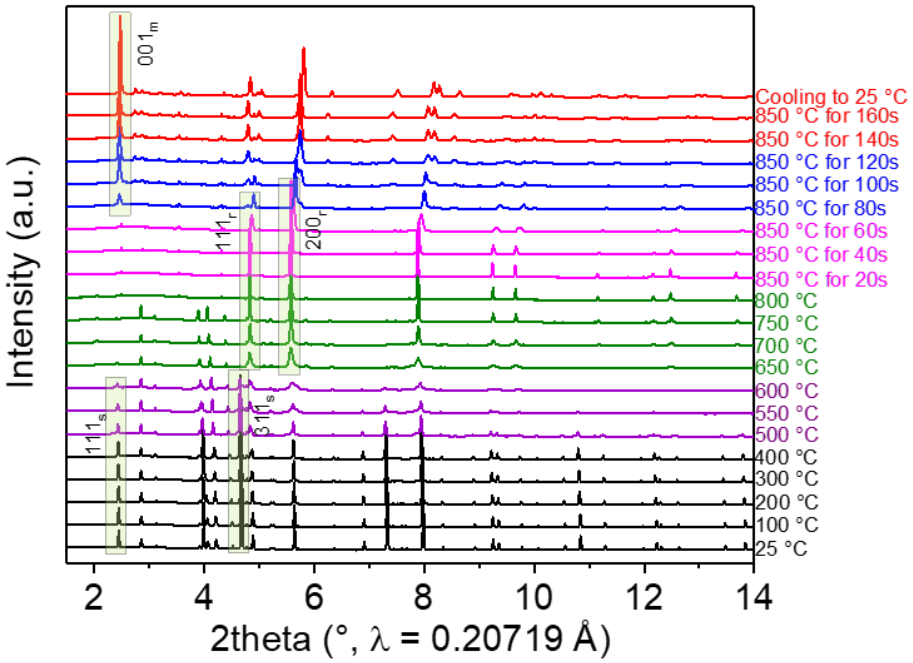

Figure 5.53 Time-resolved high-temperature synchrotron radiation diffraction patterns of a mixture of L0.00 and Li_2CO_3, and the heating temperature as a function of reaction time.

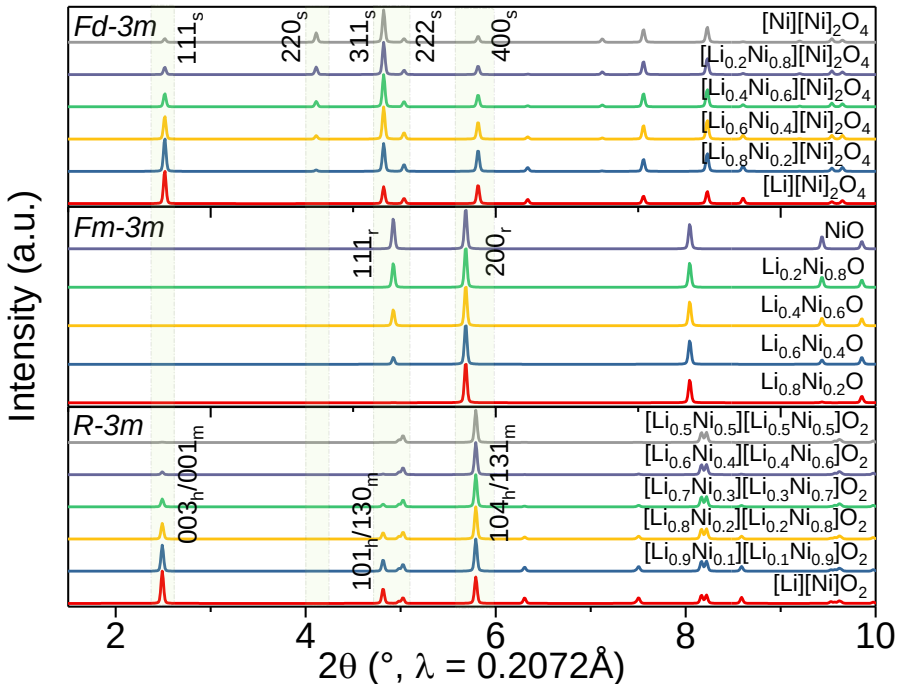

Figure 5.54 Simulation results of X-ray powder diffraction patterns of spinel $[Li_xNi_{1-x}][Ni_2]O_4$, rock-salt-type $[Li_xNi_{1-x}]O$ phase, and layered hexagonal $[Li_xNi_{1-x}][Ni_xLi_{1-x}]O_2$. s, r, h and m represent spinel, rock-salt-type, hexagonal and/or monoclinic layered phase, respectively.

Specifically, the $(200)_r$ plane of rock-salt-type structure can be considered as a non-polar cleavage plane. On the contrary, the $(111)_r$ plane is polar and unstable.[125,126] The XRD simulation results show (Figure 5.54) that the 200_r reflection is the strongest in the ionic rock-salt-type $[Li_x\ Ni_{1-x}]_{oct}O$ oxide, while the intensity of the 111_r reflection is decreased as lithium gradually inserts into the rock-salt-type architecture. Therefore, the relative intensity of the 111_r and 200_r reflections (I_{111}/I_{200}) can be used as a means to estimate the lithium concentration in the lithium-containing rock-salt-type phase. As shown in Figure 5.53 and Table 5.9, I_{111}/I_{200} ratio decreases successively with increased lithiation temperature and time, implying that lithium ions are progressively incorporated into the rock-salt-type structure. The reflections corresponding to the cubic rock-salt-type phase initially move toward lower 2-theta angles and clearly shift toward higher 2-theta angles as the lithiation proceeds. This probably can be attributed to the transition from disordered [Li/TM]-O-[Li/TM] chains in the lithium-containing rock-salt-type phase to more ordered Li-O-[Li/TM] linkages in the monoclinic layered phase. Very importantly, after cooling to room temperature, the maintained layered structure indicates that lithium and oxygen

incorporation into spinel/rock-salt-type structure produces a new and stable layered phase according to the following lithiation reaction:

$$\frac{4}{15}\underbrace{\mathrm{Mn_{tet}[Ni^{2+}_{0.75}Mn^{\sim 3+}_{1.25}]_{oct}O_4}}_{(Fd\bar{3}m)} + \frac{3}{5}\mathrm{Li_2CO_3} + \frac{1}{6}\mathrm{O_2} \xrightarrow{\Delta} \underbrace{\mathrm{[Li]_{oct}[Li_{0.2}Ni^{2+}_{0.2}Mn^{4+}_{0.6}]_{oct}O_2}}_{C2/m} + \frac{3}{5}\mathrm{CO_2}\uparrow \quad (5.8)$$

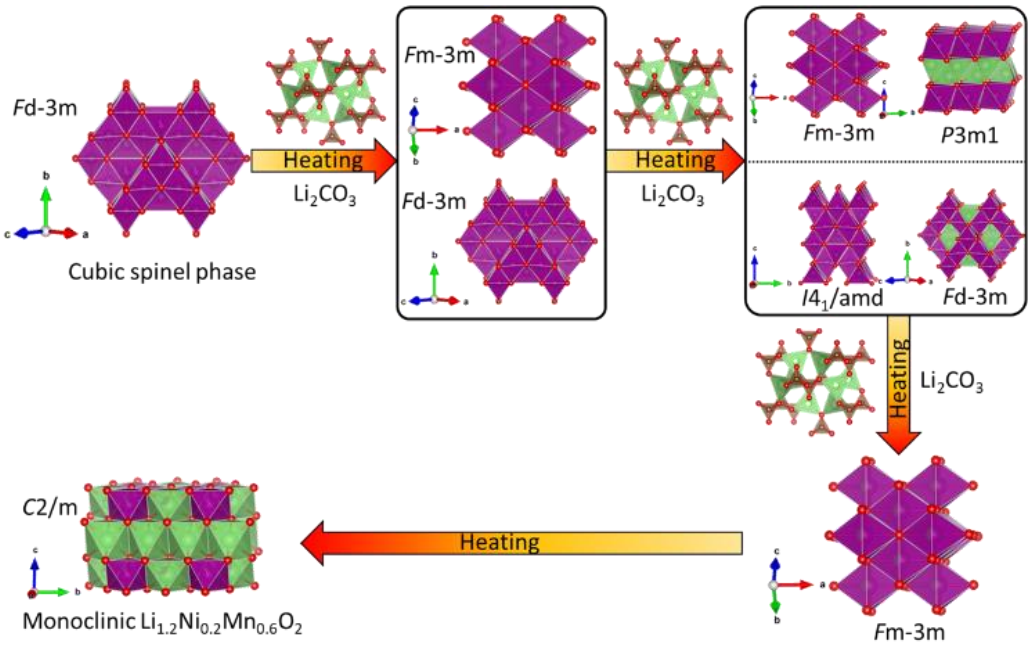

Figure 5.55 Schematic illustration for the phase transition of L0.0 and Li_2CO_3 during high-temperature lithiation reaction.

That is to say, as lithium ions are inserted into the host spinel matrix, TM atoms occupying the tetrahedral and/or octahedral sites in the spinel structure transfer to the TM layers forming a monoclinic layered phase. Meanwhile lithium ions move to both Li and TM layers in the honeycomb ordered monoclinic-layered structure. Because the spinel, rock-salt-type, and layered phases have a coherent ccp oxygen lattice, oxygen anions are supposed to be only absorbed at the oxygen surface lattice, thus supplying the indispensable nutrients for crystal growth / recrystallization. The synthesis of LLOs is frustrated by the phase transition from Li-containing rock-salt-type to monoclinic layered phase. What makes these high-temperature lithiation mechanisms interesting is that they can not only unveil the original formation of lithium insertion oxides during the synthesis process (Li/O incorporation), but offer new insights into the structural degradation of cathode materials during prolonged cycling at room temperature. For instance,

fatigue mechanism of LLOs during the mid-to long-term cycling can be considered as a kind of partially inverse formation of LLOs (Li/O loss) see Figure 5.56.

Table 5.9 Phase constitution of the mixture of L0.0 and Li_2CO_3 at different temperatures.

SRD pattern at different temperatures	Phase fraction (wt.%)						
	Li_2CO_3 ($C2/m$)	$Li_xTM_{1-x}TM_2O_4$ ($I4_1/amd$)	$Li_xTM_{1-x}TM_2O_4$ ($Fd\bar{3}m$)	Li_2TMO_3 ($C2/m$)	Li_2TMO_2 ($P3m1$)	$Li_xTM_{1-x}O$ ($Fm\bar{3}m$)	I_{111r}/I_{200r}
25 ℃	48.26 (0.90)	/	51.74 (0.49)	/	/	/	
100 ℃	49.04 (0.91)	/	50.96 (0.48)	/	/	/	
200 ℃	50.80 (0.94)	/	49.20(0.48)	/	/	/	
300 ℃	48.15 (0.98)	/	51.85 (0.52)	/	/	/	
400 ℃	50.76 (1.04)	/	49.24 (0.53)	/	/	/	
500 ℃	52.88 (1.39)	/	35.79 (0.61)	/	/	11.33 (0.96)	0.68
550 ℃	53.46 (1.68)	/	29.68 (0.76)	/	/	16.87 (0.93)	0.74
600 ℃	46.45 (1.51)	11.80 (0.90)	10.23 (0.47)	/	/	31.51 (1.42)	0.46
650 ℃	32.38 (0.85)	8.80 (0.92)	/	/	5.06 (0.67)	53.76 (1.54)	0.43
700 ℃	32.29 (0.83)	4.72 (0.43)	/	/	4.25 (1.24)	58.74 (1.38)	0.45
750 ℃	48.97 (1.20)	2.54 (0.25)	/	/	3.28 (0.42)	45.21 (0.84)	0.39
800 ℃	/	/	/	3.37 (0.05)	2.93 (0.43)	89.42 (1.77)	0.36
850 ℃ for 20s	/	/	/	0.18 (0.19)	/	93.53 (1.27)	0.35
850 ℃ for 40s	/	/	/	0.19 (0.23)	/	92.80 (1.57)	0.34
850 ℃ for 60s	/	/	/	0.74 (0.19)	/	91.72 (1.33)	0.30
850 ℃ for 80s	/	/	/	28.08 (0.69)	/	65.08 (1.13)	0.28
850 ℃ for 100s	/	/	/	56.50 (1.04)	/	37.13 (0.93)	0.29
850 ℃ for 120s	/	/	4.06 (0.55)	82.92 (1.44)	/	4.72(0.25)	0.31
850 ℃ for 140s	/	/	2.76 (0.38)	85.97 (1.19)	/	2.71 (0.23)	
850 ℃ for 160s	/	/	/	90.88 (1.00)	/	/	

Note: the impurity of Li_2SiO_3 in the sample obtained at above 800 ℃ was not accounted in this table.

5.7 Conclusions

Combining all the results above, this work provides valuable information about the correlation between formation and degradation of lithium-rich layered cathode materials. From the results on the synthesis of thermostable lithium insertion compounds, it is found that the production of a spinel/rock-salt-type/layered heterostructure is intimately tied to the available amount of lithium and oxygen, see Figure 5.56.

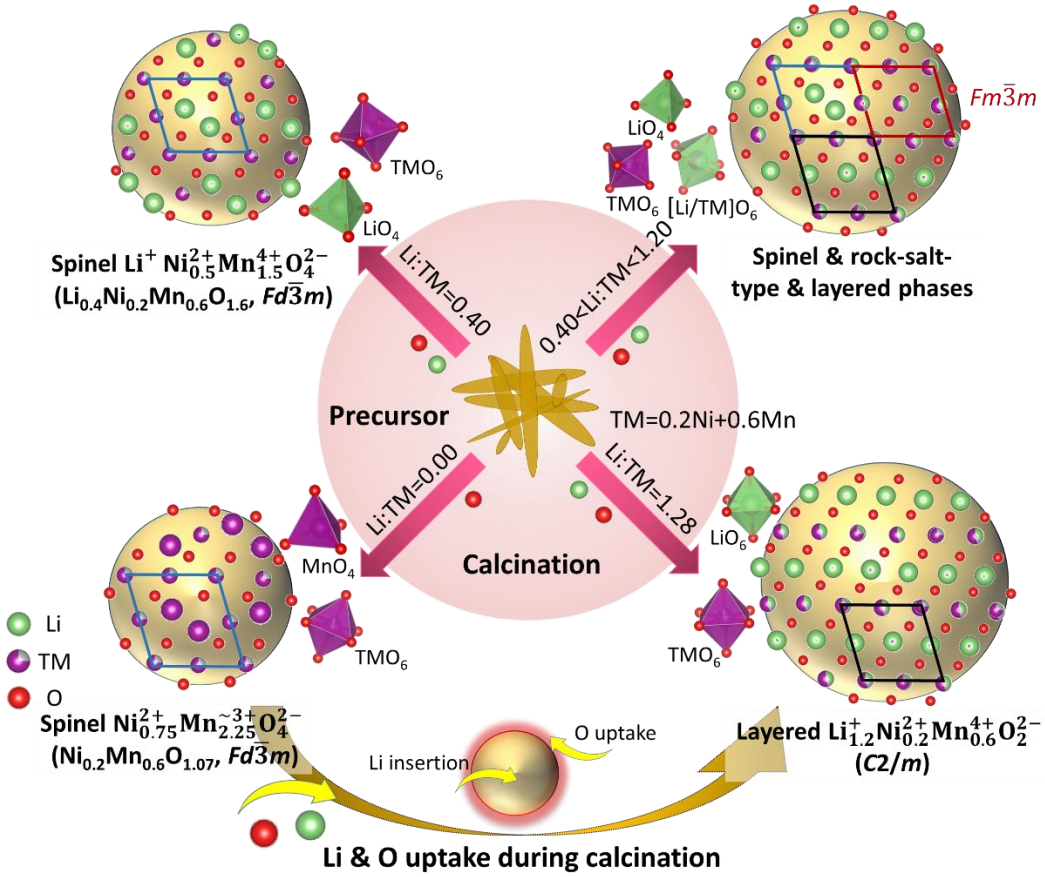

Figure 5.56 Schematic diagram of lithium- and oxygen-driven structural, electrical and thermodynamic complexity in $Li_xNi_{0.2}Mn_{0.6}O_y$ systems, revealing the possible formation mechanism of high-energy lithium-excess layered oxides.

The LLOs are stable only when a large amount of oxygen and lithium is inserted into the cubic spinel/rock-salt-type host structure, while at a low contents of them, the rock-salt-type and/or spinel phase become thermodynamically stable phases. The highly delithiated Mn-rich cathode materials with ccp oxygen lattice has the tendency to produce the Li-free spinel phase, accompanied by the reduction of manganese (IV) and the manganese migration into the tetrahedral

positions for facilitating stability of the structure. This process is supposed to be caused by oxygen release from ccp oxygen lattice during heating. The covalent bonding of nickel (II) is stronger in octahedral coordination of $Li_x\ Ni_{0.2}Mn_{0.6}O_y$ $(0.40 \leq x \leq 1.36)$ when compared with manganese (IV). However, in the over-lithiated oxides ($x > 1.36$), the stability of manganese (IV) is higher than that of nickel (II), i.e. nickel (II) is oxidized before manganese (IV).

An effective and practical technology, a hydroxide coprecipitation method followed by a microwave annealing process, for large-scale synthesis of Co-free LLOs is developed. With an increase in microwave-heating temperature, lithium and oxygen gradually enters into the spinel host framework formed from the precursor, thus continuously causing the formation of a rock-salt-type phase ($Fm\bar{3}m$) and finally resulting in the formation of a layered phase ($C2/m$). Heterogeneity and surface reconstruction along with the coherent structure of layered and spinel/rock-salt-type phases are clearly observed on a single crystallite/particle level, providing direct evidence for the localized nature of the phase transition mechanism.

The phase transformation detected by *in situ* high-temperature SRD reveals that the lithiation during synthesis of Li-containing oxides is found to be a surface-bulk-limited reaction. Hence, this synthetic process has a great impact on the phase composition, morphology, particle size, crystallinity and porosity of the prepared cathode materials, which have a pronounced effect on their ionic and electronic conductivities and thus electrochemical performances.

The rate-determining step of lithiation during synthesis is the transformation from Li-containing rock-salt-type structure to monoclinic layered structure. The LLO cathode materials can be generated during preparation as a result of competition between Li/O incorporation and Li/O loss. Since all the Li-containing spinel, Li-containing rock-salt-type and Li-rich layered phases have a similar ccp oxygen lattice, oxygen atom insertion into the oxygen surface lattice is the only possibility during high-temperature lithiation, thus providing the essential elements for the formation of LLOs.

A combination of HAADF-STEM, SRD and NPD techniques confirms that the prepared $Li[Li_{0.2}Ni_{0.2}Mn_{0.6}]O_2$ cathode consists of a single monoclinic phase with ultra-thin spinel surface. Cathodes made of the prepared LLOs exhibit an outstanding electrochemical performance, demonstrating a discharge capacity of 293 mAh g^{-1} at 0.1 C and 171 mAh g^{-1} at 10 C. The electrochemical characterizations show that the performance of cathode materials has a close relationship with the optimized phase composition and the appropriate synthetic conditions.

From a synthetic chemist's perspective, it can be concluded that the undesired transformation/degradation from layered to spinel/rock-salt-type phase during cycling is strongly related to the lithium-depleted state of charge, i.e. only at relatively low charged states, the layered phase can be considered as stable.

6 Summary and recommendations for future work

In order to develop high-energy cathode materials with enhanced performance, the aim of this study is to unravel the formation mechanism of Li-rich layered $Li[Li_{0.2}Ni_{0.2}Mn_{0.6}]O_2$ during synthesis. The incorporation of lithium and oxygen into the host matrix architecture during the formation of lithium-excess layered oxide cathode materials (LLOs) has been experimentally proved by this work. The present study not only provides the rate-limited steps and prerequisites for the synthesis of lithium insertion compounds with good electrochemical performance, but also help to better understand the degradation mechanism of these cathode materials during prolonged cycling.

The uncovered lithiation mechanism presents the original formation of LLOs in each step, which offers significant and valuable information for industrial operation, and contributes to a comprehensive understanding of the intrinsic correlation between the preparation, structure and electrochemical performance in the materials.

Unfortunately, the chemical distribution, TM oxidation state and crystal phase of the heterostructured lithium insertion oxides on a single crystallite particle level are still not clear to date. The recommendations for future work is to spatially resolve the Ni and Mn distribution and correlate them with its local chemical state and also the crystalline phases present in the crystallites. This will help to understand whether the TM oxidation state is linked to the elemental heterogeneity and crystallographic structure.

Bibliography

[1] P. Gibot, M. Casas-Cabanas, L. Laffont, S. Levasseur, P. Carlach, S. Hamelet, J.-M. Tarascon, C. Masquelier, *Nat. Mater.* **2008**, *7*, 741.

[2] Y.-Y. Hu, Z. Liu, K.-W. Nam, O. J. Borkiewicz, J. Cheng, X. Hua, M. T. Dunstan, X. Yu, K. M. Wiaderek, L.-S. Du, K. W. Chapman, P. J. Chupas, X.-Q. Yang, C. P. Grey, *Nat. Mater.* **2013**, *12*, 1130.

[3] K. Kang, Y. S. Meng, J. Bréger, C. P. Grey, G. Ceder, *Science.* **2006**, *311*, 977.

[4] R. Malik, F. Zhou, G. Ceder, *Nat. Mater.* **2011**, *10*, 587.

[5] W. Hua, J. Zhang, Z. Zheng, W. Liu, X. Peng, X. D. Guo, B. Zhong, Y. J. Wang, X. Wang, *Dalt. Trans* **2014**, *43*, 14824.

[6] A. K. Shukla, Q. M. Ramasse, C. Ophus, H. Duncan, F. Hage, G. Chen, *Nat. Commun.* **2015**, *6*, 8711.

[7] A. Singer, S. Hy, M. Zhang, D. Cela, C. Fang, B. Qiu, Y. Xia, Z. Liu, A. Ulvestad, N. Hua, J. Wingert, H. Liu, M. Sprung, A. V. Zozulya, E. Maxey, R. Harder, Y. S. Meng, O. G. Shpyrko, *Nat. Energy* **2018**, DOI 10.1038/s41560-018-0184-2.

[8] C. Delmas, M. Maccario, L. Croguennec, F. Le Cras, F. Weill, *Nat Mater* **2008**, *7*, 665.

[9] Y. J. Lee, H. Yi, W.-J. Kim, K. Kang, D. S. Yun, M. S. Strano, G. Ceder, A. M. Belcher, *Science.* **2009**, *324*, 1051.

[10] D. H. Seo, J. Lee, A. Urban, R. Malik, S. Kang, G. Ceder, *Nat. Chem.* **2016**, *8*, 692.

[11] M. Sathiya, A. M. Abakumov, D. Foix, G. Rousse, K. Ramesha, M. Saubanère, M. L. Doublet, H. Vezin, C. P. Laisa, A. S. Prakash, D. Gonbeau, G. VanTendeloo, J.-M. Tarascon, *Nat. Mater.* **2015**, *14*, 230.

[12] G. Assat, J. M. Tarascon, *Nat. Energy* **2018**, *3*, 373.

[13] K. Luo, M. R. Roberts, R. Hao, N. Guerrini, D. M. Pickup, Y. S. Liu, K. Edström, J. Guo, A. V. Chadwick, L. C. Duda, P. G. Bruce, *Nat. Chem.* **2016**, *8*, 684.

[14] S. Hy, F. Felix, J. Rick, W. N. Su, B. J. Hwang, *J. Am. Chem. Soc.* **2014**, *136*, 999.

[15] B. Ravel, M. Newville, *J. Synchrotron Radiat.* **2005**, *12*, 537.

[16] E. Lee, K. A. Persson, *Adv. Energy Mater.* **2014**, *4*, 1.

[17] D. Mohanty, J. Li, D. P. Abraham, A. Huq, E. A. Payzant, D. L. Wood, C. Daniel, *Chem.*

Mater. **2014**, *26*, 6272.

[18] Y. Pei, Q. Chen, Y. C. Xiao, L. Liu, C. Y. Xu, L. Zhen, G. Henkelman, G. Cao, *Nano Energy* **2017**, *40*, 566.

[19] A. Lundblad, B. Bergman, *Solid State Ionics* **1997**, *96*, 173.

[20] H. Gerischer, *Zeitschrift für Phys. Chemie* **1961**, *29*, 287.

[21] C. E. Holland, J. W. Weidner, R. a. Dougal, R. E. White, *J. Power Sources* **2002**, *109*, 32.

[22] W. B. Hua, X. D. Guo, Z. Zheng, Y. J. Wang, B. H. Zhong, B. Fang, J. Z. Wang, S. L. Chou, H. Liu, *J. Power Sources* **2015**, *275*, 200.

[23] B. Nykvist, M. Nilsson, *Nat. Clim. Chang.* **2015**, *5*, 329.

[24] D. Chung, E. Elgqvist, S. Santhanagopalan, *Automotive Lithium-Ion Cell Manufacturing: Regional Cost Structures and Supply Chain Considerations*, Clean Energy Manufacturing Analysis Center (CEMAC), **2016**.

[25] K. Saravanan, P. Balaya, M. V. Reddy, B. V. R. Chowdari, J. J. Vittal, *Energy Environ. Sci.* **2010**, *3*, 457.

[26] N. Ohmer, B. Fenk, D. Samuelis, C.-C. Chen, J. Maier, M. Weigand, E. Goering, G. Schütz, *Nat. Commun.* **2015**, *6*, 6045.

[27] T. Ohzuku, Y. Makimura, *Chem. Lett.* **2001**, *2*, 744.

[28] H. Chen, C. P. Grey, *Adv. Mater.* **2008**, *20*, 2206.

[29] Y. Deng, Y. Zhou, Z. Shi, X. Zhou, X. Quan, G. Chen, *J. Mater. Chem. A* **2013**, *1*, 8170.

[30] W. B. Hua, S. N. Wang, X. D. Guo, S. L. Chou, K. Yin, B. H. Zhong, S. X. Dou, *Electrochim. Acta* **2015**, *186*, 253.

[31] E. Zhao, L. Fang, M. Chen, D. Chen, Q. Huang, Z. Hu, Q. Yan, M. Wu, X. Xiao, *J. Mater. Chem. A* **2017**, *5*, 1679.

[32] S.-H. Park, H.-S. Shin, S.-T. Myung, C. S. Yoon, K. Amine, Y.-K. Sun, *Chem. Mater.* **2005**, *17*, 6.

[33] J. Reed, G. Ceder, *Chem. Rev.* **2004**, *104*, 4513.

[34] J. Hong, H. Gwon, S.-K. Jung, K. Ku, K. Kang, *J. Electrochem. Soc.* **2015**, *162*, A2447.

[35] N. Yabuuchi, K. Kubota, Y. Aoki, S. Komaba, *J. Phys. Chem. C* **2016**, *120*, 875.

[36] C.-H. Shen, S.-Y. Shen, F. Fu, C.-G. Shi, H.-Y. Zhang, M. J. Pierre, H. Su, Q. Wang, B.-B. Xu, L. Huang, J.-T. Li, S.-G. Sun, *J. Mater. Chem. A* **2015**, *3*, 12220.

[37] A. Devaraj, M. Gu, R. Colby, P. Yan, C. M. Wang, J. M. Zheng, J. Xiao, A. Genc, J. G.

Zhang, I. Belharouak, D. Wang, K. Amine, S. Thevuthasan, *Nat. Commun.* **2015**, *6*, 8014.

[38] D. L. Ye, L. Z. Wang, *Mater. Technol. Adv. Funct. Mater.* **2014**, *29*, A59.

[39] W. Wei, L. Chen, A. Pan, D. G. Ivey, *Nano Energy* **2016**, *30*, 580.

[40] S. Kim, W. Cho, X. Zhang, Y. Oshima, J. W. Choi, *Nat. Commun.* **2016**, *7*, 13598.

[41] M. Sathiya, G. Rousse, K. Ramesha, C. P. Laisa, H. Vezin, M. T. Sougrati, M.-L. Doublet, D. Foix, D. Gonbeau, W. Walker, A. S. Prakash, M. Ben Hassine, L. Dupont, J.-M. Tarascon, *Nat. Mater.* **2013**, *12*, 827.

[42] D. Seo, J. Lee, A. Urban, R. Malik, S. Kang, *Nat. Chem.* **2016**, 1.

[43] J. Zheng, P. Xu, M. Gu, J. Xiao, N. D. Browning, P. Yan, C. Wang, J. G. Zhang, *Chem. Mater.* **2015**, *27*, 1381.

[44] M. Gu, I. Belharouak, J. Zheng, H. Wu, J. Xiao, A. Genc, K. Amine, S. Thevuthasan, D. R. Baer, J. G. Zhang, N. D. Browning, J. Liu, C. Wang, *ACS Nano* **2013**, *7*, 760.

[45] D. Mohanty, S. Kalnaus, R. A. Meisner, K. J. Rhodes, J. Li, E. A. Payzant, D. L. Wood, C. Daniel, *J. Power Sources* **2013**, *229*, 239.

[46] K. Luo, M. R. Roberts, N. Guerrini, N. Tapia-Ruiz, R. Hao, F. Massel, D. M. Pickup, S. Ramos, Y. S. Liu, J. Guo, A. V. Chadwick, L. C. Duda, P. G. Bruce, *J. Am. Chem. Soc.* **2016**, *138*, 11211.

[47] M. Lee, S. Lee, P. Oh, Y. Kim, J. Cho, *Nano Lett.* **2014**, *14*, 993−999.

[48] A. Manthiram, K. Chemelewski, E.-S. Lee, *Energy Environ. Sci.* **2014**, *7*, 1339.

[49] X. Gao, Y. H. Ikuhara, C. A. J. Fisher, H. Moriwake, A. Kuwabara, H. Oki, K. Kohama, R. Yoshida, R. Huang, Y. Ikuhara, *Adv. Mater. Interfaces* **2014**, *1*, 1400143.

[50] J. Rana, S. Glatthaar, H. Gesswein, N. Sharma, J. R. Binder, R. Chernikov, G. Schumacher, J. Banhart, *J. Power Sources* **2014**, *255*, 439.

[51] N. Ortiz-Vitoriano, N. E. Drewett, E. Gonzalo, T. Rojo, *Energy Environ. Sci.* **2017**, *10*, 1051.

[52] J. Xiao, X. Chen, P. V. Sushko, M. L. Sushko, L. Kovarik, J. Feng, Z. Deng, J. Zheng, G. L. Graff, Z. Nie, D. Choi, J. Liu, J. G. Zhang, M. S. Whittingham, *Adv. Mater.* **2012**, *24*, 2109.

[53] Z. Zhu, D. Zhang, H. Yan, W. Li, *J. Mater. Chem. A* **2013**, *1*, 5492.

[54] J. Lee, C. Kim, B. Kang, *NPG Asia Mater.* **2015**, *7*, e211.

[55] A. Manthiram, K. Chemelewski, E.-S. Lee, *Energy Environ. Sci.* **2014**, *7*, 1339.

[56] M. Freire, N. V. Kosova, C. Jordy, D. Chateigner, O. I. Lebedev, A. Maignan, V. Pralong, *Nat. Mater.* **2015**, *15*, 1.

[57] C. Kim, P. J. Phillips, B. Key, T. Yi, D. Nordlund, Y. S. Yu, R. D. Bayliss, S. D. Han, M. He, Z. Zhang, A. K. Burrell, R. F. Klie, J. Cabana, *Adv. Mater.* **2015**, *27*, 3377.

[58] D. Tang, Y. Sun, Z. Yang, L. Ben, L. Gu, X. Huang, *Chem. Mater.* **2014**, *26*, 3535.

[59] J. S. Yuan, H. B. Yin, Z. Y. Ji, H. N. Deng, *Ind. Eng. Chem. Res.* **2014**, *53*, 9889.

[60] H. C. Kang, D. K. Jun, B. Jin, E. M. Jin, K. H. Park, H. B. Gu, K. W. Kim, *J. Power Sources* **2008**, *179*, 340.

[61] F. Tian, L. Liu, X. Wang, Z. Yang, M. Zhou, X. Wang, *Compos. Sci. Technol.* **2012**, *72*, 344.

[62] B. Carter, G. Norton, *Ceramic Materials Science and Engineering*, **2007**.

[63] C. Herring, *J. Appl. Phys.* **1950**, *21*, 301.

[64] H. Gleiter, *Acta Metall.* **1969**, *17*, 853.

[65] F. Zhang, T. Zhou, Y. Liu, J. Leng, *Sci. Rep.* **2015**, *5*, DOI 10.1038/srep11152.

[66] A. C. Metaxas, *Power Eng. J.* **1991**, *5*, 237.

[67] A. C. Metaxas, R. J. Meredith, *Peter Peregrinus Ltd. London, Chapter 7, p151* **1983**, *29*, 659.

[68] Z. Tang, D. Gao, P. Chen, Z. Li, Q. Wu, *Pure Appl. Chem.* **2008**, *80*, 2537.

[69] H. Shin, S. Park, Y. Bae, Y. Sun, *Solid State Ionics* **2005**, *176*, 2577.

[70] Z. Zhu, D. Zhang, H. Yu, *Electrochim. Acta* **2014**, *115*, 290.

[71] D. Wang, I. Belharouak, G. Zhou, K. Amine, *Adv. Funct. Mater.* **2013**, *23*, 1070.

[72] W. B. Hua, X. D. Guo, Z. Zheng, Y. J. Wang, B. H. Zhong, B. Fang, J. Z. Wang, S. L. Chou, H. Liu, *J. Power Sources* **2015**, *275*, 200.

[73] W. Hua, Y. Wang, Y. Zhong, G. Wang, B. Zhong, B. Fang, X. Guo, S. Liao, H. Wang, *Chinese J. Chem.* **2015**, *33*, 261.

[74] J. Rodríguez-Carvajal, *Phys. B Phys. Condens. Matter* **1993**, *192*, 55.

[75] K. Momma, F. Izumi, *J. Appl. Crystallogr.* **2011**, *44*, 1272.

[76] P. A. Stadelmann, *Ultramicroscopy* **1987**, *21*, 131.

[77] J. Barthel, "Dr. Probe - High-resolution (S)TEM image simulation software," can be found under http://www.er-c.org/barthel/drprobe/, **2017**.

[78] C. L. Jia, S. B. Mi, J. Barthel, D. W. Wang, R. E. Dunin-Borkowski, K. W. Urban, A. Thust,

Nat. Mater. **2014**, *13*, 1044.

[79] L. Simonelli, C. Marini, W. Olszewski, M. Ávila Pérez, N. Ramanan, G. Guilera, V. Cuartero, K. Klementiev, N. L. Saini, *Cogent Phys.* **2016**, *3*, 1231987.

[80] M.-H. Lee, Y.-J. Kang, S.-T. Myung, Y.-K. Sun, *Electrochim. Acta* **2004**, *50*, 939.

[81] S. Klaus, Y. Cai, M. W. Louie, L. Trotochaud, A. T. Bell, *J. Phys. Chem. C* **2015**, *119*, 7243.

[82] P. F. Smith, B. J. Deibert, S. Kaushik, G. Gardner, S. Hwang, H. Wang, J. F. Al-Sharab, E. Garfunkel, L. Fabris, J. Li, G. C. Dismukes, *ACS Catal.* **2016**, *6*, 2089.

[83] A. R. Armstrong, P. G. Bruce, *Nature* **1996**, *381*, 499.

[84] H. R. Oswald, R. Asper, in *Prep. Cryst. Growth Mater. with Layer. Struct.* (Ed.: R.M.A. Lieth), Springer Netherlands, Dordrecht, **1977**, pp. 71–140.

[85] Y.-K. Sun, S.-T. Myung, B.-C. Park, J. Prakash, I. Belharouak, K. Amine, *Nat. Mater.* **2009**, *8*, 320.

[86] W. Hua, W. Liu, M. Chen, S. Indris, Z. Zheng, X. Guo, M. Bruns, T.-H. Wu, Y. Chen, B. Zhong, S. Chou, Y.-M. Kang, H. Ehrenberg, *Electrochim. Acta* **2017**, *232*, 123.

[87] L. Lan, Q. Li, G. Gu, H. Zhang, B. Liu, *J. Alloys Compd.* **2015**, *644*, 430.

[88] J. Zhao, W. Zhang, A. Huq, S. T. Misture, B. Zhang, S. Guo, L. Wu, Y. Zhu, Z. Chen, K. Amine, F. Pan, J. Bai, F. Wang, *Adv. Energy Mater.* **2016**, 1601266.

[89] W. Hua, B. Schwarz, M. Knapp, A. Senyshyn, A. Missiul, X. Mu, S. Wang, C. Kübel, J. R. Binder, S. Indris, H. Ehrenberg, *J. Electrochem. Soc.* **2019**, *166*, A5025.

[90] D. Adam, *Nature* **2003**, *421*, 571.

[91] K. Lee, S. Myung, Y. Sun, *Chem. Mater.* **2007**, *19*, 2727.

[92] X. Miao, Y. Yan, C. Wang, L. Cui, J. Fang, G. Yang, *J. Power Sources* **2014**, *247*, 219.

[93] R. Baddour-hadjean, *Chem. Rev.* **2010**, *110*, 1278.

[94] F. Dogan, J. R. Croy, M. Balasubramanian, M. D. Slater, H. Iddir, C. S. Johnson, J. T. Vaughey, B. Key, *J. Electrochem. Soc.* **2015**, *162*, A235.

[95] C. P. Grey, N. Dupré, *Chem. Rev.* **2004**, *104*, 4493.

[96] J. Cabana, M. Casas-Cabanas, *Chem. Mater.* **2012**, *24*, 2952.

[97] A. Karim, S. Fosse, K. A. Persson, *Phys. Rev. B* **2013**, *87*, 75322.

[98] G. Z. Wei, X. Lu, F. S. Ke, L. Huang, J. T. Li, Z. X. Wang, Z. Y. Zhou, S. G. Sun, *Adv. Mater.* **2010**, *22*, 4364.

[99] G. Wulff, *Zeitschrift für Kryst. und Mineral.* **1901**, *34*, 449.

[100] S. Permien, S. Indris, A. L. Hansen, M. Scheuermann, D. Zahn, U. Schürmann, G. Neubüser, L. Kienle, E. Yegudin, W. Bensch, *ACS Appl. Mater. Interfaces* **2016**, *8*, 15320.

[101] S. Kobayashi, I. R. M. Kottegoda, Y. Uchimoto, M. Wakihara, *J. Mater. Chem.* **2004**, *14*, 1843.

[102] D. A. Weber, A. Senyshyn, K. S. Weldert, S. Wenzel, W. Zhang, R. Kaiser, S. Berendts, J. Janek, W. G. Zeier, *Chem. Mater.* **2016**, *28*, 5905.

[103] Y. Wang, Z. Yang, Y. Qian, L. Gu, H. Zhou, *Adv. Mater.* **2015**, *27*, 3915.

[104] F. Wu, N. Li, Y. Su, L. Zhang, L. Bao, J. Wang, L. Chen, Y. Zheng, L. Dai, J. Peng, S. Chen, *Nano Lett.* **2014**, *14*, 3550.

[105] L. Chen, Y. Su, S. Chen, N. Li, L. Bao, W. Li, Z. Wang, M. Wang, F. Wu, *Adv. Mater.* **2014**, 6756.

[106] M. Xu, L. Fei, W. Zhang, T. Li, W. Lu, N. Zhang, Y. Lai, Z. Zhang, J. Fang, K. Zhang, J. Li, H. Huang, *Nano Lett.* **2017**, *17*, 1670.

[107] F. Fu, Y. Yao, H. Wang, G.-L. Xu, K. Amine, S.-G. Sun, M. Shao, *Nano Energy* **2017**, *35*, 370.

[108] M. Xu, L. Fei, W. Lu, Z. Chen, T. Li, Y. Liu, G. Gao, Y. Lai, Z. Zhang, P. Wang, H. Huang, *Nano Energy* **2017**, *35*, 271.

[109] W. Hua, Z. Wu, M. Chen, M. Knapp, X. Guo, S. Indris, J. R. Binder, N. N. Bramnik, B. Zhong, H. Guo, S. Chou, Y.-M. Kang, H. Ehrenberg, *J. Mater. Chem. A* **2017**, *5*, 25391.

[110] J. Hong, D.-H. Seo, S.-W. Kim, H. Gwon, S.-T. Oh, K. Kang, *J. Mater. Chem.* **2010**, *20*, 10179.

[111] U. Ulvestad, A. Singer, J. N. Clark, H. M. Cho, J. W. Kim, R. Harder, J. Maser, Y. S. Meng, O. G. Shpyrko, *Science.* **2015**, *348*, 1344.

[112] A. R. Armstrong, M. Holzapfel, P. Novák, C. S. Johnson, S. H. Kang, M. M. Thackeray, P. G. Bruce, *J. Am. Chem. Soc.* **2006**, *128*, 8694.

[113] M. Sathiya, A. M. Abakumov, D. Foix, G. Rousse, K. Ramesha, M. Saubanère, M. L. Doublet, H. Vezin, C. P. Laisa, A. S. Prakash, D. Gonbeau, G. VanTendeloo, J.-M. Tarascon, *Nat. Mater.* **2015**, *14*, 230.

[114] L. Aldon, P. Kubiak, M. Womes, J. C. Jumas, J. Olivier-Fourcade, J. L. Tirado, J. I. Corredor, C. P. Vicente, *Chem. Mater.* **2004**, *16*, 5721.

[115] Y. Koyama, I. Tanaka, H. Adachi, Y. Makimura, T. Ohzuku, *J. Power Sources* **2003**, *119*–

121, 644.

[116] R. D. Shannon, *Acta Crystallogr. Sect. A* **1976**, *32*, 751.

[117] R. Tackett, G. Lawes, B. C. Melot, M. Grossman, E. S. Toberer, R. Seshadri, *Phys. Rev. B* **2007**, *76*, 24409.

[118] M. Kim, X. M. Chen, Y. I. Joe, E. Fradkin, P. Abbamonte, S. L. Cooper, *Phys. Rev. Lett.* **2010**, *104*, 136402.

[119] J. Cabana, S.-H. Kang, C. S. Johnson, M. M. Thackeray, C. P. Grey, *J. Electrochem. Soc.* **2009**, *156*, A730.

[120] W.-S. Yoon, S. Iannopollo, C. P. Grey, D. Carlier, J. Gorman, J. Reed, G. Ceder, *Electrochem. Solid-State Lett.* **2004**, *7*, A167.

[121] D. Zeng, J. Cabana, J. Bréger, W.-S. Yoon, C. P. Grey, *Chem. Mater.* **2007**, *19*, 6277.

[122] E. Hu, X. Yu, R. Lin, X. Bi, J. Lu, S. Bak, K.-W. Nam, H. L. Xin, C. Jaye, D. A. Fischer, K. Amine, X.-Q. Yang, *Nat. Energy* **2018**, DOI 10.1038/s41560-018-0207-z.

[123] E. Hu, S. M. Bak, J. Liu, X. Yu, Y. Zhou, S. N. Ehrlich, X. Q. Yang, K. W. Nam, *Chem. Mater.* **2014**, *26*, 1108.

[124] J. M. Tarascon, W. R. McKinnon, F. Coowar, T. N. Bowmer, G. Amatucci, D. Guyomard, *J. Electrochem. Soc.* **1994**, *141*, 1421.

[125] C. M. Rost, E. Sachet, T. Borman, A. Moballegh, E. C. Dickey, D. Hou, J. L. Jones, S. Curtarolo, J. P. Maria, *Nat. Commun.* **2015**, *6*, DOI 10.1038/ncomms9485.

[126] B. J. Morgan, P. A. Madden, *Phys. Chem. Chem. Phys.* **2006**, *8*, 3304.

Acknowledge

The present study was performed at the Institute of Inorganic Chemistry (Karlsruhe Institute of Technology, KIT), Institute for Applied Materials - Energy Storage Systems (IAM-ESS), and Sichuan University (SCU). I got the financial support for the first year of this PhD work from the College of Chemical Engineering (SCU). And later, as a PhD student in KIT, I received the financial support from the China Scholarship Council (CSC, No. 201606240081).

Firstly, I am grateful to my supervisor and referee Prof. Dr. Helmut Ehrenberg, who gave me the opportunity to work in IAM-ESS, for his great support, valuable guidance and thoughtful comments. I would like to thank my supervisor Prof. Benhe Zhong in SCU for her enthusiastic guidance. I also want thank to Prof. Dr. Stefano Passerini for being my co-referee, Prof. Dr. Jan-Dierk Grunwaldt, and Prof. Dr. Rolf Schuster for being my examiners.

Next, I would like to express my sincere gratitude to my co-supervisor Dr. Sylvio Indris for his understanding, encouragement, brilliant suggestion, and constant support during my study at KIT. I also wish to express my deep appreciation to Dr. Björn Schwarz for his kind support and help. I am very lucky to work with them. We always discussed some scientific questions together, they taught me a lot, guided me perfectly.

I am grateful to Dr. Michael Knapp, Dr. Joachim R. Binder, Dr. Michael Bruns for providing support and giving useful comments on this work. The help from my colleagues at IAM-ESS, Dr. Sonia Dsoke, Dr. Frieder Scheiba, Dr. Angelina Sarapulova, Dr. Andy Fiedler, Dr. Florian Sigel, Dr. Cyril Ehi-Eromosele, Dr. Murat Yavuz, Dr. Raheleh Azmi, Dr. Nadine Dannehl, Dr. Susana Darma, Dr. Holger Geßwein, Dr. Michael Heere, Dr. Julia Maibach, Dr. Michael Lang, Dr. Geethu Balachandran, Dr. Christoph Dräger, Georg-Maximilian Bosch, Heike Stöffler, Dr. Tatiana Zinkevich, Lars Esmezjan, etc., are gratefully acknowledged. In addition, the kind assistance from Chinese colleagues at IAM-ESS, Dr. Guiying Tian, Qiang Fu, Lihua Zhu, Zijian Zhao, Dr. Jiangong Zhu, Dr. Jiarong He, Xinyang Liu, Xiaolin Luo, Chengping Li, etc., are highly appreciated.

I want to thank my colleague from SCU, such as Prof. Xiaodong Guo, Prof. Xinlong Wang, Prof. Zhiye Zhang, Dr. Xiushan Yang, Dr. Yanjun Zhong and Dr. Zhenguo Wu, Dr. Yanxiao Chen, Dr. Zhuo Zheng, for their nice help during the first year of this research. I would like to thank Prof.

Shulei Chou (University of Wollongong, Australia) and Prof. Yong-Mook Kang (Dongguk University-Seoul, Republic of Korea) for their fruitful discussions. People from Shulei's group, Mingzhe Chen, Enhui Wang, Haipeng Zhou, Zichao Yan, etc., are also acknowledged. I am grateful to Prof. Clare P. Grey (University of Cambridge, UK) for useful discussions and constructive suggestions.

I would like to Dr. Anatoliy Senyshyn (SPODI beamline at MLZ, Munich) for the neutron diffraction measurements; Dr. Martin Etter (P02.1 beamline at PETRA III, Hamburg), Dr. Alexander Schökel (P02.1 beamline at PETRA III), and Dr. Aleksandr Missiul (MSPD beamline at ALBA, Barcelona) for synchrotron radiation diffraction experiments; Dr. Stefan Mangold (XAS beamline at KIT synchrotron, Karlsruhe), Dr. Vadim Murzin (P64 beamline at PETRA III) and Dr. Laura Simonelli (CLAESS beamline at ALBA) for the XAS measurements; Dr. Gilberto Casillas-Garcia (UOW) for the STEM technique support; Dr. Suning Wang and Ziyue Guan for helping with the sample synthesis; Dr. Xiaoke Mu and Dr. Di Wang for the TEM experiments; Margarete Offermann for BET measurements; Daniela Linder for TG/DSC measurements; Udo Geckle and Bettina Hunzinger for the SEM-EDX experiments; Liuda Mereacre for Raman measurements. All colleagues working on this topic in IAM-ESS and SCU are gratefully acknowledged for their support and help during this research.

This work was supported by the Deutsche Forschungsgemein-schaft (DFG) under SFB 595 "Electrical Fatigue in Functional Materials" (project T3), the National Natural Science Foundation of China (Grant No. 21506133). The Bundesministerium für Bildung und Forschung (BMBF) supports Energy Research With Neutrons (ErwiN) with grant no. 05K16VK2. Part of these experiments were performed at MSPD beamline at ALBA Synchrotron with the collaboration of ALBA staff and CALIPSOplus funding (Grant 730872). This work contributes to the research performed at CELEST (Center for Electrochemical Energy Storage Ulm-Karlsruhe).

Finally, I would like to thank my parents and my brother for their love and support. I wish to express my deep gratitude to my wonderful wife, Dr. Suning Wang, who is always there for me and gives me love and confidence during my PhD study. My special thanks go to my daughter, Ke Hua, she makes me so happy.

Curriculum vitae

Personal Information

Name**:** Weibo Hua

Academic Experience

10/2016-present **Karlsruhe Institute of Technology (KIT) / Institute of Applied Materials-Energy Storage Systems (IAM-ESS)**, Karlsruhe, Germany, (Research Associate, China Scholarship Council (CSC) fellowship for PhD student).

09/2015-10/2016 **College of Chemical Engineering, Sichuan University**, Chengdu, China, (Research Associate, National Doctoral Fellowship).

09/2012-7/2015 **College of Chemical Engineering, Sichuan University**, Chengdu, China, Project: Synthesis and electrochemical properties of $LiNi_{1/3}Co_{1/3}Mn_{1/3}O_2$ cathode materials for lithium ion batteries (Master's Thesis Research).

09/2010-07/2012 **Department of Environmental and Chemical Engineering, Tangshan University**, Tangshan, China, (Bachelor's Thesis Research).

09/2007-07/2010 **Department of Environmental Engineering, North China Institute of Science and Technology**, Langfang, China.

Practical Experience

10/2016-Present Synchrotron Radiation Diffraction and Absorption Experiments at different beamlines at **DESY** (Hamburg, Germany); at **ESRF** (Grenoble, France); at **ALBA** (Barcelona, Spain); at **PSI** (Villigen, Switzerland).

10/2016-Present Neutron Diffraction Experiments at SPODI beamline at **FRM II** (Munich); at D2B beamline at **ILL** (Grenoble, France).

25/02/2018-30/03/2018 Session A: PHYSICS AND CHEMISTRY OF CONDENSED MATTER at **HERCULES** (Higher European Research Course for Users of Large Experimental Systems) 2018 School.

06/2012-08/2012 Internship at **Synthesis Section**, Beijing Easpring Material Technology Co.,Ltd, Xinxiang, China.

06/2010-11/2010 Training at **Synthesis Section** for producing Methanol (CH_3OH) from coal mining, Guizhou Shuicheng Mining Group Co., Ltd, Liupanshui, China.

Scientific Publications

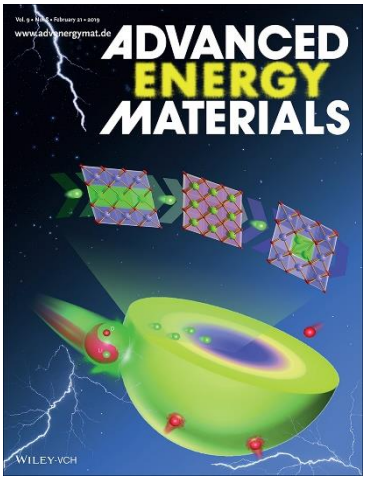

[1] **Weibo Hua**, Mingzhe Chen, Björn Schwarz, Michael Knapp, Michael Bruns, Juri Barthel, Xiushan Yang, Florian Sigel, Raheleh Azmi, Anatoliy Senyshyn, Alkesandr Missiul, Laura Simonelli, Martin Etter, Suning Wang, Xiaoke Mu, Andy Fiedler, Joachim R. Binder, Xiaodong Guo, Shulei Chou, Benhe Zhong, Sylvio Indris, and Helmut Ehrenberg. Lithium/oxygen incorporation and microstructural evolution during synthesis of Li-rich layered $Li[Li_{0.2}Ni_{0.2}Mn_{0.6}]O_2$ oxides. ***Adv. Energy Mater.***, 2019, 9(8), 1803094.

[2] **Weibo Hua**, Björn Schwarz, Michael Knapp, Anatoliy Senyshyn, Alkesandr Missiul, Xiaoke Mu, Suning Wang, Christian Kübel, Joachim R Binder, Sylvio Indris, Helmut Ehrenberg. (De)Lithiation mechanism of hierarchically layered $LiNi_{1/3}Co_{1/3}Mn_{1/3}O_2$ cathodes during high-voltage cycling. ***J. Electrochem. Soc.***, 2019, 166(3), A5025-A5032.

[3] Mingzhe Chen, **Weibo Hua**, Jin Xiao, David Cortie, Weihua Chen, Enhui Wang, Zhe Hu, Qinfen Gu, Xiaolin Wang, Sylvio Indris, Shu-Lei Chou, Shi-Xue Dou. NASICON-type air-stable and all-climate cathode for sodium-ion batteries with low cost and high-power density. ***Nat. Comm.***, 2019, 10, 1480.

[4] Zichao Yan, Liang Tang, Yangyang Huang, **Weibo Hua**, Yong Wang, Rong Liu, Qinfen Gu, Sylvio Indris, Shulei Chou, Yunhui Huang, Minghong Wu, Shi-Xue Dou. A hydrostable cathode material based on the layered P2@P3 composite with revealed redox behavior of Cu for high-rate and long cycling sodium-ion batteries, ***Angew. Chem. Int. Ed. Engl.***, 2019, 131(5), 1426-1430.

[5] Yumei Liu, Enhui Wang, Ranjusha Rajagopalan, **Weibo Hua**, Benhe Zhong, Yanjun Zhong, Zhenguo Wu, Xiaodong Guo, Shixue Dou, Juntao Li. Rational design and synthesis of advanced $Na_{3.32}Fe_{2.34}(P_2O_7)_2$ cathode with multiple-dimensional N-doped carbon matrix. ***J. Power Sources***, 2019, 412(1), 350-358.

[6] Mingzhe Chen, David Cortie, Zhe Hu, Huile Jin, Shun Wang, Qinfen Gu, **Weibo Hua**, Enhui Wang, Weihong Lai, Lingna Chen, Shu-Lei Chou, Xiao-Lin Wang, Shi-Xue Dou. A novel graphene oxide wrapped $Na_2Fe_2(SO_4)_3$/C cathode composite for long life and high energy density sodium-ion batteries, ***Adv. Energy Mater.***, 2018, 5, 1800944.

[7] Chunjin Wu, **Weibo Hua**, Zheng Zhang, Benhe Zhong, Zuguang Yang, Guilin Feng, Wei Xiang, Zhenguo Wu, Xiaodong Guo. Design and synthesis of layered $Na_2Ti_3O_7$ and tunnel $Na_2Ti_6O_{13}$ hybrid structures with enhanced electrochemical behavior for sodium-ion batteries, ***Adv. Sci.***, 2018, 5, 1800519.

[8] Yumei Liu, Ranjusha Rajagopalan, Enhui Wang, Mingzhe Chen, **Weibo Hua**, Benhe Zhong, Yan-Jun Zhong, Zhen-Guo Wu, Xiaodong Guo. Insight into the multi-role of graphene in preparation of high performance $Na_{2+2x}Fe_{2-x}(SO_4)_3$ cathodes, ***ACS Sustain. Chem. Eng.***, 2018, 6(12), 16105-16112.

[9] Chun-Liu Xu, Wei Xiang, Zhen-Guo Wu, Yong-Chun Li, Ya-Di Xu, **Wei-Bo Hua**, Xiao-Dong Guo, Xiao-Bing Zhang, Ben-He Zhong. A comparative study of crystalline and amorphous $Li_{0.5}La_{0.5}TiO_3$ as surface coating layers to enhance the electrochemical performance of $LiNi_{0.815}Co_{0.15}Al_{0.035}O_2$ cathode. ***J. Alloys Compd.***, 2018, 740, 428-435.

[10] **Weibo Hua**, Zhenguo Wu, Mingzhe Chen, Michael Knapp, Xiaodong Guo, Sylvio Indris, Joachim R. Binder, Natalia N. Bramnik, Benhe Zhong, Haipeng Guo, Shulei Chou, Yong-Mook Kang, and Helmut Ehrenberg. Shape-controlled synthesis of hierarchically layered lithium transition-metal oxide cathode materials by shear exfoliation in continuous stirred-tank reactors. ***J. Mater. Chem. A***, 2017, 5, 25391-25400.

[11] **Weibo Hua**, Wenyuan Liu, Mingzhe Chen, Sylvio Indris, Zhuo Zheng, Xiaodong Guo, Michael Bruns, Tai-Hsien Wu, Yanxiao Chen, Benhe Zhong, Shulei Chou, and Yong-Mook Kang, Helmut Ehrenberg. Unravelling the growth mechanism of hierarchically structured $Ni_{1/3}Co_{1/3}Mn_{1/3}(OH)_2$ and their application as precursors for high-power cathode materials. ***Electrochim. Acta***, 2017, 232, 123-131.

[12] Zuguang Yang, Xiaodong Guo, Wei Xiang, **Weibo Hua**, Jun Zhang, Fengrong He, Kai Wang, Yao Xiao, Benhe Zhong. K-doped layered $LiNi_{0.5}Co_{0.2}Mn_{0.3}O_2$ cathode material: Towards the superior rate capability and cycling performance. ***J. Alloys Compd.***, 2017, 699, 358-365.

[13] Zhuo Zheng, **Wei-Bo Hua**, Zhen-Guo Wu, Wei Xiang, Ben-He Zhong, and Xiao-Dong Guo. Controllable preparation of ultra-high rate $LiNi_{1/3}Co_{1/3}Mn_{1/3}O_2$ cathode through carbonate co-precipitation method for Li-Ion batteries. ***Chin. Inorg. Chem.***, 33, 2017 (2): 307-314.

[14] Zhuo Zheng, Xiao-Dong Guo, Zhen-Guo Wu, **Weibo Hua**, Benhe Zhong. Preparation of carbon-coated $LiNi_{1/3}Co_{1/3}Mn_{1/3}O_2$ cathode for high-rate lithium ion batteries. ***Chin. Inorg. Chem.***, 33, 2017 (1): 106-114.

[15] Zheng Zhuo, Xiushan Yang, **Weibo Hua**, Yan Tang. Effective enhancement of the electrochemical performance of layered Li-rich cathode $Li_{1.5}Ni_{0.25}Mn_{0.75}O_{2.5}$ by a facile molten salt method for lithium-ion batteries. ***Chin. J. Inorg. Chem.***, 2017, 33(6), 963-969.

[16] Zheng Zhuo, Zhenguo Wu, Wei Xiang, **Weibo Hua**, Xiaodong Guo. Preparation and electrochemical performance of Na^+-stabilized layered $LiNi_{0.6}Co_{0.2}Mn_{0.2}O_2$ cathode material for lithium-ion batteries. ***Chin. J. Chin. University-Chin.***, 2017, 38(8), 1458-1464.

[17] Mingzhe Chen, Zhe Hu, Zhenguo Wu, **Weibo Hua**, Kiyoshi Ozawa, Qinfen Gu, Yong-Mook Kang, Xiaodong Guo, Shu-Lei Chou, Shi-Xue Dou. Understanding performance differences from various synthesis methods: A case study of spinel $LiCr_{0.2}Ni_{0.4}Mn_{1.4}O_4$ cathode material. ***ACS Appl. Mater. Interfaces***, 2016, 8(39), 26051-26057.

[18] Wenyuan Liu, **Weibo Hua**, Zhuo Zheng, Benhe Zhong, Zhiye Zhang. Facile synthesis of hierarchical porous Ni-rich $LiNi_{0.6}Co_{0.2}Mn_{0.2}O_2$ cathode material with superior high-rate capability. ***Ionics***, 2016, 22(10), 1781-1790.

[19] Zhuo Zheng, Xiao-Dong Guo, Shu-Lei Chou, **Wei-Bo Hua**, Hua-Kun Liu, Shi Xue Dou, Xiu-Shan Yang. Uniform Ni-rich $LiNi_{0.6}Co_{0.2}Mn_{0.2}O_2$ Porous Microspheres: Facile Designed Synthesis and Their Improved Electrochemical Performance. ***Electrochim. Acta***, 2016 (191), 401-410.

[20] Su-Ning Wang, Jian-Li Wang, **Wei-Bo Hua**, Meng-Meng Sun, Zhong-Hua Shi, Shan-Dong Yuan, Lin Zhong, Yao-Qiang Chen. Designed synthesis of Zr-based ceria-zirconia-neodymia composite with high thermal stability and its enhanced catalytic performance for Rh-only three-way catalyst. ***Cat. Sci. Tech.***, 2016, 6(20), 7437-7448.

[21] Zhuo Zheng, Xiao-Dong Guo, Yan-Jun Zhong, **Wei-Bo Hua**, Chong-Heng Shen, Shu-Lei Chou, Xiu-Shan Yang. Host structural stabilization of $Li_{1.232}Mn_{0.615}Ni_{0.154}O_2$ through K-doping attempt: toward superior electrochemical performances. ***Electrochim. Acta***, 2016, 188, 336-343.

[22] Zu-Guang Yang, **Wei-Bo Hua**, Jun Zhang, Jiu-Hua Chen, Feng-Rong He, Ben-He Zhong, Xiao-Dong Guo. Enhanced electrochemical performance of $LiNi_{0.5}Co_{0.2}Mn_{0.3}O_2$ cathode materials at elevated temperature by Zr Doping. ***Acta Phys. -Chim. Sin.***, 2016, 32(5): 1056-1061.

[23] **Wei-Bo Hua**, Xiao-Dong Guo, Zhuo Zheng, Yan-Jie Wang, Benhe Zhong, Baizeng Fang, Jia-Zhao Wang, Shu-Lei Chou, Heng Liu. Uncovering a facile large-scale synthesis of $LiNi_{1/3}Co_{1/3}Mn_{1/3}O_2$ nanoflowers for high power lithium-ion batteries. ***J. Power Sources***, 2015, 275, 200-206.

[24] **Weibo Hua**, Su-Ning Wang, Xiao-Dong Guo, Shu-Lei Chou, Kui Yin, Ben-He Zhong, Shi-Xue Dou. Vacuum induced self-assembling nanoporous $LiMn_2O_4$ for lithium ion batteries with superior high rate capability. ***Electrochim. Acta***, 2015, 186, 253-261.

[25] **Weibo Hua**, Yan-Jie Wang, Yan-Jun Zhong, Guoping Wang, Ben-He Zhong, Baizeng Fang, Xiao-Dong Guo, Shi-Xuan Liao, Haijiang Wang. An approach towards the synthesis of nanoarchitectured $LiNi_{1/3}Co_{1/3}Mn_{1/3}O_2$ cathode material for lithium ion batteries. ***Chin. J. Chem.***, 2015, 33, 261-267.

[26] Zhuo Zheng, **Wei-Bo Hua**, Chong Yu, Yan-Jun Zhong, Binbin Xu, Jiazhao Wang, Benhe Zhong, Zhiye Zhang. Heterogeneous intergrowth $xLi_{1.5}Ni_{0.25}Mn_{0.75}O_{2.5}\cdot(1-x)Li_{0.5}Ni_{0.25}Mn_{0.75}O_2$ ($0 \leq x \leq 1$) composite: synergistic effect on electrochemical performance. ***Dalton Trans.***, 2015, 44, 14255-14264.

[27] Su-Ning Wang, Li Lan, **Wei-Bo Hua**, Zhong-Hua Shi, Yao-Qiang Chen, Mao-Chu Gong, Lin Zhong. Ce–Zr–La/Al_2O_3 prepared in a continuous stirred-tank reactor: a highly thermostable support for an efficient Rh-based three-way catalyst. ***Dalton Trans.***, 2015, 44, 20484-20492.

[28] Zhuo Zheng, **Wei-Bo Hua**, Shi-Xuan Liao, Yan-Jun Zhong, En-Hui Wang, Binbin Xu, Hua-Kun Liu, Benhe Zhong. Effective enhancement of electrochemical performance for layered cathode $Li_{1.5}Mn_{0.75}Ni_{0.25}O_{2.5}$ via a novel facile molten salt method. ***RSC Adv.***, 2015, 5, 58528-58535.

[29] Zhuo Zheng, Zhen-Guo Wu, Yan-Jun Zhong, Chong-Heng Shen, **Weibo Hua**, Binbin Xu, Chong Yu, Benhe Zhong, Xiao-Dong Guo. A further electrochemical investigation on solution to high energetical power source: Isomerous compound $0.75Li_{1.2}Ni_{0.2}Mn_{0.6}O_2\cdot0.25LiNi_{0.5}Mn_{1.5}O_4$. ***RSC Adv.***, 2015, 5, 37330-37339.

[30] Ji-Bin Zhang, **Wei-Bo Hua**, Zhuo Zheng, Wen-Yuan Liu, Xiao-Dong Guo, Ben-He Zhong. Preparation and electrochemical performance of $Li[Ni_{1/3}Co_{1/3}Mn_{1/3}]O_2$ cathode material for high rate lithium ion battery. ***Acta Phys. -Chim. Sin.***, 2015, *31*(5), 905-912.

[31] Ji-Bin Zhang, Zhen-Guo Wu, **Wei-Bo Hua**, Heng Liu, Ben-He Zhong. High-performance porous spherical cathode materials based on $CaCO_3$-template synthesis of $LiNi_{1/3}Co_{1/3}Mn_{1/3}O_2$ for lithium-ion batteries. ***Ionics***, 2015, 21, 3151-3158.

[32] Jibin Zhang, Yanjun Zhong, Xiaxing Shi, Zhuo Zheng, **Weibo Hua**, Yanxiao Chen, Wenyuan Liu, Benhe Zhong. Preparation and electrochemical performance of $Li[Ni_{1/3}Co_{1/3}Mn_{1/3}]O_2$ synthesized using Li_2CO_3 as template. ***Chin. J. Chem.***, 2015, 33, 1303-1309.

[33] **Weibo Hua**, Jibin Zhang, Zhuo Zheng, Wenyuan Liu, Xiao-Dong Guo, Benhe Zhong, Yan-Jie Wang, Xinlong Wang. Na-doped Ni-rich $LiNi_{0.5}Co_{0.2}Mn_{0.3}O_2$ cathode material with both high rate capability and high tap density for lithium ion battery. ***Dalton Trans.***, 2014, 43, 14824-14832.

[34] **Wei-Bo Hua**, Zhuo Zheng, Long-Yan Li, Xiao-Dong Guo, Heng Liu, Chong-Heng Shen, Zhen-Guo Wu, Ben-He Zhong, Ling Huang. Synthesis of nanostructured $LiNi_{1/3}Co_{1/3}Mn_{1/3}O_2$ by ammonia-evaporation-induced synthesis and its electrochemical properties as a cathode material for a high-power li-ion battery. ***Acta Phys. -Chim. Sin.***, 2014, *30* (8), 1481-1486.

[35] **Wei-Bo Hua**, Xiao-Dong Guo, Zhuo Zheng, Ji-Bin Zhang, Ben-He Zhong. Synthesis and study on the nanosheet-structured $LiNi_{1/3}Co_{1/3}Mn_{1/3}O_2$ cathode material for lithium-ion batteries. ***Chem. Res. Appl.***, 2014, 26(3), 441-444.

[36] Shi-Xuan Liao, Ben-He Zhong, Xiaodong Guo, Xia-Xing Shi, **Wei-Bo Hua**. Facile combustion synthesis and electrochemical performance of the cathode material $Li_{1.231}Mn_{0.615}Ni_{0.154}O_2$. ***Eur. J. Inorg. Chem***., 2013, 31, 5436-5442.

ORCID: https://orcid.org/0000-0001-5372-4422;

ResearcherID: http://www.researcherid.com/rid/R-9940-2016.

Patent

[1] Xiaodong Guo, **Weibo Hua**, Benhe Zhong, Zhenguo Wu, Zhuo Zheng, Jibin Zhang. Method for continuously preparing nanoflower lithium ion battery layered anode material and reaction kettle thereof. Publication number: CN206040815 U. (Grant of utility model patents)

Honors

- ✓ National motivational scholarship, North China Institute of Science and Technology, 2009
- ✓ First prize of "The 11th mathematics and application ability" competition, North China Institute of Science and Technology, 2009
- ✓ Comprehensive first class scholarship, North China Institute of Science and Technology, 2010
- ✓ Third prize of "Challenge Cup" undergraduate curricular academic science and technology works, Tangshan University, 2011
- ✓ Excellent Bachelor Thesis Award, Tangshan University, Tangshan, China, 2012
- ✓ First-class Scholarship for Outstanding Students, Sichuan University, China, 2012-2015
- ✓ National Scholarship for Outstanding Students, Sichuan University, China, 2014
- ✓ Outstanding Graduate, Sichuan University, China, 2012-2015
- ✓ Outstanding Graduate of Sichuan Province, Chengdu, China, 2014
- ✓ Academic Star Award, College of Chemical Engineering, Sichuan University, 2014-2016
- ✓ The Evonik Scholarship for Excellent Students, Sichuan University, China, 2015
- ✓ Invited talk at opening ceremony for graduate Sichuan University 2016 (http://ce01.scu.edu.cn/info/news/68uj0oba64r91pcll6gs0krff6/)

Conferences

[1] The 17th National Conference on Electrochemistry, 7-11 Nov. 2013, Suzhou, Jiangsu Province, China.

[2] The International Symposium of Young Scientist on Next-Generation Batteries, 2015, Changsha, Hunan Province, China.

[3] The 19th International Meeting on Lithium Batteries (IMLB2018). 17-22 Jun, 2018, Kyoto, Japan.

Dedication

To my wife, my daughter, and my parents for their dedication…

Declaration

Ich versichere hiermit, dass ich die vorliegende Dissertation selbständig und ohne unzulässige fremde Hilfe erbracht habe. Ich habe keine anderen als die angegeben Quellen und Hilfsmittel benutzt, sowie wörtliche und sinngemäße Zitate kenntlich gemacht. Die Dissertation wurde bisher an keiner anderen Hochschule oder Universität eingereicht.

Karlsruhe, den 07.01.2019

M. Sc. Weibo Hua

I hereby declare that I have made this work independently and used no other than the specified sources and tools, as well as, whether verbatim or with regards to content, indicated all citations as such and I have paid attention to the statute of the Karlsruhe Institute of Technology (KIT) in the current version to ensure good scientific practice.

Karlsruhe, 07.01.2019

M. Sc. Weibo Hua